



Titre: Mode Split Prediction for Rotating Disks with Flexible Stator
Title: Coupling

Auteur: Lucas Berthet
Author:

Date: 2021

Type: Mémoire ou thèse / Dissertation or Thesis

Référence: Berthet, L. (2021). Mode Split Prediction for Rotating Disks with Flexible Stator Coupling [Master's thesis, Polytechnique Montréal]. PolyPublie.
Citation: <https://publications.polymtl.ca/9918/>

 **Document en libre accès dans PolyPublie**
Open Access document in PolyPublie

URL de PolyPublie: <https://publications.polymtl.ca/9918/>
PolyPublie URL:

Directeurs de recherche: Frederick Gosselin
Advisors:

Programme: Génie mécanique
Program:

POLYTECHNIQUE MONTRÉAL
affiliée à l'Université de Montréal

Mode Split Prediction for Rotating Disks with Flexible Stator Coupling

LUCAS BERTHET
Département de génie mécanique

Mémoire présenté en vue de l'obtention du diplôme de *Maîtrise ès sciences appliquées*
Génie mécanique

Décembre 2021

POLYTECHNIQUE MONTRÉAL

affiliée à l'Université de Montréal

Ce mémoire intitulé :

Mode Split Prediction for Rotating Disks with Flexible Stator Coupling

présenté par **Lucas BERTHET**

en vue de l'obtention du diplôme de *Maîtrise ès sciences appliquées*

a été dûment accepté par le jury d'examen constitué de :

Aouni LAKIS, président

Frédéric P. GOSSELIN, membre et directeur de recherche

Alexandre PRESAS, membre

ACKNOWLEDGEMENTS

First, I would like to thank my research director Frédéric P. GOSSELIN for his continuous and dedicated guidance through this Master, creating a favorable environment for my first steps in research.

I would also like to thank Christine MONETTE and Bernd NENNEMANN for their help and advice throughout those two years, as well as for their warm welcome at Andritz Hydro Canada Inc.

Another thank to Philippe BLAIS for his great work during his internship, in addition to offering interest and suggestions during our exchanges. I would also like to thank my friends from the laboratory Gaétan RAYNAUD, Thomas CHARPENTIER, Sima RISHMAWI, Mohammed ABDA, Morgan DEMENOIS, David LESSARD and Anamaria SERBESCU.

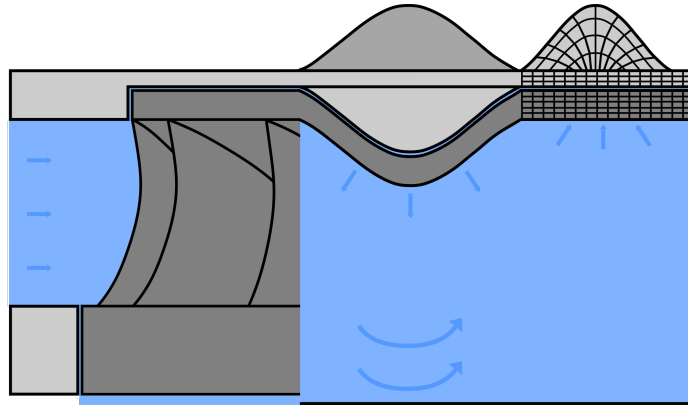
My sincere acknowledgements to the Mitacs Accelerate Program and to Andritz Hydro Canada Inc. for financing my project during this Master.

RÉSUMÉ

D'après le dernier rapport du Groupe d'experts Intergouvernemental sur l'Evolution du Climat (GIEC), la température planétaire a augmenté de 1.1°C depuis l'ère pré-industrielle, alors qu'il faudrait ne pas dépasser le seuil de 1.5°C pour éviter des conséquences irréversibles du dérèglement climatique. Pour cela, d'importantes réductions des émissions de gaz à effet de serre sont nécessaires, notamment dans le domaine de la production d'énergie. Les énergies fossiles sont remplacées par celles renouvelables, qui, étant intermittentes, doivent être compensées par l'hydroélectricité. Cela augmente la durée du fonctionnement transitoire des turbines, dont les nouvelles conditions d'opération doivent être prises en compte lors de leur conception. Cela se fait au travers de l'étude des phénomènes en jeu dans celles-ci et de leur comportement dynamique. Les roues hydrauliques, et notamment celles de haut débit ou fonctionnant aussi comme pompes, qui sont et seront les plus utilisées, sont soumises à de multiples sources d'excitation complexes, qu'il faut quantifier et qualifier. A l'inverse de l'Interaction Rotor-Stator (IRS) qui a été décrite et analysée, le phénomène de séparation des modes est mal connu et nécessite d'être étudié. Il se produit lorsque la roue tourne dans l'eau, et couplé à la masse ajoutée de cette dernière, introduit une séparation, ainsi qu'une dérive, de ses fréquences naturelles, associées aux vagues co et contre-rotative qui la parcourent pour différentes vitesses de rotation. Lors de l'étude du comportement dynamique de roues, employer la géométrie réelle au sein de simulations numériques requiert d'importantes ressources informatiques et durées de temps, alors qu'il est tout simplement impossible de le faire analytiquement. Ainsi, un modèle simplifié qui présente les mêmes caractéristiques dynamiques est nécessaire, et cela est le cas pour les disques, qui ont des modes de vibration similaires à ceux du rotor et du stator pour des basses fréquences. La séparation de modes pour un disque tournant dans un fluide dense a été analysé et expliqué par le passé expérimentalement, numériquement et analytiquement. Or, il s'avère que le stator se trouvant au-dessus de la roue est flexible comme il possède également une faible épaisseur. Dès lors que le rotor vibre et influence le fluide environnant, le stator est donc aussi impacté et participe au comportement dynamique globale de la structure. Ainsi, il est nécessaire de qualifier l'impact de ce couplage et la séparation de modes en présence d'un stator déformable. Pour cela, on développe dans ce projet deux modèles analytique et numérique de disques rotatif et stationnaire couplés par le fluide, pour étudier l'influence de leur interaction sur la séparation des modes. Dans un premier temps, on applique au fluide la théorie des écoulements potentiels, en le considérant irrotationnel, non-visqueux et incompressible. On suppose également que les disques observent des formes de modes similaires dans l'eau et le vide. En utilisant

cette hypothèse, on obtient les écoulements potentiels qui respectent la condition de non-pénétration entre le fluide et la structure. La déformation de l'interface fluide-structure entre le fluide et le disques est discrétisée avec la méthode de collocation par point. L'un après l'autre, chaque disque est considéré déformable, tandis que l'autre est rigide. Avec le principe de superposition, on couple les deux écoulements fluides obtenus ainsi dans les équations de mouvement. Le modèle numérique a été créé en collaboration avec Blais (2021) et présente les mêmes hypothèses et caractéristiques que le modèle analytique. En effet, il s'agit d'une analyse modale acoustique-structure faite sous Ansys, que nous utilisons pour vérifier son équivalent théorique et proposer un outil de simulation numérique rapide. Avec l'hypothèse de la non-viscosité du fluide, les modèles développés présentent moins de 3% d'erreur avec les données expérimentales issues de la littérature. Le modèle analytique permet une meilleure compréhension du phénomène de séparation des modes pour le couplage rotor-stator, tandis que l'analyse modale numérique offre une alternative aux simulations coûteuses en ressources et temps. Ils sont également capables de qualifier l'influence du stator au sein du couplage sur la performance globale de la structure, et de prédire le comportement dynamique de disques couplés par le fluide pour différentes configurations, dans le cadre de la conception de turbines.

ABSTRACT



High-head turbine runners are subject to multiple sources of excitations, e.g., Rotor-Stator Interaction (RSI) or trailing-edge vortices. Coupled with the added mass of water, rotation induces a mode split in the natural frequencies of runners, where co-rotating and counter-rotating waves travel through the runner at different relative speeds. Disks, by displaying a similar behavior, can be used as a simpler model. Mode split is characterized for a rotating disk in dense fluid but, in high-head turbines, the runner and the compliant confinement are coupled through the axial gap fluid. In this project, we develop an analytical model of coupled stationary and rotating disks to analyze the effect of their interaction on the mode split phenomenon. First, we apply the potential flow theory, considering the fluid as irrotational, inviscid and incompressible. We assume that the modeshapes of the disk in a dense fluid are similar to their shapes in vacuo. Based on these assumed modeshapes of the stationary and rotating disks, we derive the potential flows that respect the no-penetration boundary conditions. One after the other, each disk is considered flexible while the other one is rigid. By applying the superposition principle, we then couple the two obtained fluid flows through the structural equations of motion. An acoustic-structural modal analysis was developed in collaboration with Blais (2021) to verify the analytical model and propose a fast numerical tool for hydraulic turbine design. Despite the inviscid flow assumption, the derived models display less than 3% error with experimental data for large axial gaps and rotors thicker than stators. They predict the dynamic behavior of disks coupled through fluid for different configurations, offering an alternative to computationally expensive simulations. Additionally, they provide a better understanding of the mode split phenomenon in a rotor-stator system, by qualifying the influence of the stator component on the overall structure performance for turbine design.

TABLE OF CONTENTS

ACKNOWLEDGEMENTS	iii
RÉSUMÉ	iv
ABSTRACT	vi
TABLE OF CONTENTS	vii
LIST OF TABLES	ix
LIST OF FIGURES	x
LIST OF SYMBOLS AND ACRONYMS	xvi
LIST OF APPENDICES	xvii
CHAPTER 1 INTRODUCTION	1
CHAPTER 2 LITERATURE REVIEW	5
Mode split phenomenon	5
Rotor-stator coupling	6
Past analytical models	7
Past numerical models	11
CHAPTER 3 RESEARCH OBJECTIVES	13
CHAPTER 4 METHODOLOGY - ANALYTICAL MODEL	15
Submerged annular disk in rigid confinement	17
Structural model	17
Fluid model	20
Fluid-structure interaction model	21
Annular disk coupled through fluid with flexible disk	23
Fluid displacement potentials	24
Eigenfrequencies calculation	25
Convergence analysis	28
CHAPTER 5 METHODOLOGY - FEM MODEL	30

CHAPTER 6 RESULTS AND DISCUSSION	33
Submerged annular disk in rigid confinement	33
Validation of the analytical model	34
Comparison between the analytical and FEM models	36
Influence of parameters on implied physics	37
Annular disk coupled through fluid with flexible disk	43
Verification for the coupled static disks	44
Verification for the coupled static annuli	45
Validation for the coupled rotor-stator	46
Comparison between the analytical and FEM models	49
Influence of parameters on implied physics	51
CHAPTER 7 CONCLUSION	66
Limitations	67
Outlook	68
REFERENCES	69
APPENDICES	75

LIST OF TABLES

Table 2.1	Summary of all the studies that could be used as validation	12
Table 3.1	Summary of the research objectives	14
Table 6.1	Summary of all the developed models	33
Table 6.2	Model properties for the validation with experimental data from Presas et al. (2015a)	34
Table 6.3	Comparison with experimental natural frequencies from Presas et al. (2015a)	34
Table 6.4	Comparison of the ratio of the natural frequencies in fluid with those in vacuo from the analytical model and from Presas et al. (2015a) . .	35
Table 6.5	Natural frequencies in vacuo for FEM and analytical models	37
Table 6.6	Comparison of natural frequencies for diametrical modes from the analytical model and from Jeong (2003) - Two identical disks coupled with fluid	44
Table 6.7	Comparison of natural frequencies for diametrical modes from the analytical model and from Jeong (2006) - Two disks with different stiffness, coupled with fluid	45
Table 6.8	Model properties for the validation with experimental data from Weder (2018)	46
Table 6.9	Model properties for the parametric studies	51

LIST OF FIGURES

Figure 1.1	a) Schematic of a Francis turbine with the components of the stator and rotor, as well as the shaft; and b) example of a disk mode shape with $n = 3$ nodal diameters	1
Figure 1.2	a) Mode split; and b) frequency split and drift	3
Figure 1.3	(a) In-phase modes; and (b) out-of-phase modes with $n = 3$ nodal diameters for two identical annular disks	4
Figure 4.1	a) Geometry of a rotor and a stator in a fluid-filled tank; and b) interfaces between the fluid and the structure composed of the rotor, stator and confinement	16
Figure 4.2	a) Schematic of a flexible rotating annular disk - the rotor - in a rigid confinement similar to the experiments of Presas et al. (2015a); and b) schematic of the system coupling a flexible rotating annular disk - the rotor - with a flexible non-moving casing - the stator - similar to the experiments of Weder et al. (2019)	16
Figure 4.3	(a) Rotor-only deformation; and (b) stator-only deformation	24
Figure 4.4	N_i and N_s influence on (a) the natural frequencies of the rotor; and (b) the condition number of the pseudo-inverse matrix from the point collocation method	29
Figure 5.1	Basic mesh with quadratic elements from Blais (2021): a) section view with boundary conditions; and b) isometric section view	31
Figure 5.2	FEM workflow followed by Blais (2021)	32
Figure 6.1	Comparison of the analytical prediction (in continuous lines) with experimental data from Presas et al. (2015a) (in dot lines) for the effect of the disk rotational velocity Ω_R on the mode split magnitude $f_{F,-n} - f_{F,+n}$ for the three modes $n = 2, 3, 4$	36
Figure 6.2	Streamlines of the fluid velocity for the mode (2,0) of the confined rotor without rotation (a) in the plane $(r, \theta, 0.005)$ (where dash lines represent diameters with zero disk displacement, i.e. nodal diameters); and (b) in the plane $(r, 0, z)$	38
Figure 6.3	Natural frequencies of the co and counter-rotating waves of the confined rotor for the three modes $n = 2, 3, 4$ as a function of the disk angular velocity Ω_D , where the dash lines represent the central value of the eigenfrequencies	40

Figure 6.4	N_i and N_s influence on the natural frequencies of the rotor for $c - a = 3$ mm	41
Figure 6.5	Natural frequencies of the confined rotor without rotation for the modes $(2, 0)$, $(3, 0)$ and $(4, 0)$ as a function of: (a) the axial gap H_1 ; and (b) radial gap $c - a$	42
Figure 6.6	Influence of the rotor thickness h_R on the natural frequencies of the confined rotor without rotation for the modes $(2, 0)$, $(3, 0)$ and $(4, 0)$.	42
Figure 6.7	Natural frequencies of the confined rotor without rotation for the modes $(2, 0)$, $(3, 0)$ and $(4, 0)$ as a function of: (a) the inner radius b ; and (b) the outer radius a	43
Figure 6.8	Comparison of analytical results with experimental data from Weder (2018) for the natural frequencies of the in-phase modes $(2, 0)$, $(3, 0)$ and $(4, 0)$ as a function of the axial gap $H_1 - h_R = h_S = 1$ mm	47
Figure 6.9	Comparison of analytical results with experimental data from Weder (2018) for the natural frequencies of the in-phase modes $(2, 0)$ and $(3, 0)$ of the coupled rotor-stator as a function of the axial gap H_1 for: (a) $h_S = 1$ mm and $h_R = 1.5$ mm; and (b) $h_S = 1$ mm and $h_R = 2$ mm .	48
Figure 6.10	Comparison of analytical results with experimental data from Weder (2018) for the natural frequencies of the out-of-phase modes $(2, 0)$, $(3, 0)$ and $(4, 0)$ of the coupled rotor-stator as a function of the axial gap $H_1 - h_S = 1$ mm and $h_R = 2$ mm	49
Figure 6.11	Comparison of analytical results with FEM data for the effect of the axial gap on the natural frequencies of the coupled rotor-stator configuration for the modes $(2, 0)$, $(3, 0)$ and $(4, 0)$: (a) $(n, 0)^{\uparrow\uparrow}$ for $h_S = h_R = 1$ mm; (b) $h_R = 1.5$ mm; (c) $h_R = 2$ mm; and (d) $(n, 0)^{\uparrow\downarrow}$ for $h_S = 1$ mm and $h_R = 2$ mm	50
Figure 6.12	Effect of the disks separate deformation on the fluid flow in plane (r, θ) for the mode $(2, 0)$: (a) $z = 1$ mm and rotor deformation; (b) $z = 14$ and stator deformation	52
Figure 6.13	Effect of the rotor-stator coupling on the fluid flow in plane (r, θ) for the in-phase mode $(2, 0)$: (a) $z = 1$ mm; (b) $z = 14$ mm	54
Figure 6.14	Effect of the rotor-stator coupling on the fluid flow for the in-phase mode $(2, 0)$: (a) plane $(r, \theta, 0.007)$; and (b) plane $(r, 0, z)$	55
Figure 6.15	Effect of the rotor-stator coupling on the fluid flow for the out-of-phase mode $(2, 0)$: (a) $z = 1$ mm; and (b) $z = 14$ mm	56

Figure 6.16	Effect of the rotor-stator coupling on the fluid flow in plane $(r, 0, z)$ for the out-of-phase mode $(2, 0)$	57
Figure 6.17	Effect of rotation on the coupled rotor-stator configuration, considering modes $(2, 0)$, $(3, 0)$ and $(4, 0)$: (a) eigenfrequencies of $(n, 0)^{\uparrow\uparrow}$; (b) eigenfrequencies of $(n, 0)^{\uparrow\downarrow}$; (c) amplitude ratios of $(n, 0)^{\uparrow\uparrow}$; and (d) amplitude ratios of $(n, 0)^{\uparrow\downarrow}$	58
Figure 6.18	Influence of N_s and N_i on the eigenfrequencies for $c - a = 3$ mm: (a) $(2, 0)^{\uparrow\downarrow}$	60
Figure 6.19	Influence of the radial gap on the coupled rotor-stator configuration, considering modes $(2, 0)$, $(3, 0)$ and $(4, 0)$: (a) natural frequencies of $(n, 0)^{\uparrow\uparrow}$; (b) natural frequencies of $(n, 0)^{\uparrow\downarrow}$; (c) amplitude ratios of $(n, 0)^{\uparrow\uparrow}$; and (d) amplitude ratios of $(n, 0)^{\uparrow\downarrow}$	61
Figure 6.20	Effect of rotor thickness on the coupled rotor-stator configuration, considering modes $(2, 0)$, $(3, 0)$ and $(4, 0)$: (a) natural frequencies of $(n, 0)^{\uparrow\uparrow}$; (b) natural frequencies of $(n, 0)^{\uparrow\downarrow}$; (c) amplitude ratios of $(n, 0)^{\uparrow\uparrow}$; and (d) amplitude ratios of $(n, 0)^{\uparrow\downarrow}$	63
Figure 6.21	Effect of stator thickness on the coupled rotor-stator configuration, considering modes $(2, 0)$, $(3, 0)$ and $(4, 0)$: (a) natural frequencies of $(n, 0)^{\uparrow\uparrow}$; (b) natural frequencies of $(n, 0)^{\uparrow\downarrow}$; (c) amplitude ratios of $(n, 0)^{\uparrow\uparrow}$; and (d) amplitude ratios of $(n, 0)^{\uparrow\downarrow}$	64
Figure B.1	System with (a) a shaft in the lower fluid domain; and (b) a shaft throughout both fluid domains	76
Figure D.1	Rotating fixed-free annular disk coupled with a fixed-fixed annular disk	81

LIST OF SYMBOLS AND ACRONYMS

Acronyms

AVMI Added Virtual Mass Incrementor

FEA Finite Element Analysis

FEM Finite Element Method

FSI Fluid-Structure Interaction

IPCC Intergovernmental Panel on Climate Change

NAVMI Nondimensional Added Virtual Mass Incrementor

Bessel functions

Δ_n Bessel differential operator

I_n Modified Bessel function of the first kind and of order n

J_n Bessel function of the first kind and of order n

K_n Modified Bessel function of the second kind and of order n

Y_n Bessel function of the second kind and of order n

Fluid

β AVMI factor

β_0 AVMI factor without disk's rotation

$\Omega_{F/R}$ Relative angular velocity of the fluid to the rotor

\vec{V} Fluid velocity

Φ Velocity potential

ϕ Fluid displacement potential

\tilde{p} Pressure integrated on the surface of the disk

K Entrainment coefficient

p Pressure

Fluid/Structure

Γ Interface

Ω Angular velocity

ρ Density

E_i Reference kinetic energy

Index

$+n$ Co-rotating wave

$-n$ Counter-rotating wave

1 Upper fluid domain

2 Lower fluid domain

D Disk

F Fluid

P Plate

R Rotor

S Stator

s Root index from the lateral boundary conditions

V Vacuum

Mathematics

(r, θ, z) Cylindrical coordinates

δ Kronecker symbol

\mathcal{R} Residual

∇ Gradient

∇^4 Biharmonic operator

φ	Test functions
H_n	n th order Hankel transform
k	Scaling factor or root of the associated Bessel function
q	Generalized coordinates

Parameters

N_i	Number of discretization points for the fluid-disk and fluid-fluid interfaces
N_s	Number of considered terms of the sum solution to Laplace's equation
t	Instant

Structure

ν	Poisson ratio of the disks
ω	Angular frequencies
$\Omega_{R/F}$	Relative angular velocity of the rotor to the fluid
$\Omega_{S/F}$	Relative angular velocity of the stator to the fluid
A	Amplitude ratio
a	Outer radius of the rotor
b	Inner radius of the rotor
C	Modal damping
c	Radius of the confinement
D	Flexural rigidity of the disk
d	Radius of the stator
E	Young's modulus of the disks
H	Axial gap
h	Thickness
K_{nm}	Modal rigidity

M	Modal mass
m	Number of nodal circles
M_r	Bending moment
n	Number of nodal diameters
V	Maximum potential energy
V_r	Radial Kelvin-Kirchhoff edge reaction
W	Modeshapes of the disk
w	Vertical displacement of the disk

LIST OF APPENDICES

Appendix A	Separation of variables for the 3D Laplace equation in cylindrical coordinates	75
Appendix B	Confined rotor - Shaft in the lower fluid domain and shaft throughout both fluid domains	76
Appendix C	Eigenfrequencies calculation - AVMI factor and Rayleigh's coefficient	79
Appendix D	Coupling of a rotating fixed-free annular disk with a fixed-fixed annular disk	81

CHAPTER 1 INTRODUCTION

In 2015, most countries of the world signed the Paris climate agreement to keep the increase of Earth global temperature since the pre-industrial period well below 2°C and to pursue the actions to limit it to 1.5°C . According to the last report from the Intergovernmental Panel on Climate Change (IPCC), 1.1°C has already been reached and only significant cuts in greenhouse gases emissions will prevent the rise from breaking the set thresholds. One sector that will experience drastic changes is energy production, with a subsiding of fossil energies in favor of renewable energies. Existing and new hydroelectric plants will be put to new uses, as other green energies suppliers will enter the grid. Indeed, they will have to be as efficient as before and more versatile, as they will compensate the other energies intermittent output. Hydraulic turbines will thus face more transient events and off-design operating conditions, that have to be considered during their design (Trivedi et al., 2013).

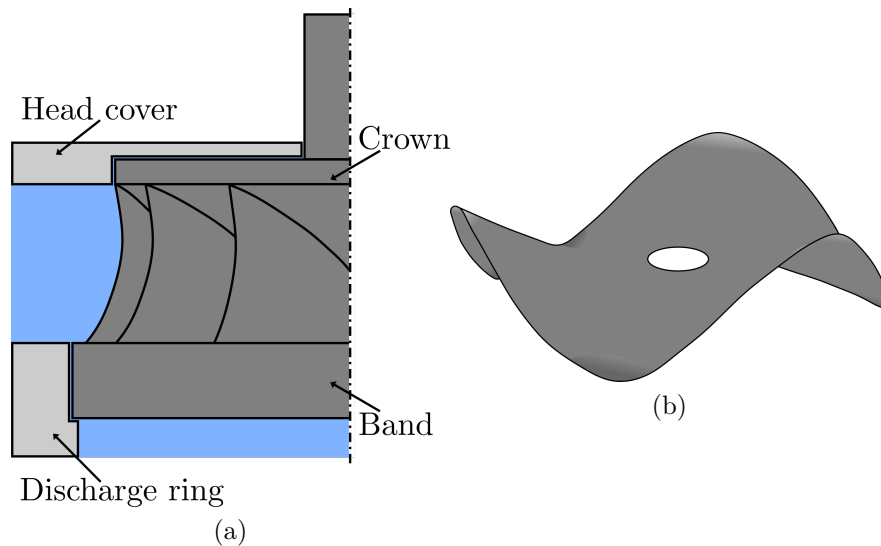


Figure 1.1 a) Schematic of a Francis turbine with the components of the stator and rotor, as well as the shaft; and b) example of a disk mode shape with $n = 3$ nodal diameters

Throughout their life, high-head turbines are subject to multiple physical phenomena that can induce severe fatigue, causing a loss in efficiency or of the turbine itself (Coutu et al., 2004, 2008). It often originates from resonance created by excitation sources, e.g. Rotor-Stator Interaction (RSI) are unavoidable in high-head Francis turbines and pump-turbines (Seidel et al., 2012). Moreover, sometimes resonance cannot be avoided and it thus become essential to determine the amplitude of vibration to ascertain if it may damage the turbine. Understanding the implied physics is therefore essential to be able to predict the dynamic

behavior of turbines. Due to their complex geometry and the fluid rotation, it has to be analyzed with a simplified approach. High-head turbines, and especially pump-turbines runners, have diametrical modes (a number of diameters, called nodal diameters, do not vibrate) for low eigenfrequencies (Egusquiza et al., 2016), and their crown and band are disk-like structures (see Figure 1.1). Hence, they can be simplified as disks, an approach that has been used in past research to qualify the involved physical phenomena, without the corresponding quantitative data.

Simplifying high-head turbines runners as disks allowed to analyze the influence of their geometry on their dynamic behavior. Runners are close to the stationary parts of turbines through small gaps filled with water, whose added mass modifies the natural frequencies of the runner. Added mass is defined as the mass of fluid oscillating with the structure. Valentín et al. (2014) studied the influence of the radial and axial gaps on the dynamic behavior of a confined stationary disk in contact with fluid on one side. The walls of the confinement are considered rigid. For both, it demonstrates that when the gap is smaller, the water added mass increases and causes the natural frequencies to decrease. Moreover, past a certain distance, the impact of rigid walls decreases and vanishes. Presas et al. (2015a) analyzed the influence of rotation on the natural frequencies of a disk in a fluid-filled rigid confinement. A stationary disk exhibits a standing wave as a mode shape, which is the superposition of two opposed traveling waves, co and counter-rotating. As the disk is stationary, the two waves superpose exactly, creating the so-called standing wave. The same phenomenon is observed when the disk rotates in vacuo or in a low-density fluid like air, as it does not have an impact on its dynamic behavior. However, when a fluid is dense, its added mass is considerable, and its movement can induce damping. Therefore, when the disk starts to rotate in a dense fluid, the two traveling waves separate (Renshaw et al., 1994). This phenomenon is called mode split, and induces the emergence of two natural frequencies associated with the forward and backward modes (see Figure 1.2). When the rotation velocity increases, their difference follows the same trend and their central value decreases slightly, which is called frequency drift. The frequency of the co-rotating wave is increased by the rotation of the fluid, while it is decreased for the counter-rotating mode (Kubota and Ohashi, 1991). When analyzing the rotation of disks in water, two reference frames are used: stationary and rotating, as the observation can be made from the stator or the rotor. When in the first one, we observe the same variation of the waves frequency described earlier, and for the latter, it is the opposite: the natural frequency of the forward mode decreases while it increases for the backward mode (Presas et al., 2015b). Indeed, in the rotating reference frame, with the rotation of the disk, the kinetic energy of the fluid increases, as well as its added mass (as it is directly proportional) for the co-rotating wave, which explains the loss in the associated

eigenfrequency. Using different reference frames is then only a matter of representation: when changing from the rotating to the stationary one, the frequency of the forward mode appears to be higher and shifts to become the highest while it is the opposite for the backward mode. Mode split for a submerged rotating disk has been analyzed experimentally, analytically and numerically by Valentín et al. (2016) and Presas et al. (2015a), and was given a physical explanation by Louyot et al. (2020).

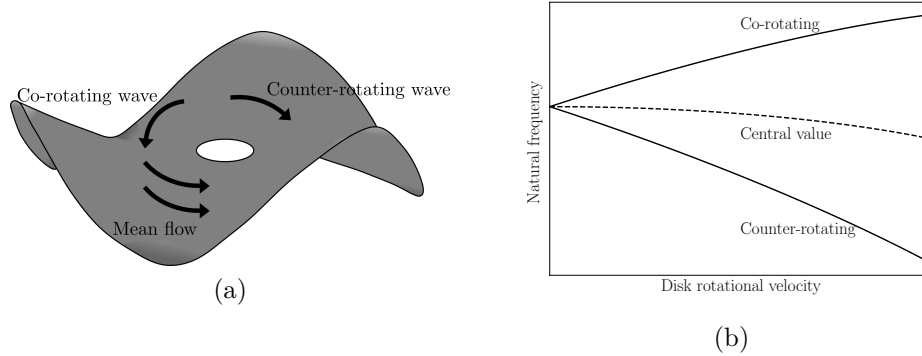


Figure 1.2 a) Mode split; and b) frequency split and drift

In hydraulic turbines, the runner is not the only component capable of vibrating due to its flexibility. Indeed, the head cover of stators is not totally rigid and Valentín et al. (2017) demonstrated that its flexibility has a significant influence on the dynamic behavior of the rotor, by coupling it with rigid and flexible covers. In fact, natural frequencies decrease when the rotor is near the rigid stator, and increase when it is near the flexible one (compared to the rigid case), if the natural frequencies in vacuo of the disk and casing are in a close range. Indeed, by being more flexible, the stator loses in rigidity and its eigenfrequencies drop to reach the range of the rotor's ones. In this case, their amplitudes are higher and the coupling is stronger. Weder et al. (2019) analyzed experimentally the coupling of the rotor with a flexible stator through the variation of their thickness and the axial gap. They first demonstrated that when two independent disk-structures are fluid-coupled, two types of modes can be distinguished depending on their relative motion. On one hand, if the modes have corresponding antinodes (e.g. upward for both for the same angle), they are said to be in-phase or sinuous (see 1.3a). On the other hand, if the modes have opposed antinodes (e.g. upward and downward for the same angle), they are said to be out-of-phase or varicose (see 1.3b). As they have different modeshapes, and the fluid flow is altered differently, they each have their own natural frequencies. Indeed, for varicose modes, the fluid is more squeezed between both structures, compared to sinuous modes, which increases its added mass and decreases the natural frequencies. In-phase modes thus have higher eigenfrequencies than

out-of-phase modes. Weder et al. (2019) also showed that the stator has an impact on the dynamic behavior of the rotor with the integration of the fluid rotation, an addition to the work of Valentín et al. (2017). One significant observation is that the amplitude ratio between the rotor and the stator is also influenced by the rotation. Therefore, mode split has to be analyzed when the rotor is coupled with a flexible stator.

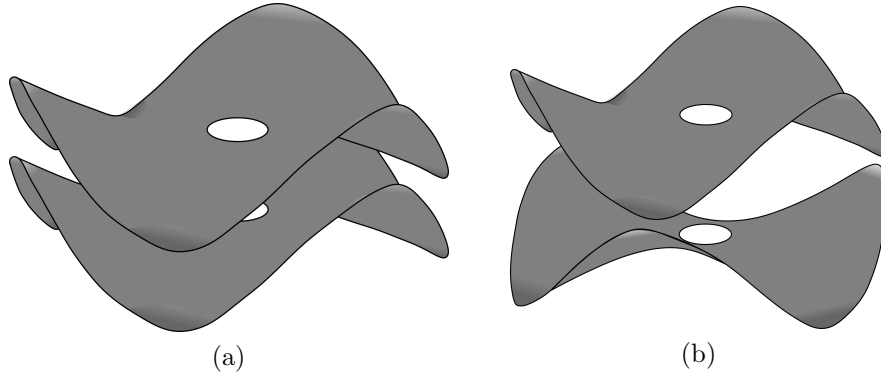


Figure 1.3 (a) In-phase modes; and (b) out-of-phase modes with $n = 3$ nodal diameters for two identical annular disks

This project was done in collaboration with Andritz Hydro Canada Inc., based in Montréal, Canada. The previous work of Louyot et al. (2020), also made in partnership with this company, analyzed the dynamic behavior of a rotating annular disk submerged in a rigid confinement and gave physical insights on the mode split phenomenon. As the stator is also part of the vibrating structure, integrating its coupling with the stator and considering the mode split is thus of interest for Andritz Hydro Canada Inc. Indeed, extending the analytical and numerical models developed by Louyot et al. (2020) would provide a better understanding and prediction of these phenomena, essential in the early stages of hydraulic turbines' design.

In this thesis, we first review the available literature to build corresponding research objectives complementing the past work and acting as guidelines for our project. We then present the methodology of our analytical and numerical models, through the establishment of the assumptions, the calculation and simulation steps. Afterwards, we verify and validate our methods with results from different theoretical approaches and experimental data, before analyzing the implied physics through parametric studies. We finally conclude on our work based on the objectives set, by additionally giving its limitations and an outlook of the future work that could be done.

CHAPTER 2 LITERATURE REVIEW

Through extending the analytical and numerical models developed by Louyot et al. (2020), our work features two physical phenomena: the mode split and the rotor-stator coupling. Both of them have been analyzed in detail in the past by Louyot et al. (2020) and Weder et al. (2019), and here we further describe the insights they made.

Mode split phenomenon

Although the mode split phenomenon was first introduced by Kubota and Ohashi (1991), reproduced numerically by Valentín et al. (2016) and observed experimentally by Presas et al. (2015a), it lacked a physical understanding. Louyot et al. (2020) thus developed analytical and numerical models to represent the crown of the runner with a rotating annular disk submerged in rigid confinement. Using β the Added Virtual Mass Incremental (AVMI) factor, it is possible to evaluate the natural frequencies of the disk in water ω_F with those in vacuum ω_V (Kwak and Kim, 1991):

$$\frac{\omega_F}{\omega_V} = \frac{1}{\sqrt{1 + \beta}}, \quad (2.1)$$

where β is defined as the ratio of the kinetic energies of the fluid and the disk. Louyot et al. (2020) then expressed β as a function of β_0 the AVMI factor without rotation of the fluid:

$$\beta = \left(1 + \frac{n\Omega_{D/F}}{\omega_F}\right)^2 \beta_0, \quad (2.2)$$

with n the number of nodal diameters and $\Omega_{D/F}$ the relative angular velocity of the disk to the fluid (as the referential is the fluid reference frame). Their theoretical approach finally lead to a formula to calculate the eigenfrequencies ω_F with ω_V , β_0 and $\Omega_{D/F}$:

$$\omega_F = \frac{\sqrt{(\beta_0 + 1)\omega_V^2 - \beta_0(n\Omega_{D/F})^2} - n\beta_0\Omega_{D/F}}{\beta_0 + 1}. \quad (2.3)$$

The definition of β corroborates the explanation of the added mass given by Paidoussis (2014), as he associates the fluid loading with accelerations of the structure (and in turn those of the fluid). Moreover, it allows us to understand the effect of the added mass on the natural frequencies: if it is increased, the ratio between eigenfrequencies in water and in vacuo is reduced, resulting in lower natural frequencies in fluid. On the contrary, if the

added mass effect is less considerable, the ratio between eigenfrequencies in water and in vacuo increases, leading to higher natural frequencies in fluid. This behavior is similar to the one displayed by a mass-spring system. Indeed, without fluid, increasing the rigidity of the spring causes a rise in eigenfrequencies, whereas increasing the mass results in a reduction of the natural frequencies. The added mass of the fluid is thus combined with the mass of the structure and has the same influence as increasing the mass of the structure. Louyot (2019) also demonstrated that the natural frequencies of the disk in water decrease for smaller axial gaps and/or when the disk is larger and thinner, as he observed the opposite trend for β_0 . The eigenfrequencies increase with the number of nodal diameters and circles.

In the rotating reference frame, the disk rotation decreases the frequency of the co-rotating wave while it increases the frequency of the counter-rotating wave. In addition, the number of nodal diameters $n > 0$ and $n < 0$ respectively correspond to the forward and backward modes. Therefore, the term responsible for the mode split phenomenon is identified in Eq. (2.3) found by Louyot (2019) as $-n\beta_0\Omega_{D/F}$. From this observation, it is possible to write the mode split magnitude as:

$$\omega_{F,-n} - \omega_{F,+n} = \frac{2n\beta_0\Omega_{D/F}}{\beta_0 + 1}. \quad (2.4)$$

Therefore, by increasing β_0 , the mode split magnitude tends towards the asymptotic value of $2n\Omega_{D/F}$. The other phenomenon observed with the rotation of the disk is the frequency drift. According to Eq. (2.3), it originates from the term $-\beta_0(n\Omega_{D/F})^2$ as it decreases the natural frequencies no matter which wave is concerned (the sign of n has no influence with the square). Louyot (2019) showed that the drift is negligible for angular velocities of the disk corresponding to those of hydroelectric runners under operating conditions. By increasing sufficiently the rotational velocity (and thus getting outside the operating range of turbines), the natural frequencies become complex values and an unstable coupling between the disk motion and the pressure of the fluid is triggered, resulting in a coupled-mode flutter instability.

Rotor-stator coupling

For the coupling of the rotor crown and the stator head cover (see Figure 1.1), Weder (2018) showed that, in addition to the rotor, stator and fluid forming a vibrational system on its own, the viscous dissipation of the fluid acts as the dominant damping mechanism when there is no disk rotation. This could explain discrepancies between experimental data and results from analytical models assuming inviscid flow. To further explain the difference between the frequencies of the varicose and sinuous modes, and to also refer to the definition of the added

mass done by Paidoussis (2014), Weder (2018) demonstrated that the more considerable squeezing of the fluid for out-of-phase modes results in in-plane accelerations of the fluid, which in turn increase the modal mass of the vibrating system. Weder (2018) also did multiple studies on the variation of the parameters of the system, such as the axial gap, the thickness of the rotor and stator, as well as the rotation. As for the annular disk submerged in rigid confinement, reducing the axial gap causes a decline in the eigenfrequencies of the in-phase and out-of-phase modes. Indeed, smaller gaps increase the squeezing effect between the rotor and the stator, and the added mass of the fluid also rises in this case. Reducing the axial gap also decreases the amplitude ratio of the rotor to the stator for varicose modes, while it slightly increases for sinuous modes. Weder (2018) also observed that the natural frequencies of the in-phase modes are sensitive to the increase of the thickness ratio (defined as the quotient of the thicknesses of the rotor and stator), whereas it is its decrease for the out-of-phase modes. For an increasing thickness ratio, the amplitude ratios of the varicose mode considerably decline, while they are nearly constant for the in-phase modes. When the rotor is rotating, Weder (2018) describes that the natural frequencies of the system split and drift, as is observed when the stator is considered rigid. As for the amplitude ratio, an increasing rotational velocity reduces it slightly for most of the modes.

Past analytical models

The coupling between the rotor crown and the stator head cover (see Figure 1.1) can be idealized as a rotating annular disk and a stationary circular disk coupled through fluid. Leissa (1969) describes the dynamic behavior of such plates in vacuo with different boundary conditions, with theory from the earlier work of Southwell (1922) and Vogel and Skinner (1965). Lamb (1920) first studied the fluid-structure interaction of a circular plate clamped to a rigid and infinite wall, in contact on one side with infinite fluid by using the method introduced by Rayleigh (1877). Along with the potential flow theory, the fluid is assumed irrotational and inviscid, as is the case for the following studies. It is also assumed incompressible in this work. Rayleigh (1877), along with Lamb (1920), are at the origin of the Rayleigh quotient for coupled vibration, developed by Zhu (1994), used to calculate the natural frequencies of plates in contact with fluid. Indeed, using Rayleigh's quotient, the eigenfrequencies of the plates in vacuo ω_V and those in fluid ω_F can be expressed as:

$$\omega_V^2 = \left(\frac{V_P}{E_P} \right)_V \quad \text{and} \quad \omega_F^2 = \left(\frac{V_P}{E_P + E_F} \right)_F, \quad (2.5)$$

where V_P is the maximum potential energy, E_P and E_F the reference kinetic energies of the plate and the fluid, respectively. Assuming that the modeshapes of the plate are the same in fluid as in vacuo, the energies of the plate in both media can be considered equal, leading to (Lamb, 1920):

$$\omega_F = \frac{\omega_V}{\sqrt{1 + \frac{E_F}{E_P}}}, \quad (2.6)$$

where we recognize the formula from Eq. (2.3), which links the natural frequencies of the plate in fluid and in vacuo, with the AVMI factor $\beta = E_F/E_P$. The Non-dimensional AVMI (NAVMI) factor was later introduced by Kwak and Kim (1991), defined as:

$$\Gamma = \beta \frac{\rho_P h}{\rho_F a}, \quad (2.7)$$

with ρ_P and ρ_F the densities of the plate and the fluid, respectively, h the thickness of the plate and a its radius. Amabili and Kwak (1996) revised the problem of Lamb (1920), employing the NAVMI factor and comparing it with the more accurate Rayleigh-Ritz approach. The latter is indeed considered more accurate as it removes the assumption that the modeshapes in fluid are the same in vacuo. It does so by introducing wet modeshapes defined as the linear combination of admissible functions multiplied by unknown Ritz coefficients. The eigenfunctions of the plate vibrating in vacuo are used as admissible functions, as the dry modeshapes are similar to the wet ones. As the flow is potential, it is solution to Laplace's equation and Amabili and Kwak (1996) used the Hankel transform to solve it. To explain the use of this operation, as it is employed by other references, we briefly define it here. According to Piessens (2000), the n th order Hankel transform H_n of the function $f(r)$ defined for a variable $r \geq 0$ is:

$$F_n(k) = H_n \{f(r)\} = \int_0^\infty r f(r) J_n(kr) dr, \quad (2.8)$$

where J_n is the Bessel function of the first kind and of order n and k the scaling factor. Applying the separation of variables to Laplace's equation in cylindrical coordinates gives the Bessel differential operator Δ_n , whose Hankel transform with an arbitrary function $f(r)$ such that $\lim_{r \rightarrow \infty} f(r) = 0$ displays an interesting property:

$$H_n \{\Delta_n f(r)\} = -k^2 H_n \{f(r)\}, \quad (2.9)$$

making it useful for problems with polar symmetry and involving the Laplacian operator. As the fluid domain is infinite and the fluid displacement potential is null far from the plate, Amabili and Kwak (1996) could use this property to reduce Laplace's equation to

an ordinary differential equation. Once solved, they used the inverse Hankel transform to get the expression of the potential. The NAVMI factor is employed again, through the use of the Rayleigh quotient and its minimization, which is not a real scalar but a matrix in this case, given the combination of dry modeshapes considered. Amabili and Kwak (1996) also considered other configurations, with different boundary conditions to prove that the assumed-mode approach is accurate, when compared to the Rayleigh-Ritz method. Amabili et al. (1996) analyzed the free vibrations of annular plates in contact on one side with infinite dense fluid. The fluid-structure interaction is solved once again with the Hankel transform and the natural frequencies are obtained with the assumed-mode approach, through the AVMI factor, and the Rayleigh-Ritz method. Amabili et al. (1996) showed once more that using the AVMI factor is as precise as employing the Rayleigh-Ritz method for the first modes. This was also demonstrated by Amabili (1996) for circular and annular plates in contact with confined fluid, either by a rigid wall or a free surface. Kubota and Ohashi (1991) first studied the interaction of a stationary annular disk submerged in an annular and cylindrical tank filled with rotating fluid. They observed the split of frequencies, that they validated with an experimental setup. Presas et al. (2015a) integrated the rotation for a disk with an average radius in a fluid-filled confinement by dividing the fluid in two subdomains above and below the disk. Both fluid domains rotate at a different velocity, obtained through a Computational Fluid Dynamics (CFD) simulation of the disk rotating in a viscous fluid. Once the potential velocity of the fluid has been determined, Presas et al. (2015a) use Euler's momentum equation for an incompressible ideal fluid to evaluate the pressure on the disk, and introduce it in the equation of motion given by Leissa (1969):

$$D\nabla^4 w + \rho_P h_P \frac{\partial^2 w}{\partial t^2} = p(r, \theta, t), \quad (2.10)$$

where D is the flexural rigidity, ∇^4 the biharmonic operator, w the vertical displacement of the plate, t the instant and p the pressure. Due to its simplifications, their model is only able to assume modes with no nodal circles and $n \geq 2$ nodal diameters, with no radial gap. Their experimental data could be used to validate analytical models, and their configuration is given in Table 2.1. Louyot et al. (2020) reproduced their model without assuming an average radius to better explain the mode split, while also not considering a radial gap. They used the same approach as Amabili et al. (1996), with the difference that they employed the Galerkin method to write the vertical displacement as a linear combination of test functions (dry modeshapes) multiplied with the generalized coordinates. It is similar to the beginning of the Rayleigh-Ritz method, but, while the latter minimizes the Rayleigh quotient, Galerkin's method minimizes the weighted average error once the assumed solution has been integrated.

Louyot et al. (2020) then used the orthogonality of the modeshapes to uncouple each mode. In their work, the fluid rotates as a solid body at a fraction of the disk angular velocity, defined with the entrainment coefficient K , empirically determined by Poncet et al. (2005, 2007).

Kerboua et al. (2008) modeled the coupling of rectangular plates with fluid, with different boundary conditions such as a rigid wall and a free surface. They used an hybrid approach to represent the structure, combining Finite Element Method (FEM) and classical shell theory, while they applied the potential flow theory for the fluid. They determined the pressure at the fluid-structure interface with Bernoulli's equation, and combined it with the deformed shape of the plate to evaluate the virtual added mass of the fluid. Similarly, Askari et al. (2013) simulated a circular disk in a partially-filled confinement with a free surface. The wet modeshapes are represented with a Ritz function, and they used the linear least-squares method to discretize the fluid-disk interface, allowing for the integration of the radial gap. They also considered the deformation of the disk and the free surface separately, using the superposition principle, which they then coupled in Rayleigh's coefficient. The boundary conditions at the fluid-fluid interface are critical for the representation of the implied physics, and Lee et al. (2016) provide additional details on the method used by Askari et al. (2013). Indeed, they simulate the sloshing of a fluid in a cylindrical casing with a partially submerged rigid cylindrical body at its center. A radial gap is thus formed this way and the fluid is divided in multiple subdomains depending on its boundaries. Jeong (2003, 2006) analyzed analytically and numerically the dynamic behavior of fluid-coupled circular and annular plates respectively. The circular disks are identical, while the annular plates have different inner radius and thickness. They also used the Rayleigh-Ritz method, but used different approaches to solve Laplace's equation. Indeed, Jeong (2003) used the Fourier-Bessel series to expand the Bessel functions of the modeshapes, and simplify the representation of the fluid-structure interaction between the disks and the fluid. This method is relevant for this configuration as the axial symmetry of the problem allows for special boundary conditions related to the in-phase and out-of-phase modes. Jeong (2006) used for his asymmetric configuration the finite Hankel transform, similarly to Amabili and Kwak (1996). Instead of using displacements and forces, Weder (2018) used strains and stresses from continuum mechanics to model the rotor-stator coupling, along with an experimental setup. Their experimental results could indeed be used to validate analytical models as they analyzed the influence of the axial gap, the thicknesses and the rotation on the rotor-stator coupling. Representation of the three models are available in Table 2.1.

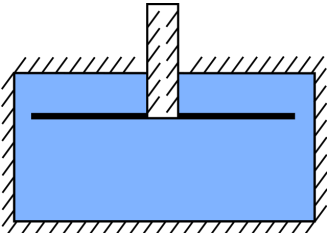

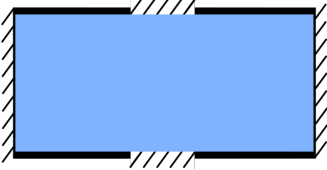
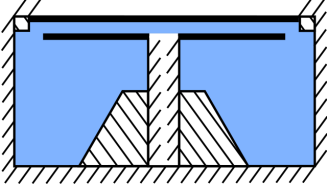
Past numerical models

Analytical methods alone are not able to completely reproduce the complexity of hydraulic turbines. Therefore, in the industry, numerical models to predict the dynamic behavior of such structures are used. One of the most used is the two-way fluid-structure coupling that computes and couples simultaneously the fluid and the structure (Dompierre and Sabourin, 2010). To do that, it links a CFD model with a Finite Element Analysis (FEA). This method was used under Ansys by Hengstler (2013) to predict the natural frequencies of standing and submerged circular plates, while Weber and Seidel (2015) also integrated rotation to reproduce the model of Presas et al. (2015a). Employing COMSOL, Specker (2016) modeled a disk-fluid-disk system, whereas Weder et al. (2019) added bias motion to study mode split in the rotor-stator coupling. Due to the iteration of two separate models, fully-coupled fluid-structure simulation yields precise results but is computationally expensive (Hübner et al., 2016). Moreover, it lacks stability and the data exchange between the solvers is a considerable issue (Biner, 2017). There are two types of schemes used for Fluid-Structure Interaction (FSI) analysis: monolithic and partitioned. While the first one solves the entire coupled problem as one system of equations in one iteration, the second one is used in most cases, requiring a lot of subiterations to be performed at each time step, to achieve convergence. Divergence may occur in this process when a strong interaction is involved. Being time-consuming and divergent, simpler methods have been sought for, such as one way coupled FSI. In case of small amplitude deformation and large structural time scales, pressure and forces from the CFD simulation can be applied as boundary conditions to the structure to obtain strains and stresses. The opposite can also be done, where the structural motion is imposed to the fluid in the flow simulation to get its reaction forces, and in turn the structural strain. This process is employed by the modal approach (which is an alternative to two-way coupled FSI), with the structural modeshape as input. It can either use the modal work, where the hydrodynamic damping and frequency shifts are obtained through the energy exchange between the structural motion and the flow, or the modal force, in which a single degree of freedom oscillator model couples a CFD model with a code calculating the displacement of the disk with the surrounding fluid parameters and pressure field. The latter was developed to predict the hydrodynamic damping and added stiffness of runner blades in flowing water by Monette et al. (2014) and Nennemann et al. (2016), and compared with the first method. Biner (2017) used the modal work approach to predict the dynamic behavior of a rotating disk submerged in rigid confinement. Louyot et al. (2020) extended the modal force approach to the same system to build a fast eigenfrequencies prediction model. However, parasitic high frequencies of vibration limit its range of prediction to low rotation speeds. Moreover, each

mode has to be studied separately as its modeshape is imposed as an initial condition to get the free vibrations of the structure.

Alternatively, Presas et al. (2015a,b, 2016) used acoustic-structural FSI coupling with modal analysis, which applies FEA to both the structure and the fluid, as it is considered acoustic (inviscid and irrotational). Rodriguez et al. (2012) validated this method experimentally, as acoustic-structural modal analysis showed to predict natural frequencies of submerged plates close to a rigid wall with an accuracy of 2.5%. Valentín et al. (2016) also showed the capability of this analysis to model rotating disks submerged in dense fluid, by reproducing the experimental setup of Presas et al. (2014a,b, 2015a,b,c, 2016) with precise results. They also describe in detail the approach to follow, as well as the reference frame to do the calculations in. Hengstler (2013) simulated the coupling of two disks through fluid using this method under Ansys, a system similar to the one of Jeong (2003).

Table 2.1 Summary of all the studies that could be used as validation

Name	Description	Schematic
Confined rotor	Fixed-free annular disk in fluid-filled and rigid confinement from Presas et al. (2015a)	
Coupled static disks	Identical free-fixed circular disks coupled with fluid from Jeong (2003)	
Coupled static annuli	Fixed-fixed annular disks coupled with fluid from Jeong (2006)	
Coupled rotor-stator	Free-fixed circular disk and fixed-free annular disk coupled by fluid in rigid confinement from Weder (2018)	

CHAPTER 3 RESEARCH OBJECTIVES

High-head hydraulic turbines and pump-turbines present dynamic behavior similar to disks for low frequencies (Egusquiza et al., 2016). Using this simplified model, the implied physics, such as RSI, have been thoroughly analyzed in the past research. More specifically, the mode split phenomenon occurring for a rotating submerged disk was observed experimentally by Presas et al. (2015a). Valentín et al. (2016) simulated it numerically using acoustic-structural modal analysis to study the influence of the fluid flow and the reference frame. Louyot et al. (2020) developed an analytical modal analysis of the disk to provide a better understanding of the basic mechanisms at play and the essential parameters. Louyot et al. (2020) used the Galerkin method to consider each assumed-mode, and the Hankel transform to represent the fluid-structure interface, as well as the AVMI factor to evaluate the natural frequencies. While mode split was well explained, the analytical model lacks the integration of one geometrical characteristic: the radial gap. It was implemented in another method developed by Askari et al. (2013), but for a non-rotating submerged disk. Each mode is considered separately as a Ritz function, the flexible fluid-structure interface is discretized using the linear least-squares method and the eigenfrequencies are calculated with Rayleigh's quotient.

In turbines, not only the runner is flexible and subject to excitation, as it is also the case for the thin upper cover of the stator. Valentín et al. (2017) demonstrated experimentally that, depending on its flexibility, the stator may vibrate and be coupled through the fluid with the rotor. Askari et al. (2013) were able to couple the deformation of a submerged disk with a free surface, by applying the superposition principle on the flows calculated for each deformation. Jeong (2003) made an analytical model of the coupling of two identical disks through fluid, using the Hankel transform and the Rayleigh-Ritz method. Hengstler (2013) simulated numerically the same configuration under Ansys using an acoustic-structural modal analysis. Jeong (2006) completed his work with the same approach for fixed-fixed annular disks with different thickness and inner radius. Weder et al. (2019) integrated experimentally the rotation, and determined that it influences the rotor-stator coupling, and the amplitude ratio between both disks. Many experiments were conducted on the interaction of disks and annuli through still or rotating fluid. They are schematized in Table 2.1.

From the literature review, we can formulate three research objectives for this project and the associated thesis (summarized in Table 3.1):

- Analyze analytically the dynamic behavior of the rotation of the rotor crown, as a

rotating fixed-free annular disk submerged in a dense fluid and confined with a radial gap in a rigid casing. For the structural calculations (when the system is placed in vacuo or air), apply the Galerkin method, based on the assumed-mode approach, as Louyot (2019) did. When fluid is added in the confinement, discretize the moving fluid-structure interface with the point collocation method as Askari et al. (2013). Validate the results with experimental data from Presas et al. (2015a) and analyze the influence of multiple characteristics on the dynamic behavior of the rotor.

- Model the coupling of the rotor with the head cover of the stator, simplified as a clamped circular disk. To integrate the rotor-stator coupling, consider separately each component deformation before coupling them through the equations of motion, using the superposition principle as Askari et al. (2013) did. Verify the model step by step with data from different analytical models from Jeong (2003, 2006). Validate the results with experimental measurements of Weder (2018), as well as employ them to study the influence of rotation and thickness ratio on the behavior of the rotor-stator coupling.
- Develop a Finite Element Method (FEM) model under Ansys to perform an acoustic-structural modal analysis of the rotor-stator coupling with stationary and rotating disks. Recreate the model for the confined rotor from the work of Presas et al. (2015a) and Valentín et al. (2016). Add the stator, and validate the results with experimental data from Weder (2018). Verify the corresponding analytical methods with this model, mainly developed by Blais (2021), especially for the lone rotor.

Table 3.1 Summary of the research objectives

Model	Objectives	Verification	Validation
Analytical	Analyze the dynamic behavior of a rotating fixed-free annular disk submerged in a dense fluid and confined with a radial gap in a rigid casing	FEM model	Presas et al. (2015a)
Analytical	Model the coupling through fluid of a fixed-free annular disk with a clamped circular disk	FEM model, Jeong (2003) and Jeong (2006)	Weder (2018)
FEM	Develop an acoustic-structural modal analysis under Ansys of the rotor-stator coupling with stationary and rotating disks	Analytical model, Presas et al. (2015a), Jeong (2003, 2006)	Presas et al. (2015a) and Weder (2018)

CHAPTER 4 METHODOLOGY - ANALYTICAL MODEL

In this section, we describe the approach used to build the analytical forced modal analysis. In addition to considering the turbine rotor and stator as rotating and stationary disks, we use the following assumptions:

1. We consider small amplitude deformations of the disks to apply linear perturbation theory.
2. The disks only deform in the axial direction, even when rotating, due to the low rotation speeds range (the gyroscopic effect and the centrifugal forces are negligible).
3. We apply the potential flow theory to the fluid, such that it is considered inviscid and irrotational, in addition to incompressible.
4. The fluid rotates as a solid body with a mean velocity equal to a fraction of the disk rotation speed, when viewed from the rotating disk reference frame. The value of the fraction is given empirically by Poncet et al. (2005, 2007).
5. We use the assumed-mode approach, which states that the disks modeshapes are the same in water as in vacuo. It was proved accurate for multiple configurations by Amabili et al. (1996), Amabili and Kwak (1996), and Amabili (1996) with the Rayleigh-Ritz method.

The rotor is represented by a fixed-free¹ rotating annular disk of density ρ_D ², inner radius b , outer radius a and thickness h_R . It is rotating with an angular velocity Ω_R in the stationary reference frame. The rotor is clamped at its inner radius to a rigid shaft of the same thickness. The stator is represented by a fixed circular disk of the same material as the rotor, an outer radius d and a thickness h_S . We use the cylindrical coordinates (r, θ, z) in the stationary reference frame, with its origin at the center of the rotor. The latter and the stator share the same central axis z and are separated by an axial gap H_1 . Both are placed in a casing of diameter c , which is considered rigid and filled with a fluid of density ρ_F , and the rotor is placed at a distance H_2 above the lower surface of the confinement. The stator is part of the upper wall of the casing, thus the latter has an overall height of $H_1 + H_2$. Figure 4.1 schematizes the modeled geometry.

The model is developed in two steps, as described in the research objectives:

¹Throughout the thesis, boundary conditions are listed starting from the center to the edge of the disk.

²The index is set to D to differentiate with the fluid density and as both disks have the same density.

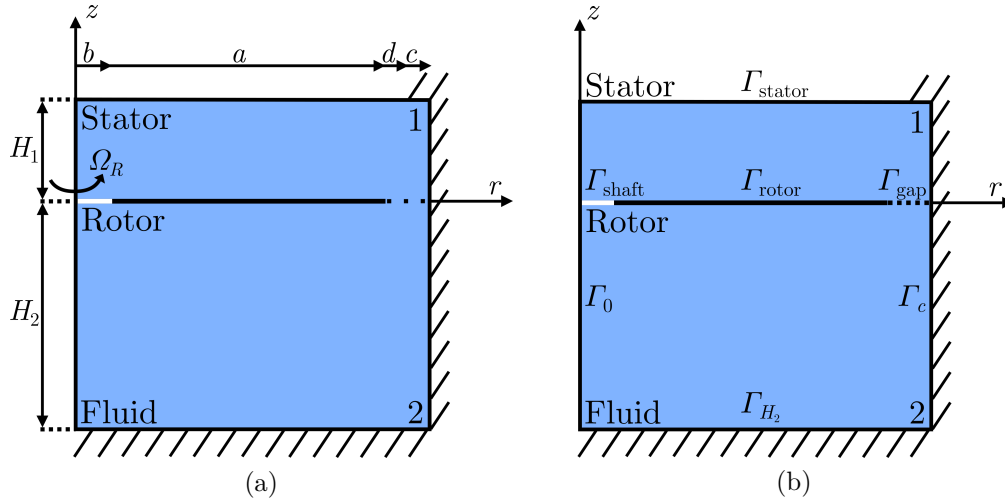


Figure 4.1 a) Geometry of a rotor and a stator in a fluid-filled tank; and b) interfaces between the fluid and the structure composed of the rotor, stator and confinement

- We first integrate the radial gap, to better reproduce the system of Presas et al. (2015a), as their experimental data is used to validate our model. The stator is considered rigid, and the rotor is the only vibrating structure, as can be seen on Figure 4.2a.
- We then implement the rotor-stator coupling, by no longer assuming the stator as rigid (see Figure 4.2b). The results are compared with experimental data from Weder (2018).

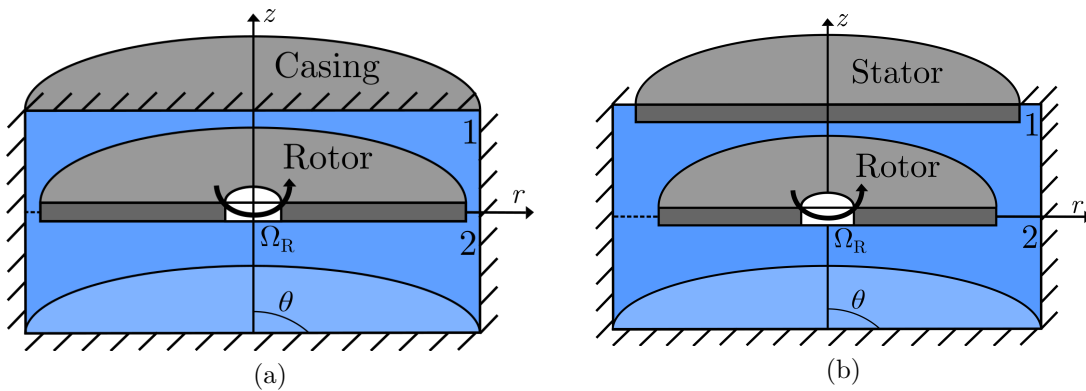


Figure 4.2 a) Schematic of a flexible rotating annular disk - the rotor - in a rigid confinement similar to the experiments of Presas et al. (2015a); and b) schematic of the system coupling a flexible rotating annular disk - the rotor - with a flexible non-moving casing - the stator - similar to the experiments of Weder et al. (2019)

Submerged annular disk in rigid confinement

Structural model

We use the same approach as Louyot (2019), therefore we will briefly describe it. According to Leissa (1969), the transverse displacement w of a disk is given by:

$$D\nabla^4 w + \rho_D h \frac{\partial^2 w}{\partial t^2} = p(r, \theta, t), \quad (4.1)$$

where D is the flexural rigidity (or bending stiffness) of the disk defined as $D = Eh^3/(12(1 - \nu^2))$ (with E the Young's modulus and ν the Poisson ratio of the disk material), ∇^4 is the biharmonic operator, t the instant and p the pressure field applied to the disk. The structural parameters associated to the disk are written with no index to lighten the equations. For the rotor-stator coupling, the indexes R and S are used to differentiate the disks representing respectively the rotor and stator.

The vertical displacement w in vacuo is composed of all the modeshapes of the disk, with n and m the numbers of nodal diameters and circles respectively:

$$w(r, \theta, t) = \sum_{n=0}^{\infty} \sum_{m=0}^{\infty} W_{nm}(r, \theta) e^{i\omega_V t}, \quad (4.2)$$

where ω_V and W_{nm} are the angular natural frequency and modeshape in vacuo, respectively. For a single mode of an annular disk, and using the Fourier decomposition in θ , the associated modeshape may be expressed as:

$$W_{nm}(r, \theta) = \psi_{nm}(r) e^{in\theta}, \quad (4.3)$$

where

$$\psi_{nm}(r) = A_n J_n(k_{nm}r) + B_n Y_n(k_{nm}r) + C_n I_n(k_{nm}r) + D_n K_n(k_{nm}r), \quad (4.4)$$

with J_n , Y_n , I_n and K_n the Bessel functions of the first and second kind, and the modified Bessel functions of the first and second kind respectively. We introduce k_{nm} as $k_{nm} = \rho_D h \omega_V^2 / D$ to later determine W_{nm} . The complex part of $e^{in\theta}$, i.e. $i \sin n\theta$, is not needed when the disk is stationary, as its boundary conditions are axisymmetric. Indeed, the co and counter-rotating waves are exactly superposed and are represented by $\cos n\theta$ and $\sin n\theta$, respectively. When the rotation is integrated, and the waves are out of phase, it is still not necessary to include it either, as all the terms in θ disappear, whether it is in the first or the second model.

The boundary conditions for a fixed-free annular disk are such that (Leissa, 1969)

$$W_{nm}(r, \theta)|_{r=b} = 0, \left. \frac{\partial W_{nm}(r, \theta)}{\partial r} \right|_{r=b} = 0, \quad (4.5)$$

$$V_r(r, \theta)|_{r=a} = 0, M_r(r, \theta)|_{r=a} = 0, \quad (4.6)$$

where V_r is the radial Kelvin-Kirchhoff edge reaction and M_r the bending moment:

$$V_r = -D \left[\frac{\partial}{\partial r} (\nabla^2 W_{nm}(r, \theta)) + (1 - \nu) \frac{1}{r} \frac{\partial^2}{\partial \theta \partial r} \left(\frac{1}{r} \frac{\partial W_{nm}(r, \theta)}{\partial \theta} \right) \right] \quad (4.7)$$

$$M_r = -D \left[\frac{\partial^2 W_{nm}(r, \theta)}{\partial r^2} + \nu \left(\frac{1}{r} \frac{\partial W_{nm}(r, \theta)}{\partial r} + \frac{1}{r^2} \frac{\partial^2 W_{nm}(r, \theta)}{\partial \theta^2} \right) \right]. \quad (4.8)$$

V_r represents the shear force at the edge of the plate under Kirchhoff-Love (or thin plates) theory, resulting from the addition of the out-of-plane shear force and the force created by the twisting moment.

When substituting Eq. (4.7) and (4.8) for V_r and M_r in the four boundary conditions of Eq. (4.5) and (4.6), we obtain the eigenvalue problem:

$$\mathbf{M} \cdot \mathbf{X}_n = \begin{bmatrix} a_i & \cdots & d_i \\ \vdots & \ddots & \vdots \\ a_{iv} & \cdots & d_{iv} \end{bmatrix} \cdot \begin{bmatrix} A_n \\ B_n \\ C_n \\ D_n \end{bmatrix} = 0 \quad (4.9)$$

The first step is to find the eigenvalues k of this problem by solving $\det(M) = 0$. There is an infinite number of solutions for any number of nodal circles m , and, if we remove the trivial solution $k = 0$, the next one corresponds to $m = 0$. This has to be done numerically, with a Python code³. This code has been used to support all the calculations of the analytical model. Once the eigenvalues are determined, we can evaluate the eigenvectors composed of A_n , B_n , C_n and D_n . First, A_n is fixed arbitrarily with the value 1 to determine the three other terms and have the modeshapes form an orthonormal base (as it is naturally orthogonal).

To then apply the Galerkin method to Eq. (4.1), the displacement is approximated with a discrete sum (for more details, see Louyot (2019)):

$$w(r, \theta, t) \approx w_N(r, \theta, t) = \sum_j^N \varphi_j(r, \theta) q_j(t), \quad (4.10)$$

³https://github.com/lm2-poly/rotor-stator_coupling_split

where N is the number of considered modes with different nodal diameters, φ_j are test functions satisfying the boundary conditions (chosen to be equal to the orthonormal modeshapes W_j) and q_j the generalized coordinates. We replace w with w_N in Eq. (4.1):

$$D\nabla^4 w_N + \rho_D h \frac{\partial^2 w_N}{\partial t^2} - p_N(r, \theta, t) = \mathcal{R}, \quad (4.11)$$

where \mathcal{R} is the residual. By substituting w_N with Eq. (4.10), and by observing that $\nabla^4 W_j = k_j^4 W_j$:

$$\sum_j^N \left[\rho_D h \frac{\partial^2 q_j(t)}{\partial t^2} + D k_j^4 q_j(t) \right] W_j(r, \theta) - p_j(r, \theta, t) = \mathcal{R}. \quad (4.12)$$

According to Galerkin's method:

$$\int_{r=b}^a \int_{\theta=0}^{2\pi} \mathcal{R} W_i(r, \theta) r dr d\theta = 0 \quad \forall i \leq N. \quad (4.13)$$

As the modes are orthonormal,

$$\int_{r=b}^a \int_{\theta=0}^{2\pi} W_i(r, \theta) W_j(r, \theta) r dr d\theta = 2\pi (a^2 - b^2) \delta_{ij}, \quad (4.14)$$

where δ_{ij} is the Kronecker symbol. By multiplying Eq. (4.12) with W_i , and then integrating over the annular disk surface, we get:

$$2\pi (a^2 - b^2) \sum_j^N [\rho_D h \ddot{q}_j(t) + D k_j^4 q_j(t)] \delta_{ij} = \int_b^a \int_0^{2\pi} p_j(r, \theta, t) W_i r dr d\theta. \quad (4.15)$$

We notice that each equation representing a single mode can be decoupled from the system, and by generalizing for any chosen mode, we derive the equation solved by the vertical displacement w :

$$M \ddot{w}(t) + K_{nm} w(t) = \tilde{p}_{nm}(t) \quad (4.16)$$

where $M = 2\pi(a^2 - b^2)\rho_D h$, $K_{nm} = 2\pi(a^2 - b^2)Dk_{nm}^4$ and $\tilde{p}_{nm}(t) = \int_b^a \int_0^{2\pi} p(r, \theta, t) W_{nm}(r, \theta) r dr d\theta$. Eq. (4.16) can be assimilated as the equation governing the vertical motion of a one degree-of-freedom mass-spring system.

The natural angular frequency of the annular disk in vacuo may be evaluated with Eq. (4.16) when $\tilde{p}_{nm}(t) = 0$:

$$\omega_V = \sqrt{\frac{K_{nm}}{M}} = k_{nm}^2 \sqrt{\frac{D}{\rho_D h}}. \quad (4.17)$$

Fluid model

As one can observe in Figure 4.2, the fluid domain is divided in two subdomains: the upper and lower fluid regions. The superior and inferior faces of the annular disk are in contact with the fluid. The oscillatory fluid flow of both subdomains can be described by a velocity potential, solution of Laplace's equation in cylindrical coordinates:

$$\nabla^2 \Phi = 0. \quad (4.18)$$

As the time-dependence is considered harmonic, the velocity potential function Φ may be separated in a product of a displacement potential ϕ and a harmonic time function:

$$\Phi = i\omega_F \phi(r, \theta, z) e^{i\omega_F t}. \quad (4.19)$$

At every instant t , the potential must solve Laplace's equation, i.e.:

$$\frac{\partial^2 \phi}{\partial r^2} + \frac{1}{r} \frac{\partial \phi}{\partial r} + \frac{1}{r^2} \frac{\partial^2 \phi}{\partial \theta^2} + \frac{\partial^2 \phi}{\partial z^2} = 0. \quad (4.20)$$

We then apply the separation of variables $\phi(r, \theta, z) = R(r)P(\theta)Z(z)$ to determine the expression of ϕ_1 and ϕ_2 (see Appendix A). The subscript 1 refers to the upper fluid, while 2 is for the lower. From the separation of variables, we get:

$$\phi(r, \theta, z) = \cos n\theta \sum_{s=1}^{\infty} (A_{nms} J_n(\beta_{nms} r) + B_{nms} Y_n(\beta_{nms} r)) (C_1 \cosh \beta_{nms} z + C_2 \sinh \beta_{nms} z). \quad (4.21)$$

To better reproduce the system from Presas et al. (2015a), we have established three models: the first without a shaft in the fluid (except at the center of the rotor with the same thickness), the second with a shaft in the lower fluid domain and the last with a shaft throughout both fluid domains. Considering a shaft changes the boundary condition on the fluid at the center of the confinement, which influences the radial form of the fluid displacement potential. Especially, the Bessel function of the second kind may or may not be included, depending on the presence of the shaft since the fluid displacement potential has to be finite at $r = 0$ and $\lim_{r \rightarrow 0} Y_n(r) = \infty$. Most of the fluid flows in the radial gap or between adjacent antinodes, hence the three models lead to similar results. Thus, the presence of a shaft at the center has little influence on the fluid flow. We decided to use a model without shaft for the entire analytical approach.

Fluid-structure interaction model

First, we apply to the fluid displacement potentials from Eq. 4.21 the boundary conditions at the lateral wall Γ_c and the center of the confinement Γ_0 of the Figure 4.1b:

$$\begin{cases} \frac{\partial \phi_1}{\partial r} \Big|_{r=c} = 0 \text{ and } \phi_1 \Big|_{r=0} = 0 \\ \frac{\partial \phi_2}{\partial r} \Big|_{r=c} = 0 \text{ and } \phi_2 \Big|_{r=0} = 0 \end{cases} . \quad (4.22)$$

Upon application of the boundary conditions of Eq. (4.22), we are able to remove the Bessel function of the second kind and determine β_{nms} with the first set of conditions, such that $J'_n(\beta_{nms}c) = 0$. We introduce s as the root index for the n -th derivative of the Bessel function, where the root is represented by β_{nms} , which takes a value for each s . According to the superposition principle, every root has to be considered or at least a sufficient number so that convergence has been reached. Thus, we truncate the infinite sum of Eq. (4.21) to N_s terms. The value of N_s , which ensures convergence, is determined at the end of this section.

The boundary conditions at the lower and upper walls Γ_{H_1} and Γ_{H_2} (see Figure 4.1b) give us the following equations on the fluid displacement potentials:

$$\begin{cases} \frac{\partial \phi_1}{\partial z} \Big|_{z=H_1} = 0 \\ \frac{\partial \phi_2}{\partial z} \Big|_{z=-H_2} = 0 \end{cases} , \quad (4.23)$$

which allow us to determine the unknown terms in the axial component of the fluid displacement potentials from Eq. (4.21). Substituting Eq. (4.21) into the boundary conditions of Eq. (4.23) leads to:

$$\begin{cases} \phi_1(r, \theta, z) = \cos n\theta \sum_{s=1}^{\infty} A_{nms} J_n(\beta_{nms}r) [\cosh \beta_{nms}z - \tanh \beta_{nms}H_1 \sinh \beta_{nms}z] \\ \phi_2(r, \theta, z) = \cos n\theta \sum_{s=1}^{\infty} C_{nms} J_n(\beta_{nms}r) [\cosh \beta_{nms}z + \tanh \beta_{nms}H_2 \sinh \beta_{nms}z] \end{cases} , \quad (4.24)$$

which are the fluid displacement potentials of the upper and lower fluid domains, respectively.

The last coefficients left to evaluate in Eq. (4.21) are A_{nms} and C_{nms} , with the conditions for the fluid-shaft (considered rigid), fluid-rotor and fluid-fluid interfaces Γ_{shaft} , Γ_{rotor} and Γ_{gap} in $z = 0$ (see Figure 4.1b). This is where we determine the influence of the deformable rotor on the surrounding fluid. While the non-slip boundary condition is not considered as the fluid is inviscid, we apply the kinematic (or non-penetration) condition, which ensures that the velocity normal component is continuous, on the potential fluid displacements from

Eq. (4.24):

$$\frac{\partial \phi_{1/2}}{\partial z} \Big|_{z=0} = \begin{cases} 0 & 0 \leq r \leq b \\ \left(1 + \frac{n\Omega_{R/F}}{\omega_F}\right) \psi_n(r) \cos n\theta & b < r \leq a \end{cases} \quad \text{and} \quad \frac{\partial \phi_1}{\partial z} \Big|_{z=0} = \frac{\partial \phi_2}{\partial z} \Big|_{z=0}, \quad a < r \leq c. \quad (4.25)$$

In addition, the dynamic condition ensures that the pressure of an inviscid fluid at an interface is continuous and applying it to Eq. (4.24) for the interface Γ_{gap} leads to:

$$\phi_2|_{z=0} = \phi_1|_{z=0}, \quad a < r \leq c. \quad (4.26)$$

This condition is only applied on the fluid-fluid interface Γ_{gap} , as it is later used in the equation of motions to couple the fluid motions related to each deformation of the rotor and stator, or could have been used instead of the AVMI factor calculus for the lone rotor.

Louyot (2019) used the Galerkin method and Hankel transform to discretize these interfaces, whereas we will use the approach from Askari et al. (2013), the point collocation method. To solve these systems of equations, we define a vector with unknown coefficients $\xi = (\xi_1, \xi_2, \dots, \xi_{N_s})$, such that $\xi = \begin{Bmatrix} A \\ C \end{Bmatrix}$, where A refers to A_{nms} and C to C_{nms} . We substitute the flow potentials of Eq. (4.24) into the boundary conditions of Eq. (4.25) and (4.26). We then apply the point collocation method by enforcing that these boundary conditions are met at N_i evenly distributed points $r_i = (i-1)(c/N_i)$, with $i = (1, \dots, N_i)$. Therefore, we obtain $2N_i$ equations of the form:

$$\sum_{s=1}^{N_s} X_{is} \xi_s = Y_i. \quad (4.27)$$

The left part of Eq. (4.27) is composed of the derivatives of the fluid displacements potentials and their difference such that Y_i is filled with 0 or the term associated to the deformation of the rotor from Eq. (4.25). To reduce the sums in s in a product of a matrix \mathbf{X} and a vector ξ , the latter is a concatenation of each vector ξ_s , namely $\xi = \{A_{nm0}, C_{nm0}, \dots, A_{nmN_s}, C_{nmN_s}\}$. Hence, each matrix or vector has the following size:

$$\mathbf{X} : \{2 \times N_i, 2 \times N_s\}, \quad Y : \{2 \times N_i, 1\} \quad \text{and} \quad \xi : \{2 \times N_s, 1\}. \quad (4.28)$$

To determine the unknown parameters A_{nms} and C_{nms} , we evaluate the pseudo-inverse of \mathbf{X} , non-invertible as it is not always square, such that:

$$\mathbf{X}\xi = Y \leftrightarrow \xi = (\mathbf{X}^T \mathbf{X})^{-1} \mathbf{X}^T Y. \quad (4.29)$$

This calculus is done numerically with the Python code. In it, the pseudo-inverse matrix is evaluated with the singular values decomposition of \mathbf{X} .

Now that A_{nms} and C_{nms} are determined, we have the expressions for the potentials. Hence, we can calculate the AVMI factor β_0 with the fluid and disk reference kinetic energies to then determine the eigenfrequencies of the rotor alone:

$$\beta_0 = \frac{E_f^1 + E_f^2}{E_d}, \quad (4.30)$$

with

$$E_f^i = \rho_F \int \int_{\Omega_i} \phi_i|_{z=0} \frac{\partial \phi_i}{\partial z} \Big|_{z=0} r dr d\theta, \quad (4.31)$$

and

$$E_d = \frac{1}{2} \rho_D h \int \int_{\Omega} w^2 r dr d\theta. \quad (4.32)$$

The subscript 0 refers to the rotation not being included in the model, to simplify it. The natural frequencies in water of the rotor ω_F can be written as a function of those in vacuo ω_V :

$$\frac{\omega_F}{\omega_V} = \frac{1}{\sqrt{1 + \beta}} \quad (4.33)$$

with $\beta = (1 + n\Omega_R/\omega_F)^2 \beta_0$ according to Louyot (2019). By inserting the expression of β in Eq. (4.33), we obtain as Louyot (2019):

$$\omega_F = \frac{\sqrt{(\beta_0 + 1)\omega_V^2 - \beta_0(n\Omega_{R/F})^2 - n\beta_0\Omega_{R/F}}}{\beta_0 + 1}. \quad (4.34)$$

We are able to implement the rotation at the last step (and express β as a function of β_0 as Louyot (2019)), and use numerical calculation instead of symbolic (as integrating the rotation earlier introduces the unknown ω_F), because we can isolate ω_F at each of its appearances. Indeed, it intervenes during two steps of the approach: while applying the boundary conditions for the interfaces Γ_{shaft} , Γ_{rotor} and Γ_{gap} , and for the evaluation of the kinetic energies, through the term $\frac{\partial \phi_i}{\partial z} \Big|_{z=0}$ and its expression in Eq. (4.25). In the first one, we only have terms that are null or of deformation in the vector Y , as explained above. For the second one, we get ω_F out of the integrals, as it does not contain variables of integration.

Annular disk coupled through fluid with flexible disk

To consider the coupling of the stator with the rotor, the latter is not considered rigid anymore but flexible, as can be seen in Figure 4.2.

Fluid displacement potentials

First, we use the principle of superposition and consider the potential flow solution ϕ^R resulting from rotor deformation for a fixed stator and the potential ϕ^S resulting from stator deformation for a fixed rotor (see Figure 4.3).

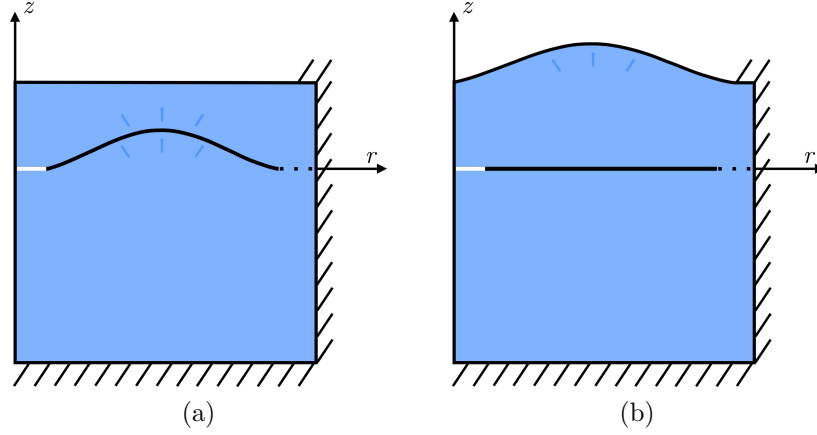


Figure 4.3 (a) Rotor-only deformation; and (b) stator-only deformation

The flow potentials above and below the rotor (see Figure 4.2) can be expressed as:

$$\begin{cases} \phi_1 = \phi_1^S + \phi_1^R \\ \phi_2 = \phi_2^S + \phi_2^R \end{cases} . \quad (4.35)$$

After applying the separation of variables to Laplace's equation and the boundary conditions at the interfaces with the lower and upper walls Γ_{H_1} and Γ_{H_2} , as well as with the confinement lateral wall Γ_c and its center Γ_0 (see Figure 4.1b), we obtain the fluid displacement potentials:

$$\begin{cases} \phi_1^R(r, \theta, z) = \cos n\theta \sum_{s=1}^{\infty} A_{nms} J_n(\beta_{nms} r) [\cosh \beta_{nms} z - \tanh \beta_{nms} H_1 \sinh \beta_{nms} z] \\ \phi_2^R(r, \theta, z) = \cos n\theta \sum_{s=1}^{\infty} B_{nms} J_n(\beta_{nms} r) [\cosh \beta_{nms} z + \tanh \beta_{nms} H_2 \sinh \beta_{nms} z] \end{cases} \quad (4.36)$$

and

$$\begin{cases} \phi_1^S(r, \theta, z) = \cos n\theta \sum_{s=1}^{\infty} J_n(\beta_{nms} r) [A_{nms}^- \cosh \beta_{nms} z + B_{nms}^- \sinh \beta_{nms} z] \\ \phi_2^S(r, \theta, z) = \cos n\theta \sum_{s=1}^{\infty} C_{nms}^- J_n(\beta_{nms} r) [\cosh \beta_{nms} z + \tanh \beta_{nms} H_2 \sinh \beta_{nms} z] \end{cases} . \quad (4.37)$$

The potential ϕ_1^S in Eq. (4.36) has a different form than the others because, as the stator deforms, the boundary condition on the upper wall from Eq. (4.23) cannot be applied.

Moreover, the coefficient normally found in the radial component has been included in A_{nms}^- and B_{nms}^- , to reduce the number of unknowns.

We then apply the kinematic and dynamic conditions associated to the fluid-shaft, fluid-fluid, fluid-rotor and fluid-stator interfaces Γ_{shaft} , Γ_{gap} , Γ_{rotor} and Γ_{stator} to the fluid displacement potentials from Eq. (4.36) and (4.37), to determine A_{nms} , B_{nms} , A_{nms}^- , B_{nms}^- and C_{nms}^- . We use the point collocation method as described in the precedent section. For the sole deformation of the rotor, we employ the same equations as before, given in Eq. (4.25) and (4.26), and thus the same results for A_{nms} and B_{nms} (the latter replaced C_{nms}). For the sole deformation of the stator, we have:

$$\left. \frac{\partial \phi_1^S}{\partial z} \right|_{z=0} = \begin{cases} 0 & 0 \leq r \leq a \\ \frac{\partial \phi_2^S}{\partial z} \Big|_{z=0} & a < r \leq c \end{cases} \quad \text{and} \quad \begin{cases} \frac{\partial \phi_2^S}{\partial z} \Big|_{z=0} = 0 & b \leq r \leq a \\ \phi_2^S \Big|_{z=0} = \phi_1^S \Big|_{z=0} & a < r \leq c \end{cases}, \quad (4.38)$$

as well as

$$\begin{cases} \frac{\partial \phi_1^S}{\partial z} \Big|_{z=H_1} = \left(1 + \frac{n\Omega_{S/F}}{\omega_F}\right) \psi_{nm}^S(r) \cos n\theta & 0 \leq r \leq d \\ \frac{\partial \phi_1^S}{\partial z} \Big|_{z=H_1} = 0 & d < r \leq c \end{cases} \quad (4.39)$$

with $\Omega_{S/F} = K\Omega_R$ the relative speed of the stator compared to the fluid (as the fluid rotates) and:

$$\psi_{nm}^S(r) = J_n(k_{nm}^S r) - \frac{J_n(k_{nm}^S d)}{Y_n(k_{nm}^S d)} Y_n(k_{nm}^S r). \quad (4.40)$$

The modeshapes ψ_{nm}^S of the stator have been determined by solving the eigenvalue problem resulting from the application of the boundary conditions of a free-fixed circular disk.

Eigenfrequencies calculation

Each fluid displacement potential for each deformation is calculated in an uncoupled way, but it is necessary to then couple them to determine the dynamic behavior of the system. As the amplitudes for the stator and rotor are not known, we introduce an unknown amplitude term for their displacement (respectively A_{nm}^R and A_{nm}^S), which allows us to couple them:

$$\begin{cases} w^R(r, \theta, t) = A_{nm}^R \cos(n\theta) \psi_{nm}^R(r) e^{i\omega_F t} \\ w^S(r, \theta, t) = A_{nm}^S \cos(n\theta) \psi_{nm}^S(r) e^{i\omega_F t} \end{cases}. \quad (4.41)$$

We first evaluate the natural frequencies, to validate our model with the results of Weder et al. (2019). We have used three formulae employed in the literature: the equations of motion, the AVMI factor and the Rayleigh coefficient. The first ones introduce the fluid influence through

the pressure of the dynamic condition at the interfaces Γ_{rotor} and Γ_{stator} (see Figure 4.1b), while for the other two, it is through the reference kinetic energies. Moreover, the second one uses the natural frequencies of the disks in vacuo, while the last one does not. Using these three different methods allowed us to compare them, and reach the correct formulation of the rotor-stator coupling. Below, we describe the first approach, while the other two can be found in Appendix C.

We write Euler's equation which links the fluid velocity V to the pressure p to calculate the ones on the rotor and stator:

$$\rho_F \frac{\partial \vec{V}}{\partial t} + \rho_F (\vec{V} \cdot \nabla) \vec{V} = -\nabla p. \quad (4.42)$$

We introduce the velocity potential Φ such that $\vec{V} = \nabla \Phi$ and we obtain:

$$\rho_F \frac{\partial \Phi}{\partial t} + \rho_F \frac{1}{2} (\nabla \Phi)^2 + p = 0. \quad (4.43)$$

While the first term of Eq. (4.43) is proportional to the acceleration (i.e. the added mass) due to its derivation in time, the central term is proportional to velocity. According to D'Alembert's paradox, the flow of an ideal fluid (irrotational, incompressible and inviscid such as ours) exerts zero net force on a body submerged in it. Therefore, when the pressure is integrated to be implemented as a force in the equations of motions, this term is null. Thus we consider it as null from this step on to simplify the calculations, and by replacing Φ with $i\omega_F e^{i\omega_F t} \phi$ in Eq. (4.43):

$$p = \rho_F \omega_F^2 \phi e^{i\omega_F t} \text{ with } \phi = \phi_1^R + \phi_2^R + \phi_1^S + \phi_2^S. \quad (4.44)$$

As the rotor is placed at $z = 0$ and the stator at $z = H_1$, the pressures exerted on both are obtained from Eq. (4.44):

$$\begin{cases} p^R = \rho_F \omega_F^2 \left[A_{nm}^R \left(1 + \frac{n\Omega_{R/F}}{\omega_F} \right) (\phi_1^R|_{z=0} + \phi_2^R|_{z=0}) \right. \\ \quad \left. + A_{nm}^S \left(1 + \frac{n\Omega_{S/F}}{\omega_F} \right) (\phi_1^S|_{z=H_1} + \phi_2^S|_{z=H_1}) \right] e^{i\omega_F t} \\ p^S = \rho_F \omega_F^2 \left[A_{nm}^R \left(1 + \frac{n\Omega_{R/F}}{\omega_F} \right) \phi_1^R|_{z=0} + A_{nm}^S \left(1 + \frac{n\Omega_{S/F}}{\omega_F} \right) \phi_1^S|_{z=0} \right] e^{i\omega_F t} \end{cases}, \quad (4.45)$$

where the unknowns such as the amplitude terms and the natural frequencies are taken out of the fluid displacement potentials.

We express the equations of motion for the rotor and stator with Eq. (4.1), then we apply the Galerkin method as in the structural model, to use the modes' orthogonality to nullify

all the incompatible modes, which gives:

$$\begin{cases} -M^R \omega_F^2 e^{i\omega_F t} A_{nm}^R + K_{nm}^R e^{i\omega_F t} A_{nm}^R = \int_b^a \int_0^{2\pi} p^R \omega^R r dr d\theta \\ -M^S \omega_F^2 e^{i\omega_F t} A_{nm}^S + K_{nm}^S e^{i\omega_F t} A_{nm}^S = \int_0^d \int_0^{2\pi} p^S \omega^S r dr d\theta \end{cases}, \quad (4.46)$$

where

$$\begin{cases} M^R = \rho_r \int_b^a \int_0^{2\pi} \psi_{nm}^R{}^2 r dr d\theta \text{ and } K_{nm}^R = D^R k_{nm}^4 \int_b^a \int_0^{2\pi} \psi_{nm}^R{}^2 r dr d\theta \\ M^S = \rho_s \int_0^d \int_0^{2\pi} \psi_{nm}^S{}^2 r dr d\theta \text{ and } K_{nm}^S = D^S k_{nm}^4 \int_0^d \int_0^{2\pi} \psi_{nm}^S{}^2 r dr d\theta \end{cases}. \quad (4.47)$$

By applying the modes' orthogonality, we should have $\int_{b/0}^{a/d} \int_0^{2\pi} \psi_{im}^{R/S} \psi_{jm}^{R/S} r dr d\theta = 2\pi(a^2 - b^2)\delta_{ij}$ or $2\pi d^2\delta_{ij}$. Yet, by considering these expressions, the model does not work, so we have kept the initial form. We then transform the system of Eq. (4.46) in a matrix form by isolating the amplitude terms A_{nm}^R and A_{nm}^S to solve it:

$$\begin{bmatrix} M^R \omega_F^2 - K_{nm}^R + p_R^R & p_S^R \\ p_R^S & M^S \omega_F^2 - K_{nm}^S + p_S^S \end{bmatrix} \cdot \begin{bmatrix} A_{nm}^R \\ A_{nm}^S \end{bmatrix} = \vec{0}, \quad (4.48)$$

with

$$\begin{cases} p_R^R = \rho_F \omega_F^2 \left(1 + \frac{n\Omega_{R/F}}{\omega_F}\right)^2 \int_b^a \int_0^{2\pi} (\phi_1^R|_{z=0} + \phi_2^R|_{z=0}) \psi_{nm}^R(r) \cos(n\theta) r dr d\theta \\ p_S^R = \rho_F \omega_F^2 \left(1 + \frac{n\Omega_{S/F}}{\omega_F}\right) \left(1 + \frac{n\Omega_{R/F}}{\omega_F}\right) \int_b^a \int_0^{2\pi} (\phi_1^S|_{z=0} + \phi_2^S|_{z=0}) \psi_{nm}^R(r) \cos(n\theta) r dr d\theta \\ p_R^S = \rho_F \omega_F^2 \left(1 + \frac{n\Omega_{R/F}}{\omega_F}\right) \left(1 + \frac{n\Omega_{D/F}}{\omega_F}\right) \int_0^d \int_0^{2\pi} \phi_1^R|_{z=0} \psi_{nm}^S(r) \cos(n\theta) r dr d\theta \\ p_S^S = \rho_F \omega_F^2 \left(1 + \frac{n\Omega_{S/F}}{\omega_F}\right)^2 \int_0^d \int_0^{2\pi} \phi_1^S|_{z=0} \psi_{nm}^S(r) \cos(n\theta) r dr d\theta \end{cases}. \quad (4.49)$$

We can get out the rotation terms containing ω_F from the pressures of Eq. (4.49) in the system of Eq. (4.48):

$$\begin{bmatrix} \omega_F^2 \begin{bmatrix} M^R + \hat{p}_R^R & \hat{p}_S^R \\ \hat{p}_R^S & M^S + \hat{p}_S^S \end{bmatrix} + \omega_F n \Omega_D \begin{bmatrix} 2(1-K)\hat{p}_R^R & \hat{p}_S^R \\ \hat{p}_R^S & 2K\hat{p}_S^S \end{bmatrix} \\ - \begin{bmatrix} K_{nm}^R + n^2(1-K)^2\Omega_D^2\hat{p}_R^R & n^2K(1-K)\Omega_D^2\hat{p}_S^R \\ n^2K(1-K)\Omega_D^2\hat{p}_R^S & K_{nm}^S + n^2K^2\Omega_D^2\hat{p}_S^S \end{bmatrix} \end{bmatrix} \cdot \begin{bmatrix} A_{nm}^R \\ A_{nm}^S \end{bmatrix} = \vec{0}, \quad (4.50)$$

where:

$$\begin{cases} \hat{p}_R^R = \rho_F \int_b^a \int_0^{2\pi} (\phi_1^R|_{z=0} + \phi_2^R|_{z=0}) \psi_{nm}^R(r) \cos(n\theta) r dr d\theta \\ \hat{p}_S^R = \rho_F \int_b^a \int_0^{2\pi} (\phi_1^S|_{z=0} + \phi_2^S|_{z=0}) \psi_{nm}^R(r) \cos(n\theta) r dr d\theta \\ \hat{p}_R^S = \rho_F \int_0^d \int_0^{2\pi} \phi_1^R|_{z=0} \psi_{nm}^S(r) \cos(n\theta) r dr d\theta \\ \hat{p}_S^S = \rho_F \int_0^d \int_0^{2\pi} \phi_1^S|_{z=0} \psi_{nm}^S(r) \cos(n\theta) r dr d\theta \end{cases} \quad (4.51)$$

By identifying the matrices in Eq. (4.50), we obtain the equations of a one degree-of-freedom damped mass-spring oscillator:

$$[M\omega_F^2 + C\omega_F + K] \cdot \begin{bmatrix} A_{nm}^R \\ A_{nm}^S \end{bmatrix} = \vec{0}. \quad (4.52)$$

From Eq. (4.50) and (4.52), we get a better physical understanding of the rotor-stator coupling. Indeed, without rotation, we observe that, in addition to the added mass induced when the rotor and the stator deform separately, their deformations also create an added mass for each other, which represents their coupling. The modal rigidity is not affected in this case. Rotation does not affect the modal mass, but the modal rigidity is affected in this case, in addition to the appearance of damping. The observations made for the modal mass in the case without rotation are valid for the modal rigidity when rotation is implied.

To determine the natural frequencies, we solve numerically the determinant of the matrix from Eq. 4.52, where ω_F is the unknown. It is equivalent to solving an eigenvalue problem. By then substituting the values of the eigenfrequencies in Eq. (4.52), we obtain the eigenmodes of the problem, and we deduce the associated amplitude ratio. It is negative for a varicose mode and positive for a sinuous one, as the modeshapes are out-of-phase for the first one and in-phase for the second.

Convergence analysis

To choose the parameters N_s and N_i , we have to analyze their influence on the convergence of the model. To do so, we study the evolution of the natural frequencies depending on the pair selected, as well as the condition number of the pseudo-inverse matrix from Eq. (4.27) for the point collocation method. We use the condition number to determine if the matrix is ill-conditioned, and if it is correlated to the trend of the results. For the initial system of Presas et al. (2015a), with the parameters defined after in Table 6.2, we obtain Figure 4.4.

Figure 4.4 contains two 2D subfigures with N_s and N_i as abscissae. Figure 4.4a represents the eigenfrequencies of the rotor in the rotating reference frame for two nodal diameters and no nodal circles. In Figure 4.4b, the evolution of the condition number of the pseudo-

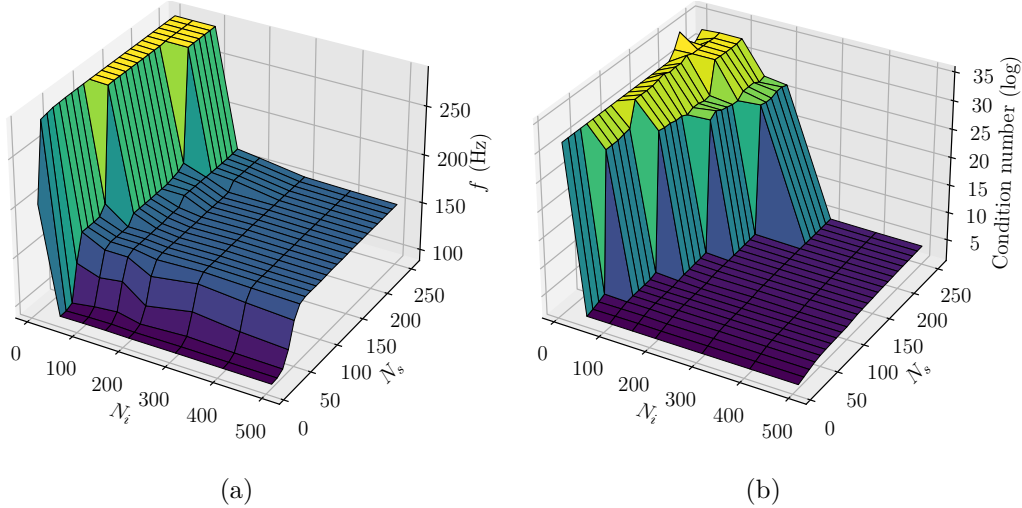


Figure 4.4 N_i and N_s influence on (a) the natural frequencies of the rotor; and (b) the condition number of the pseudo-inverse matrix from the point collocation method

inverse matrix is displayed. As we can see, there is a direct correlation between the condition number of the pseudo-inverse matrix and the eigenfrequencies: when the condition number is significant, the results are more likely to diverge. Moreover, if the pair of parameters is not compatible, the condition number soars, as well as the results. We observe that we have to choose a large enough value for both parameters. However, N_s and N_i greatly influence the computing time of the code as they determine the number of terms present in the different matrices. Therefore, we select their values such that the convergence has just been attained:

$$N_i = 200 \text{ and } N_s = 80.$$

We tested the influence of N_s and N_i for different configurations of the model from Presas et al. (2015a), and we observed similar convergence, such that the values chosen were still valid. We also looked at the system from Weder et al. (2019), for the parameters defined after in Table 6.8. The convergence of the natural frequencies of the in-phase modes is reached even faster, even if we lack information on the condition number, as it can be calculated solely for the rotor or stator and not for the coupling. Hence, the values selected for N_i and N_s are still valid. We could also have changed them to reduce computation time but it is not realistic to check convergence for each system and change their values accordingly.

CHAPTER 5 METHODOLOGY - FEM MODEL

The FEM model was used to support the analytical approach, by comparing their results for the same assumptions, and create an effective and fast tool to characterize the dynamic behavior of lone submerged rotors or coupled with stators through fluid. We started its development by investigating the dynamic behavior of a stationary annular disk in vacuo using hexahedral finite elements with Ansys Mechanical under Ansys Workbench. We then added the fluid cavity, first filled with air, then with water simulated as acoustic elements to reproduce the model of Presas et al. (2015a). The casing was additionally integrated to have boundary conditions similar to those of Presas et al. (2015a) and get results closer to their experimental data. The integration of the fluid rotation through the use of APDL commands was investigated. From here on, the further development of the FEM model was done by Blais (2021) during his internship, where we helped for the conceptualization of the methodology and acted as supervisors. Blais (2021) implemented the rotation of the fluid in the simulation, as well as the boundary conditions used in the analytical approach and in the study of Presas et al. (2015a). He then added the stator to represent its coupling with the rotor through the reproduction of the models from Jeong (2003, 2006) to finish with the experimental setup of Weder et al. (2019). He additionally removed the necessity to use Ansys Mechanical under Ansys Workbench by combining it with a Python code through APDL commands. This allowed a fast and simple setup of the analysis, as well as the possibility to do automatic parametric studies. In the following, we briefly describe the derived model, and additional details can be found in Blais (2021).

We performed an acoustic-structural modal analysis in Ansys Mechanical APDL 2021R1. The fluid, by being simulated with acoustic elements, is considered inviscid, irrotational, and either compressible or incompressible. The mesh is chosen to be structural hexahedral to be able to ensure a good aspect ratio with the number of divisions along the radial, tangential and axial directions. The elements are quadratic and an example of mesh is given in Figure 5.1. The latter shows that there is no need to include a casing, as Ansys interprets the outer surfaces of the fluid as rigid walls (we save on the number of elements). The nodes present in the fluid-structure interface belong simultaneously to both structural and acoustic elements. While the structural elements possess displacement Degrees Of Freedom (DOF), the acoustic elements have pressure DOF.

To characterize the mode split numerically, the rotation of the rotor has to be included. As the fluid is inviscid, it cannot be entrained if the structure rotates, therefore the fluid

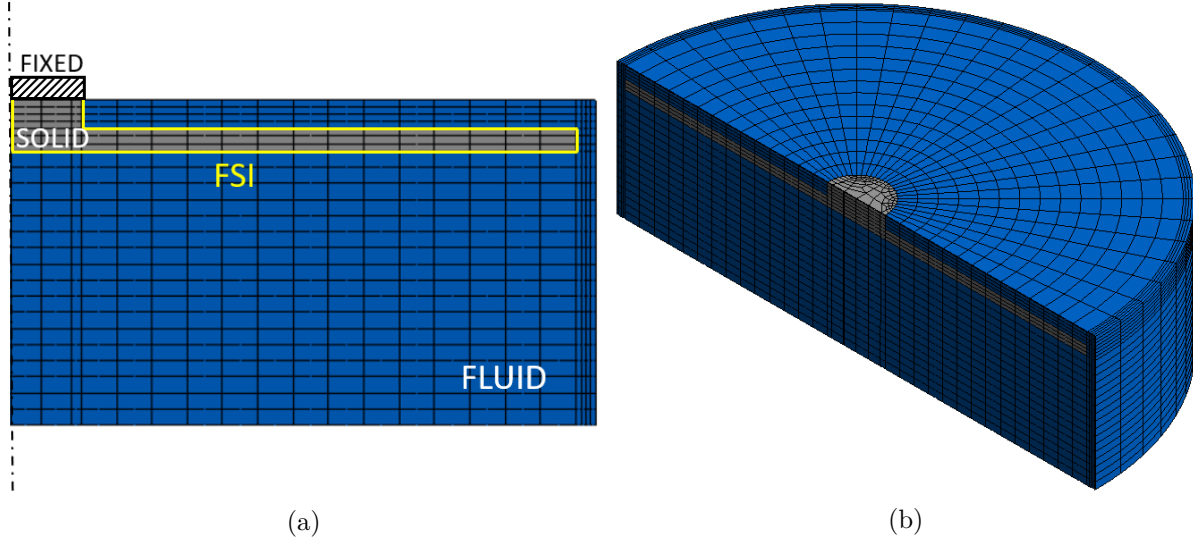


Figure 5.1 Basic mesh with quadratic elements from Blais (2021): a) section view with boundary conditions; and b) isometric section view

rotates as a solid body, while the rotor is stationary. We use the same method as in the analytical model, namely we evaluate the relative velocity of the fluid to the rotor with the empirical entrainment factor K (from Poncet et al. (2007)). We get the relative rotational velocity of the fluid with respect to the rotor $\Omega_{F/R} = \Omega_F - \Omega_R$ where $\Omega_F = K\Omega_R$, which we apply through the mean flow effect (only supported by Ansys 2021R1) on the fluid nodes. This command allows us to enforce a constant (or varying in space as in our model) velocity $\vec{V}_\theta = \Omega_{F/R} r \vec{e}_\theta$ on each node.

To compare results with the analytical approach, and also to validate its development, the FEM model was used to reproduce the work from Presas et al. (2015a), Jeong (2003, 2006) and Weder (2018).

To allow for automatic pre and post-processing, as well as effective parametric studies, Ansys Mechanical APDL 2021R1 was coupled with Python 3.8. Indeed, the latter is in charge of those two steps, by defining the input parameters and the chosen configuration, as well as managing the results from Ansys to identify the modeshapes associated with each frequency and to plot the relevant graphs (e.g. modeshapes visual representation). A global workflow is given in Figure 5.2.

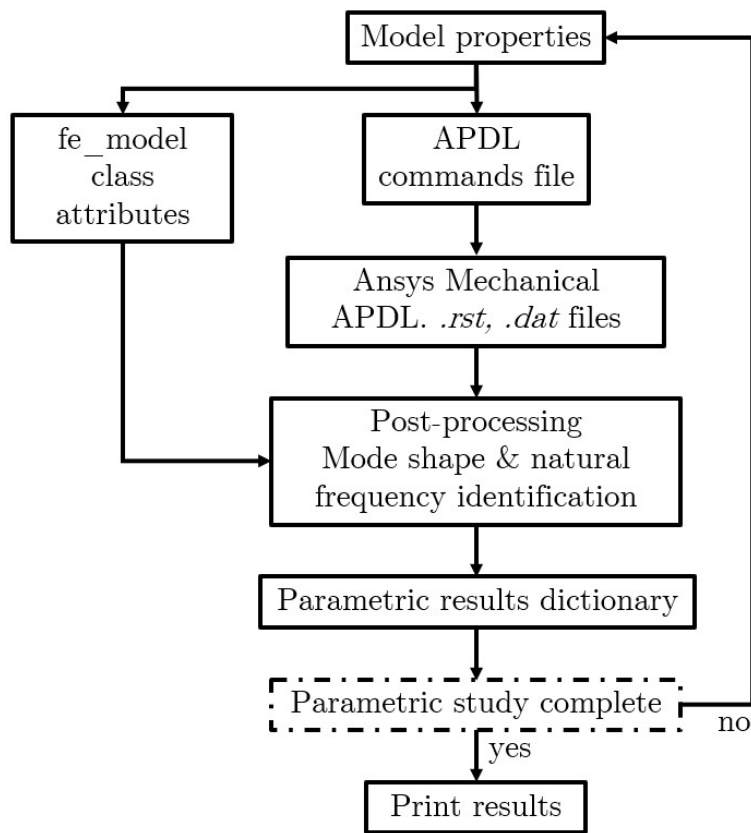


Figure 5.2 FEM workflow followed by Blais (2021)

CHAPTER 6 RESULTS AND DISCUSSION

In this section, we address the results of the two developed analytical models for the submerged rotating rotor with radial gap, and for the coupling of the rotor and stator. To verify the second approach, we first represent the systems from Jeong (2003, 2006) and compare our results with their analytical data. Once both models are validated, we compare them with their FEM counterpart, and get a better understanding of the involved phenomena through parametric studies. Table 6.1 is a summary of the four developed models, used as reference along this section.

Table 6.1 Summary of all the developed models

Name	Description	Schematic
Confined rotor	Fixed-free annular disk in fluid-filled and rigid confinement	
Coupled static disks	Identical free-fixed circular disks coupled with fluid	
Coupled static annuli	Fixed-fixed annular disks coupled with fluid	
Coupled rotor-stator	Free-fixed circular disk and fixed-free annular disk coupled by fluid in rigid confinement	

Submerged annular disk in rigid confinement

Here we present and discuss the results of the analytical model for the confined rotor, as depicted in Table 6.1. We first validate the model with experimental data from Presas et al. (2015a), then compare it with the FEM model. Finally, we analyze the fluid flow and the

influence of multiple parameters on the vibration of the rotor, such as the rotation of the disk, the axial and radial gaps, the disk thickness, as well as the disk inner and outer radii.

Validation of the analytical model

To validate the model, we use experimental data from Presas et al. (2015a) for the system depicted in Table 2.1. Even if a shaft is present in their system, it has been shown in the methodology that it does not influence the dynamic behavior of the disk. As some parameters were not defined, in particular for the material, we chose the same ones as Louyot (2019), listed in Table 6.2.

Table 6.2 Model properties for the validation with experimental data from Presas et al. (2015a)

Parameter	Value
E [GPa]	200
ρ_D [kg/m ³]	7680
ν	0.27
ρ_F [kg/m ³]	997
b [mm]	25
a [mm]	200
c [mm]	207
h [mm]	8

In Table 6.3, we compare the natural frequencies $f = \omega/(2\pi)$ (in Hz) of our analytical model with the experimental ones from Presas et al. (2015a) for the modes with $n = 2, 3, 4$ nodal diameters (with $m = 0$ nodal circles). Presas et al. (2015a) chose these modes as they are the most likely to be excited in high-head turbines. In this chapter, all natural frequencies are expressed in Hz and in the rotating reference frame.

Table 6.3 Comparison with experimental natural frequencies from Presas et al. (2015a)

Mode	$f_{F,exp,Presas}$ [Hz]	$f_{F,ana}$ [Hz]	$\varepsilon_{exp,ana}$
(2,0)	127.05	149.39	17.58%
(3,0)	321.16	364.82	13.59%
(4,0)	642.23	696.49	8.45%

The discrepancies between between both sets of results are significant, and decrease with the number of nodal diameters. Several differences between both models can explain such discrepancies. First of all, as written before, not all parameters are given by Presas et al. (2015a), in particular for the material properties, which have a considerable influence on the

dynamic behavior of the disk. We modified them and obtained better accuracy, but it does not represent a real validation as we cannot know the initial parameters of the experimental setup. Moreover, the boundary conditions are different and difficult to reproduce analytically. Indeed, there is no information on the casing, but it seems to be thin and thus flexible. It is then likely to affect the vibrations of the rotor by being coupled through the fluid. The casing was considered flexible by Blais (2021) in his FEM model, and he got more accurate results, showing that this particular boundary condition has an effect on the natural frequencies. We also reproduced differently the model of Presas et al. (2015a) by considering the top surface of the casing as a flexible fixed-fixed annular disk (see Appendix D). The natural frequencies are slightly lowered by the addition of a non-rigid stator, so it seems that the material properties have the highest contribution in the discrepancies between the analytical results and the experimental data from Presas et al. (2015a).

Table 6.4 Comparison of the ratio of the natural frequencies in fluid with those in vacuo from the analytical model and from Presas et al. (2015a)

Mode	$\frac{f_{F,exp,Presas}}{f_{V,exp,Presas}} [Hz]$	$\frac{f_{F,ana}}{\omega_{V,ana}} [Hz]$	$\varepsilon_{exp,ana}$
(2,0)	0.492	0.523	6.20%
(3,0)	0.545	0.592	8.58%
(4,0)	0.622	0.646	3.91%

To put aside the influence of different structural properties and boundary conditions as best as we can, we evaluate the eigenfrequencies of the three modes in fluid, normalized with those in vacuo. The results are presented in Table 6.4. The values of the ratio increase with the azimuthal wave number, as the added mass effect is less considerable for higher numbers of nodal diameters. Indeed, modes with fewer nodal diameters accelerate the fluid more as it must move between upward and downward antinodes further apart. This in turn increases the added mass of the fluid when near rigid walls. We also observe better accuracy (not linked with the number of nodal diameters), which means that the analytical FSI is close to the experimental one. The fluid is well simulated.

When the disk starts to rotate, the standing wave splits into two traveling waves with their own natural frequencies. Presas et al. (2015a) analyzed the influence of the rotation on this phenomenon, and to compare their experimental data with our results, we also introduced the rotation in our model. The fluid is chosen to rotate as a solid body to a fraction of the angular velocity of the disk, namely the entrainment coefficient K . Its value is dependent on the parameters of the fluid cavity as well as the rotational velocity. Presas et al. (2015a) computed the value of K with CFD to be around 0.4 for their configuration, which matches the range mentioned by Poncet et al. (2005, 2007). We used that value of $K = 0.4$. As

written before, we have considerable discrepancies with the model of Presas et al. (2015a) in terms of frequencies in vacuo, so we evaluated the mode split magnitude from $f_{F,-n} - f_{F,+n}$, i.e. the difference in frequency between the forward and backward travelling waves.

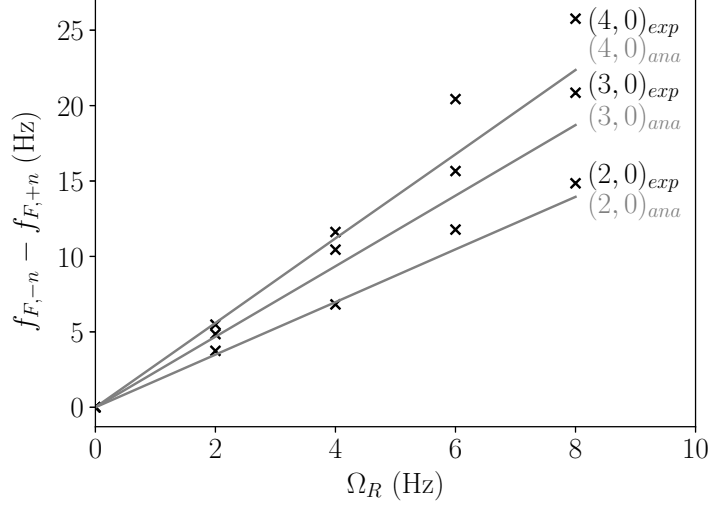


Figure 6.1 Comparison of the analytical prediction (in continuous lines) with experimental data from Presas et al. (2015a) (in dot lines) for the effect of the disk rotational velocity Ω_R on the mode split magnitude $f_{F,-n} - f_{F,+n}$ for the three modes $n = 2, 3, 4$

Figure 6.1 compares analytical results with experimental data from Presas et al. (2015a) for the influence of the disk rotational velocity Ω_R on the mode split magnitude $f_{F,-n} - f_{F,+n}$, for the modes (2,0), (3,0) and (4,0). The mode split magnitude increases with the number of nodal diameters, as well as with the angular velocity for the three modes. The results are precise until the disk rotates at $\Omega_R = 6$ Hz, at which they diverge. In addition to the differences between the two models mentioned before, it may be due to the value of K that does not represent the physics implied anymore. Indeed, Presas et al. (2015a) demonstrated that for higher rotational velocities, the value of K decreases, increasing in turn the mode split magnitude. While it increases nearly linearly for the mode (3,0), the experimental mode split magnitude suddenly increases from $\Omega_R = 6$ Hz.

Comparison between the analytical and FEM models

In addition to the validation with the experimental data from Presas et al. (2015a), we compare it with the FEM model so that this step acts as a verification. The same parameters (see Table 6.2) and assumptions have been considered, such that the confinement is rigid and the fluid is set to incompressible in Ansys, except for the rotation. The comparison is explained by Blais (2021), thus we will briefly discuss them and display the most relevant

results. Some of them are also presented in the next section, so the related observations will be discussed after.

Table 6.5 Natural frequencies in vacuo for FEM and analytical models

Mode	$f_V [Hz]$		
	FEM	Analytical	ε
(2,0)	282.43	285.65	1.14%
(3,0)	611.60	616.22	0.76%
(4,0)	1066.40	1077.64	1.05%

In Table 6.5, we compare the analytical and FEM eigenfrequencies in vacuo to see if the structural part of each model displays the same results. The FEM natural frequencies are slightly lower than the analytical ones. The maximum discrepancy is 1.14%, showing that the structure is simulated similarly by both methods. The small deviations may be explained with the differences inherent to each model, as the disk analytically only deforms in the transverse direction while its three degrees of freedom are considered in the FEM model. Moreover, boundary conditions are not exactly the same as the entire shaft is considered rigid in the analytical model and only its upper and lower surfaces are fixed for the FEM model. Indeed, with the first boundary conditions, the overall rigidity of the disk is higher, which explains the difference between both sets of eigenfrequencies.

Once we had studied the structural part of the analytical and FEM models, we analyzed the influence of the radial and axial gaps, as well as the angular velocity on the dynamic behavior of the rotor. For the first two, Blais (2021) showed that both models display the same behavior: increasing the axial gap or the radial gap increases the natural frequencies; and a good correlation, even if the added mass effect seems to be higher for the FEM model. Indeed, its normalized natural frequencies are slightly lower, which can be explained with the assumptions mentioned before. As for the rotation, except for the natural frequencies themselves (that show the same deviation as before), the mode split magnitude and the frequency drift are close for both models, which shows that the effect of the disk rotation on the dynamic behavior is represented similarly by both methods.

Influence of parameters on implied physics

Here we analyze the influence of different parameters, such as the angular velocity, the radial and axial gaps, the disk thickness and its inner and outer radii, on the dynamic behavior of the rotor. This step is done to verify that we obtain the same physical phenomena observed experimentally by Valentín et al. (2014) and Presas et al. (2015a, 2016), as well as provide

additional understanding about unexplored physics, through new parametric studies. Apart from the parameter whose influence is analyzed, the other values are provided in Table 6.2. The modes studied are the same as the ones of Presas et al. (2015a), namely $(2, 0)$, $(3, 0)$ and $(4, 0)$.

Fluid flow without rotation

To better understand the fluid flow in the confinement, we trace its streamlines with the evaluation of the fluid velocity and its associated displacement potentials. Figure 6.2 depicts the flow streamlines of the confined rotor without rotation for the mode $(2, 0)$ in the plane $(r, \theta, 0.005)$, namely in the middle of the axial gap with $z = 0.005$ m, as well as in the plane $(r, 0, z)$.

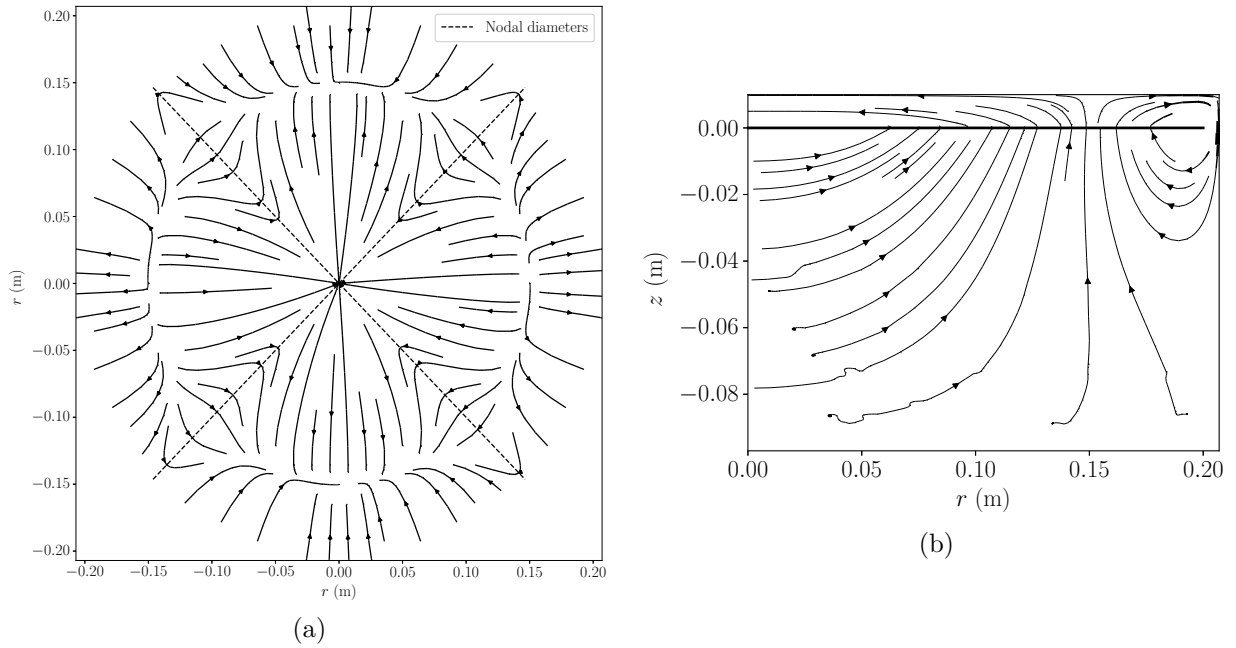


Figure 6.2 Streamlines of the fluid velocity for the mode $(2, 0)$ of the confined rotor without rotation (a) in the plane $(r, \theta, 0.005)$ (where dash lines represent diameters with zero disk displacement, i.e. nodal diameters); and (b) in the plane $(r, 0, z)$

We can get some valuable information solely from the standing case. In Figure 6.2a, the nodal diameters are highlighted by dash lines, so we can observe where are the antinodes (an antinode is the location where the disk observes maximum amplitude), while the flow direction gives their direction. Indeed, we see a circle at $r \approx 0.14$ m where the fluid separates away from the circle and towards the center and edge of the disk in the left and right quarters. In the top and bottom quarters, the flow is reversed and goes toward the $r \approx 0.14$ m circle.

In the first case, it means the antinode is upward, while it is downward in the second. Similar dynamics can be observed for modes with different numbers of nodal diameters (not shown). For an upward antinode, the fluid is pushed towards the adjacent downward antinodes or in the radial gap. For a downward antinode, it is the opposite, the fluid is drawn from the adjacent upward antinodes and through the radial gap. Both motions for each type of antinode is representative of how the added mass of the fluid either contained in the axial or radial gap affects the dynamic behavior of the fluid. Indeed, the added mass is directly proportional to the kinetic energy of the fluid. Figure 6.2b corroborates the observations made for the flow in the axial gap for Figure 6.2a. Indeed, for this upward antinode, as we are in the plane $(r, 0, z)$, the fluid separates away from the $r \approx 0.14$ circle and towards the center and edge of the disk. We can also observe the flow below the disk, where the fluid is dragged to the circle from the center of the disk and the radial gap.

Influence of rotation

In this section, we analyze the influence of the rotational velocity of the confined rotor on its dynamic behavior. First, we look at the evolution of its natural frequencies with the increase of the angular velocity. Figure 6.3 provides further details on the split of the modes $(2, 0)$, $(3, 0)$ and $(4, 0)$, whose magnitude is given in Figure 6.1. The eigenfrequencies are normalized with those in vacuum f_V to better appreciate the mode split of the three modes. Figure 6.1 shows that the mode split magnitude increases with the velocity, and we observe in Figure 6.3 that the frequency of the co-rotating wave is decreasing while it is increasing for the counter-rotating wave. This is the case because the reference frame is rotational, as it is linked to the fluid. It would have been the opposite in the stationary reference frame. Moreover, even if it is barely visible, one can appreciate the frequency drift with the dash lines: the decrease of the central value of the eigenfrequencies of both waves. It becomes considerable for bigger rotational velocities, as demonstrated by Louyot (2019).

Influence of the radial and axial gaps

The proximity to rigid walls of the submerged disk affects its dynamic behavior, as demonstrated by Valentín et al. (2014) and Presas et al. (2016). Therefore, we analyze the effect of the axial and radial gaps H_1 and $c - a$ on the natural frequencies of the confined rotor without rotation for the modes $n = 2, 3, 4$. For the influence of the radial gap, at first, the natural frequencies dropped to a value close to the one for no radial gap, for $c - a < 6$ mm. We then noticed that for such values, the fluid did not flow in the radial gap. For the smallest radial gaps, we discovered that no points of the point collocation method were in the

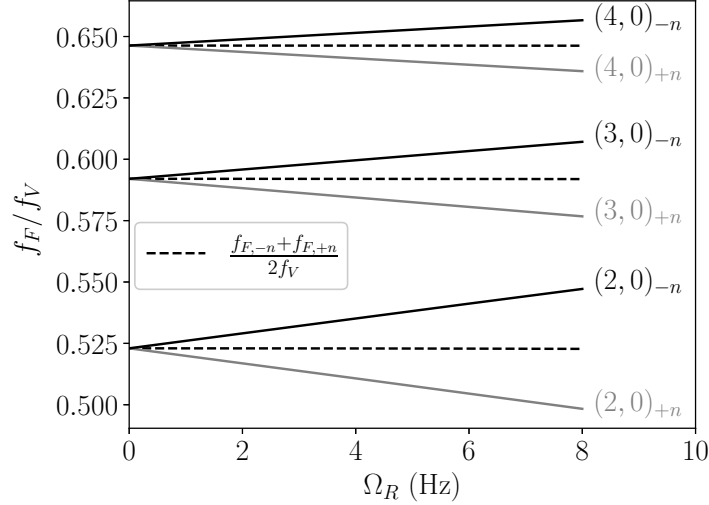


Figure 6.3 Natural frequencies of the co and counter-rotating waves of the confined rotor for the three modes $n = 2, 3, 4$ as a function of the disk angular velocity Ω_D , where the dash lines represent the central value of the eigenfrequencies

interface between the two fluid domains Γ_{gap} (see 4.1b). For the wider ones, it was not the case, so we decided to investigate the convergence of the natural frequencies. As an example, we obtained the influence of N_s and N_i on the natural frequencies for the radial gap $c - a = 3$ mm, depicted in Figure 6.4. As we can see, compared to before, the convergence is reached for a higher value of N_s , and it in fact keeps increasing the smaller the radial gap is. As N_s is related to the number of terms in the sum solution to Laplace's equation, it is directly linked to the number of Bessel functions we consider. Due to their oscillatory behavior, it may be needed to implement a higher number for smaller radial gaps so that the fluid displacement potentials are able to approximate the flow in the interface Γ_{gap} . Consequently, to be able to study the influence of small radial gaps on the dynamic behavior of the rotor, we do a convergence analysis for each one in order to determine the associated couple of convergence parameters (N_s, N_i) . This approach is tedious and demonstrates that the point collocation method is limited to discretize deformable fluid-structure and fluid-fluid interfaces for small radial gaps.

In Figure 6.5, we plot the influence of the axial and radial gaps H_1 and $c - a$ on the natural frequencies of the confined rotor for the modes $n = 2, 3, 4$. The eigenfrequencies in water are normalized with those in vacuo to better appreciate their trend when the three modes are traced on the same figure. In Figure 6.5b, we display the values of (N_s, N_i) used to determine the natural frequencies for small radial gaps for the mode $(2, 0)$. We employ the same values with the corresponding radial gaps for the modes $n = 3, 4$. For the remaining data, we

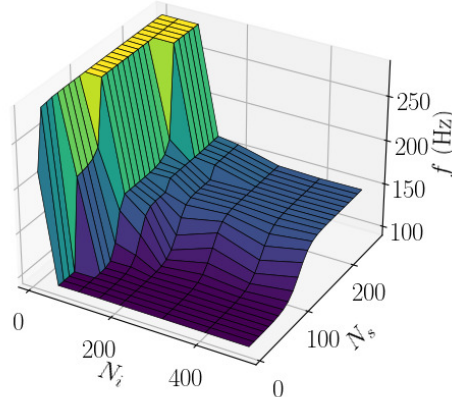


Figure 6.4 N_i and N_s influence on the natural frequencies of the rotor for $c - a = 3$ mm

keep the default values $N_s = 80$ and $N_i = 200$. In both subfigures, the natural frequencies increase with the number of nodal diameters, as well as with the axial and radial gaps for the three modes. Indeed, according to Valentín et al. (2014) and Presas et al. (2016), when the axial or radial gap decreases, the fluid is squeezed between the structure and its added mass increases. The natural frequencies of the disk are then decreased in turn. Moreover, in Figure 6.5a, past a threshold of $H_1 > 0.04$ m, increasing the axial gap does not influence the natural frequencies. The same value of axial gap was obtained by Louyot (2019), and can be used to design a casing where the axial gaps do not interfere with the dynamic behavior of the disk. When comparing the influence of both gaps, we observe that the axial gap has more influence on the eigenfrequencies, as the surface occupied by the fluid in this gap is more considerable. In Figure 6.5b, the natural frequencies decrease slightly until the radial gap is null, where they decline abruptly as no more fluid flows in the interface Γ_{gap} .

Influence of the thickness

Here we discuss the influence of the disk thickness on its natural frequencies. Figure 6.6 compares the frequencies of the modes $(2, 0)$, $(3, 0)$ and $(4, 0)$ as a function of the disk thickness h_R . We observe that the eigenfrequencies increase with the thickness, as it was demonstrated by Louyot (2019) when he analyzed the effect of h_R on the AVMI factor β_0 . Indeed, β_0 decreases for thicker disks, as the increase of their thickness raises their kinetic energy (see Equation 4.32). Moreover, from a structural point of view, the modal mass M is proportional to h_R , while the modal rigidity K is proportional to its cube. Therefore, even if increasing h_R raises the modal mass of the disk, its rigidity increases even more and causes the natural frequencies to follow the same trend, in addition to the decrease of the added mass (represented by β_0).

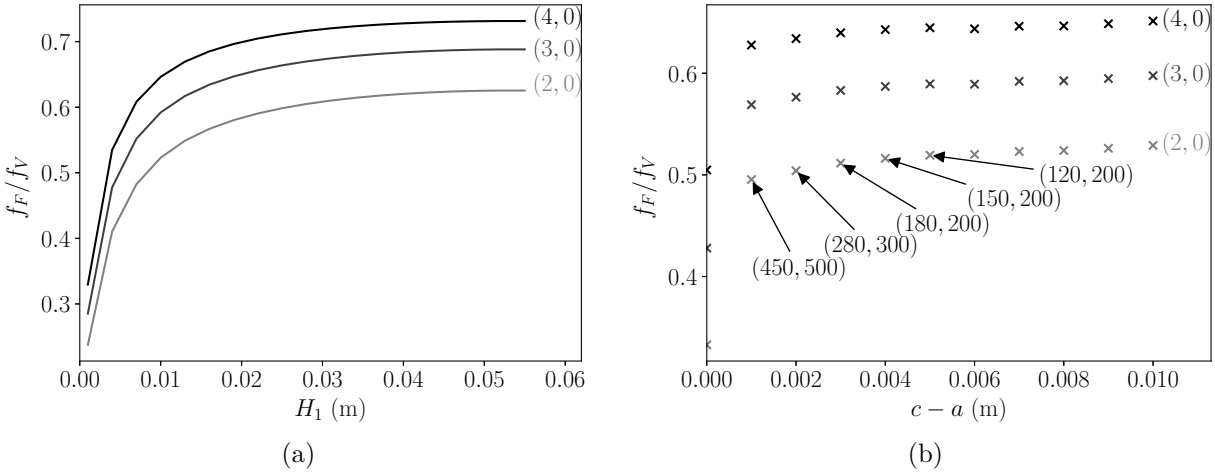


Figure 6.5 Natural frequencies of the confined rotor without rotation for the modes (2, 0), (3, 0) and (4, 0) as a function of: (a) the axial gap H_1 ; and (b) radial gap $c - a$

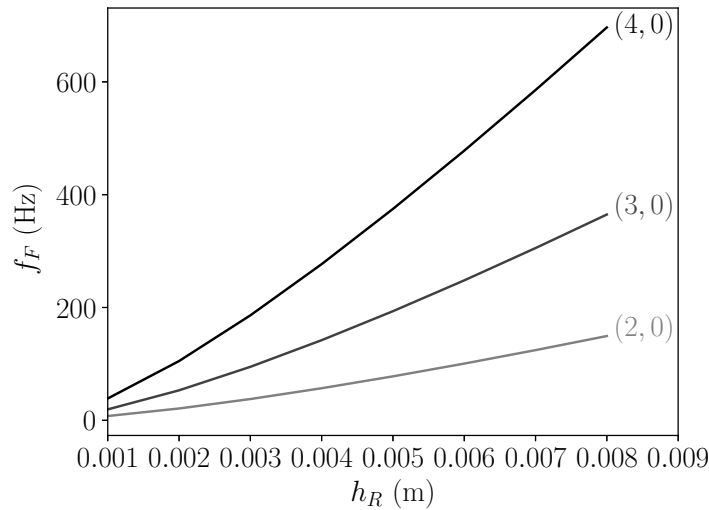


Figure 6.6 Influence of the rotor thickness h_R on the natural frequencies of the confined rotor without rotation for the modes (2, 0), (3, 0) and (4, 0)

Influence of the inner and outer radii

Figure 6.7 depicts the influence of the inner and outer radii b and a on the natural frequencies of the modes (2, 0), (3, 0) and (4, 0). For each variation, all other parameters are kept constant: for b , there is no change to do, but for a , we considered the radial gap constant at 7 mm, so that c had to be increased too. In Figure 6.7a, b has nearly no influence on the natural frequencies. It would however be expected that, although increasing b decreases similarly the modal rigidity and mass of the disk, it affects the boundary conditions of the

disk and the associated frequency parameter k_{nm} . Indeed, increasing b raises k_{nm} , and thus the modal rigidity, in regard to the modal mass. In Figure 6.7a, b has nearly no influence because it is varied slightly. In Figure 6.7b, when a increases, the natural frequencies are greatly reduced. Indeed, increasing a decreases k_{nm} , and the linked modal rigidity, while the added mass of the fluid is increased as the surface of the disk increases, as observed by Louyot (2019).

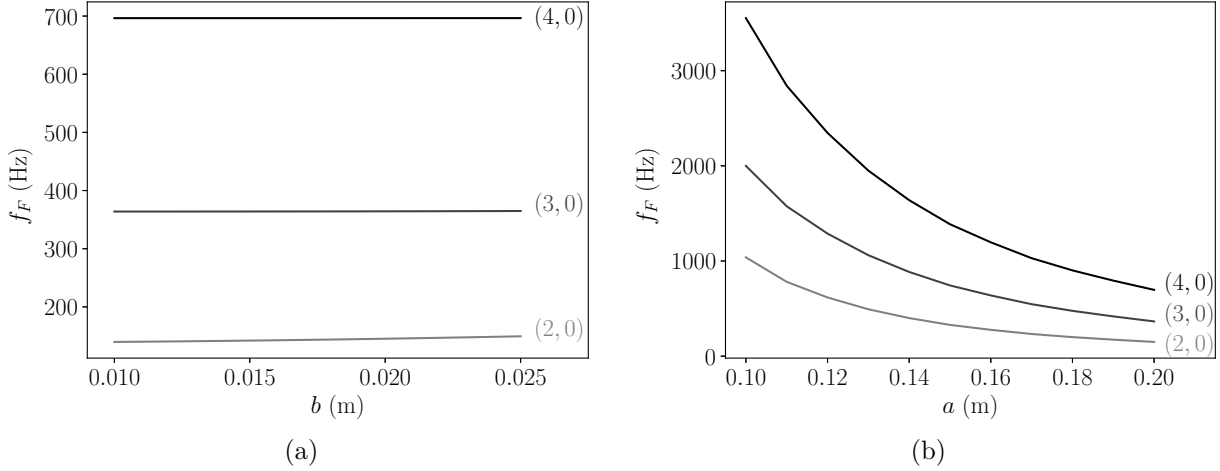


Figure 6.7 Natural frequencies of the confined rotor without rotation for the modes (2, 0), (3, 0) and (4, 0) as a function of: (a) the inner radius b ; and (b) the outer radius a

Annular disk coupled through fluid with flexible disk

Here we present and discuss the results of the analytical model for a fixed-free annular disk coupled through fluid with a clamped circular disk, i.e. the coupled rotor-stator as depicted in Table 6.1. We first verify our models for the coupled static disks and annuli (see Table 6.1) with the analytical data from Jeong (2003, 2006). We then validate the model with experimental data from Weder (2018), then compare it with the FEM model. Finally, we analyze the fluid flow without rotation and the influence of multiple parameters on the rotor-stator coupling, such as the rotation of the disk, the radial and axial gaps, as well as the thicknesses of both disks. Additionally, throughout this section, we mainly show results for the modes (2, 0), (3, 0) and (4, 0) as they are the most likely to affect the runners of hydraulic turbines (Presas et al., 2015a) and for the sake of simplicity.

Verification for the coupled static disks

Jeong (2003) analyzed analytically and numerically the coupling through fluid of two identical clamped disks (see Table 2.1). Therefore, as it is a simple model with no radial gap and only one fluid domain, we reproduced it as a first verification for our analytical model integrating the rotor-stator coupling. Moreover, in this case, as the disks are identical, the modes are exactly in-phase or out-of-phase. During our first calculations, we used the parameters $N_s = 80$ and $N_i = 200$, and we obtained the natural frequencies of the identical disks in vacuo. After going through the different steps of the method, we noticed that the values of pressures were nearly null. We deduced that it came from the values of the coefficients A_{nms} of the radial component of the fluid displacement potentials from Eq. (4.24), determined with the point collocation method. Indeed, we saw that the rank of the pseudo-inverse matrix decrease when increasing N_s , i.e. the more unknowns (represented by N_s) we have, the more dependent the equations (represented by N_i) become, until a threshold where the unknowns A_{nms} cannot be determined and are given a value of 0. Hence, it is as if the fluid is not present and that is why the natural frequencies in vacuo were found. The solution was to decrease N_s , and we selected $N_s = 10$. Table 6.6 contains the comparison of our results (using this value for N_s) with the analytical data from Jeong (2003) for the modes in-phase and out-of-phase (1, 0), (2, 0), (3, 0) and (4, 0). $\uparrow\uparrow$ stands for sinuous modes and $\uparrow\downarrow$ for varicose modes.

Table 6.6 Comparison of natural frequencies for diametrical modes from the analytical model and from Jeong (2003) - Two identical disks coupled with fluid

Mode	$(n, 0)^{\uparrow\uparrow}$			$(n, 0)^{\uparrow\downarrow}$		
	$f_{F,ana} [Hz]$	$f_{F,ana,Jeong} [Hz]$	ε	$f_{F,ana} [Hz]$	$f_{F,ana,Jeong} [Hz]$	ε
(1,0)	348.48	348.4	0.02%	149.33	147.5	1.24%
(2,0)	589.66	589.5	0.03%	369.58	366.1	0.95%
(3,0)	891.17	890.9	0.03%	672.27	667.8	0.67%
(4,0)	1256.78	1256.2	0.05%	1052.84	1048.1	0.45%

As expected, the natural frequencies increase with the number of nodal diameters, and they are lower for out-of-phase modes, as the fluid is more squeezed in that case. The analytical results are equivalent, with discrepancies between both models less than 0.05% for sinuous modes and 1.5% for varicose modes. Jeong (2003) built his analytical model using finite Fourier-Bessel series expansion and the Rayleigh-Ritz method, while we used the point collocation method and the assumed-modes approach. Consequently, for this specific configuration, the analytical model is verified, and the assumption that modeshapes are the same in water as in vacuo still holds.

Verification for the coupled static annuli

Jeong (2006) reproduced analytically and numerically the coupling through fluid of two fixed-fixed annular disks, with different inner radii and thicknesses (see Table 2.1). This model is closer to the rotor-stator coupling we want to represent, thus their analytical data (verified with finite element analysis) can serve as a second verification for our model. Indeed, as the disks are different, their modes are not exactly in-phase or out-of-phase, thus mixed, which is more representative of the rotor-stator coupling in hydraulic turbines. Moreover, it still is a simple system, as there is no radial gap and only one fluid domain. For this comparison, we are able to keep our initial values of N_s and N_i , as the coefficients A_{nms} are evaluated with two equations at the fluid-disk interface, and the rank of the pseudo-inverse is less affected by the value of N_s . Indeed, there is no deformation inside the inner radius of the disks, while they deform between the inner and outer radii. Table 6.7 contains the comparison of our results with the analytical data from Jeong (2003) for the out-of-phase modes (1, 0), (2, 0), (3, 0) and (4, 0). For this choice of nodal parameters, the modes are only varicose due to the geometry of the system.

Table 6.7 Comparison of natural frequencies for diametrical modes from the analytical model and from Jeong (2006) - Two disks with different stiffness, coupled with fluid

Mode	$f_{F,ana} [Hz]$	$f_{F,ana,Jeong} [Hz]$	ε	Coupling
(1,0)	55.3	53.55	3.16%	↑↓
(2,0)	104.1	101.76	2.25%	↑↓
(3,0)	173.3	171.83	0.91%	↑↓
(4,0)	271.0	271.55	0.06%	↑↓

For the coupled static annuli, the results are less accurate, with discrepancies of less than 4%. As for the comparison with the out-of-phase modes from Jeong (2003), we observe that the deviation decreases with the number of nodal diameters considered, to reach a low value. Jeong (2006) also used the Rayleigh-Ritz method (and the finite Hankel transform) that do not assume the same modeshapes in water as in vacuo, hence the decrease of more than 1% of the error may be due to the fact that we use the assumed-mode approach. Indeed, with an increase of the number of nodal diameters, the amplitude of the disk decreases and alters less the fluid domain. Therefore, the modes in water are closer to those in vacuo and the assumed-mode approach becomes more precise.

Validation for the coupled rotor-stator

To validate the final analytical model, we reproduce the system of Weder et al. (2019) and we use the experimental data of Weder (2018) (see Table 2.1). In this case, all the parameters and geometry dimensions are given, thus we are able to recreate the same model. However, we made some geometrical simplifications as the geometry is complex to reproduce, especially in the lower axial gap with the conical clamping of the rotor shaft (see Table 2.1). Indeed, it goes from the bottom of the casing (at 98 mm of the rotor) up to 44 mm away from the rotor. Since the lower axial gap is large, its exact value has little influence on the dynamic behavior of the structure, we therefore considered $H_2 = 98$ mm. Moreover, we did not reproduce the protruding cylindrical clamping of the stator, as it is at 25 mm away from the edge of the rotor, and does not have any impact on the fluid motion. The stator is still considered to be clamped at this distance. In fact, Weder et al. (2019) built such a setup so that only the upper axial gap and the thickness of the disks have an effect on the dynamic behavior of the rotor-stator coupling. Table 6.8 shows the parameters used as well as those employed for the parametric studies of Weder (2018).

Table 6.8 Model properties for the validation with experimental data from Weder (2018)

Parameter	Value
E [GPa]	210
ρ_D [kg/m ³]	7850
ν	0.30
ρ_F [kg/m ³]	997
H_1 [mm]	[1.4,2.2,2.9,3.6,4.4,6.4,9.4,14.4]
H_2 [mm]	98
b [mm]	15
a [mm]	100
d [mm]	125
c [mm]	150
h_R [mm]	[1,1.5,2]
h_S [mm]	[1,1.5,2]

We compare the analytical results with the experimental data through three different parametric studies on the axial gap, the rotor and stator thicknesses, as well as the out-of-phase modes.

Influence of the axial gap

Figure 6.8 depicts the comparison between the analytical results and the experimental data from Weder (2018) through the effect of the axial gap on the eigenfrequencies of the in-phase modes (2,0), (3,0) and (4,0) for a rotor and stator thickness of 1 mm. The deviations between both models are also represented in %. The natural frequencies increase with the axial gap, and with the number of nodal diameters for the three modes. Therefore, the axial gap has the same influence on the natural frequencies of the rotor-stator coupling as the ones of the confined rotor: its decrease increases the fluid added mass and lowers the eigenfrequencies. For these thicknesses of $h_R = h_S = 1$ mm, the discrepancies between both models are considerable, reaching up to more than 15% for the mode (3,0), for smaller axial gaps. This can be explained with our assumption that the fluid is inviscid. Indeed, in the experimental setup, the fluid is not ideal and its viscosity has more influence for small axial gaps, as the fluid is more squeezed. Moreover, we also considered that it could be due to nonlinear effects, but Weder (2018) explains that they considered small vibration amplitudes, thus neglecting nonlinear effects such as acoustic streaming or nonlinear stiffness of the disks. As observed before, the accuracy increases with the axial gap, and may be due to the modes in water being closer to those in vacuo for such configuration, in addition to the reduced influence of the viscosity.

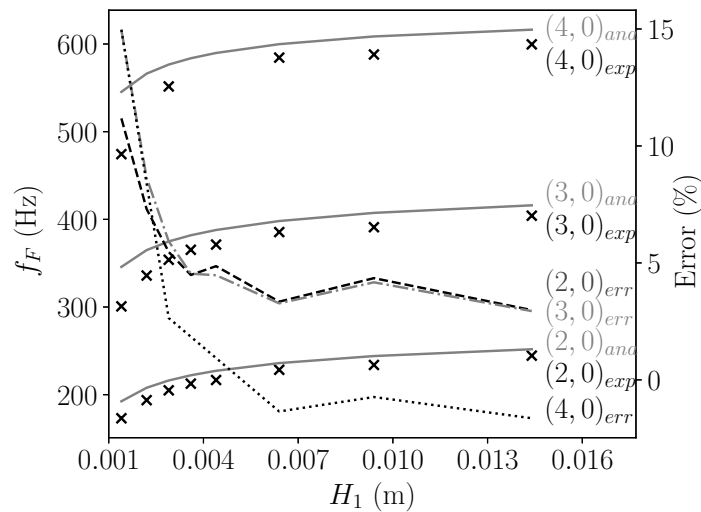


Figure 6.8 Comparison of analytical results with experimental data from Weder (2018) for the natural frequencies of the in-phase modes (2,0), (3,0) and (4,0) as a function of the axial gap $H_1 - h_R = h_S = 1$ mm

Influence of the thickness

Figure 6.9 displays the comparison of analytical results with experimental data from Weder (2018) for the natural frequencies of the in-phase modes $n = 2, 3$ of the coupled rotor-stator as a function of the axial gap for different thicknesses of the rotor $h_R = 1.5$ mm and $h_R = 2$ mm. The mode (4,0) is not displayed as it was not observed by Weder (2018). As before, with the decrease of the axial gap, the natural frequencies of the two modes decrease. The behavior of the discrepancies in both cases are different compared to before: they decrease until $H_1 = 3.6$ mm and increase afterwards to stay below a threshold of 2.5%. Overall, the deviations are lower and decrease with the rotor thickness. This may be explained by the fact that increasing the thickness of the rotor increases its rigidity and in turn its natural frequencies. This way, the eigenfrequencies of both disks are closer, which induces that they are more likely to vibrate together and that their amplitudes are more similar, resulting in a less compressed fluid. As explained before, when the fluid domain is less altered, the influence of the viscosity is lower and the assumption of inviscid fluid is more appropriate. We also considered the case where $h_R = h_S = 1.5$ mm (not shown), and we obtained similar deviations as for thicknesses of 1 mm, showing that even if we change the thicknesses and make them equal, the analytical model matches less the experimental data from Weder (2018).

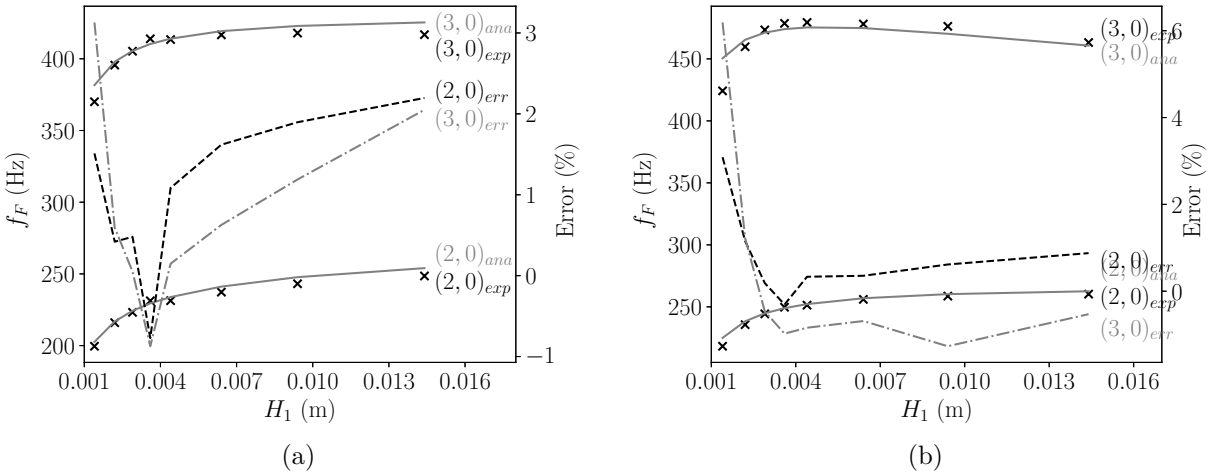


Figure 6.9 Comparison of analytical results with experimental data from Weder (2018) for the natural frequencies of the in-phase modes (2,0) and (3,0) of the coupled rotor-stator as a function of the axial gap H_1 for: (a) $h_S = 1$ mm and $h_R = 1.5$ mm; and (b) $h_S = 1$ mm and $h_R = 2$ mm

Out-of-phase modes

Figure 6.10 depicts the influence of the axial gap on the natural frequencies for the out-of-phase modes $n = 2, 3, 4$ of the coupled rotor-stator, for $h_R = 2$ mm and $h_S = 1$ mm. The eigenfrequencies for varicose modes are lower than those for sinuous modes, as explained in the introduction. One can observe that the axial gap has the same influence on the out-of-phase modes: the decrease of the axial gap lowers their natural frequencies. It also seems that the analytical prediction is more accurate for varicose modes, with all frequencies below 3.5%, even for small axial gaps. Overall, the analytical model seems to be precise for either big axial gaps or thickness ratios h_R/h_S superior to 1.

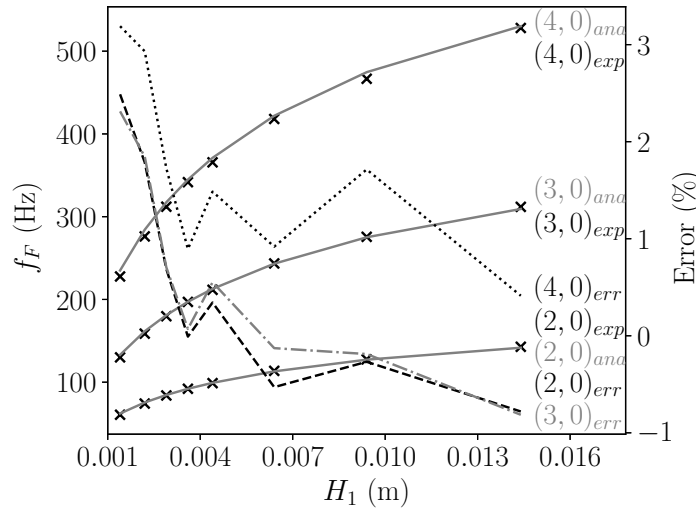


Figure 6.10 Comparison of analytical results with experimental data from Weder (2018) for the natural frequencies of the out-of-phase modes (2, 0), (3, 0) and (4, 0) of the coupled rotor-stator as a function of the axial gap H_1 - $h_S = 1$ mm and $h_R = 2$ mm

Comparison between the analytical and FEM models

Here we compare the analytical and FEM models through the same studies used to validate the first one with experimental data. In case of the FEM model, the fluid is considered compressible and the lower axial gap is $H_2 = 44$ mm. We saw that a smaller lower axial gap should only slightly affect the dynamic behavior, as explained before. This was done in order to have fewer elements in the model, to save computation time, without losing accuracy.

Figure 6.11 compares analytical and FEM results for the influence of the axial gap on the natural frequencies of the coupled rotor-stator for the modes (2, 0), (3, 0) and (4, 0). Figure 6.11a, Figure 6.11b and Figure 6.11c varies the rotor thickness ($h_R = [1, 1.5, 2]$) for the

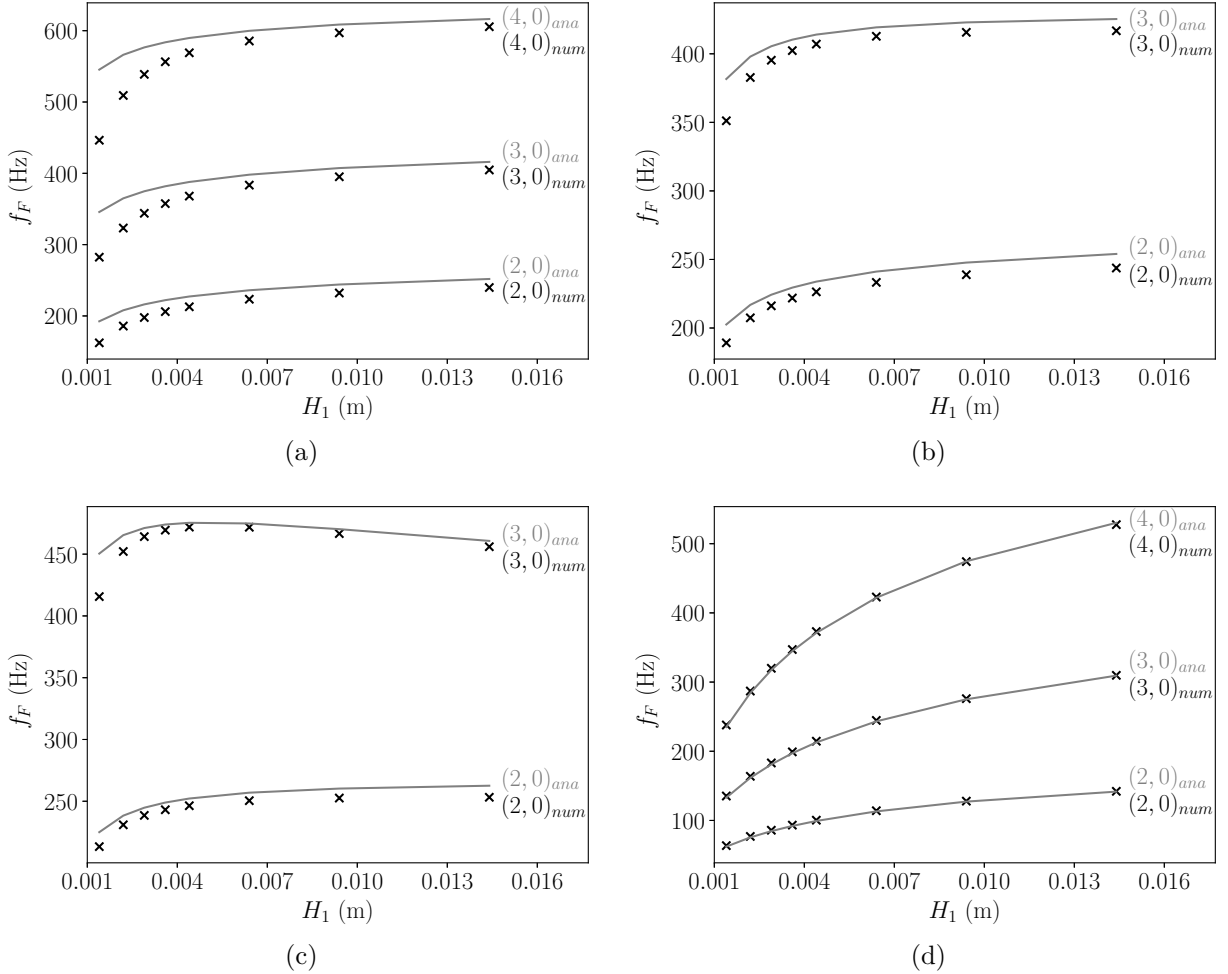


Figure 6.11 Comparison of analytical results with FEM data for the effect of the axial gap on the natural frequencies of the coupled rotor-stator configuration for the modes (2, 0), (3, 0) and (4, 0): (a) $(n, 0)^{\uparrow\uparrow}$ for $h_S = h_R = 1$ mm; (b) $h_R = 1.5$ mm; (c) $h_R = 2$ mm; and (d) $(n, 0)^{\uparrow\downarrow}$ for $h_S = 1$ mm and $h_R = 2$ mm

in-phase modes while Figure 6.11d considers the out-of-phase modes for $h_R = 2$ mm. The thickness of the stator is kept at $h_S = 1$ mm. As for the comparison between the analytical model and the experimental setup of Weder et al. (2019), both models are closer when h_R/h_S increases and are the closest for the varicose modes. We also observe that the FEM simulation is better at predicting the collapse of eigenfrequencies when the axial gap decreases. In fact, this is where the highest discrepancies between the models are present. It thus may seem that regarding the experimental data from Weder (2018), the FEM model is more accurate, but as Blais (2021) demonstrated, the FEM natural frequencies are lower than the experimental ones, which results in the same overall discrepancies, with the same trend.

Influence of parameters on implied physics

Here we analyze the influence of different parameters, such as the angular velocity, the radial gap, as well as the disks thickness, on the dynamic behavior of the rotor. This step is done to verify that we obtain the same physical phenomena observed experimentally by Valentín et al. (2017) and Weder (2018), and provide additional understanding about unexplored physics, through new parametric studies. The parameters that remain unchanged during a study are those found in Table 6.9. We choose $h_S = h_R = 1$ mm to have a thickness ratio h_R/h_S of 1 throughout the different analysis. Moreover, as the model is validated for thickness ratios higher than 1 or large axial gaps, we select $H_1 = 14.4$ mm.

Table 6.9 Model properties for the parametric studies

E [GPa]	210
ρ_D [kg/m ³]	7850
ν	0.3
ρ_F [kg/m ³]	997
H_1 [mm]	14.4
H_2 [mm]	85
b [mm]	15
a [mm]	100
d [mm]	125
c [mm]	150
h_S [mm]	1
h_R [mm]	1

Fluid flow without rotation - In-phase modes

To provide additional insight on the rotor-stator coupling through fluid, we calculate the flow of fluid without rotation, and then trace its velocity with streamlines in different planes such as (r, θ) and (r, z) . As a first step, and to see the influence of each disk deformation on the fluid for the coupled rotor-stator configuration, we select the deformation of each one and plot the associated streamlines. Figure 6.12a depicts the effect of the deformation of the rotor on the flow for the mode $(2, 0)$ of the coupled rotor-stator, while Figure 6.12b describes the flow subject to the stator deformation. The planes chosen are (r, θ) for $z = 1$ mm and $z = 14$ mm respectively, to be as close to each disk and capture their influence. The dash lines represent the nodal diameters, and it is the case for all the following figures in the plane (r, θ) .

In Figure 6.12a, the velocities outside a circle of $r = 0.1$ m are negligible so we removed

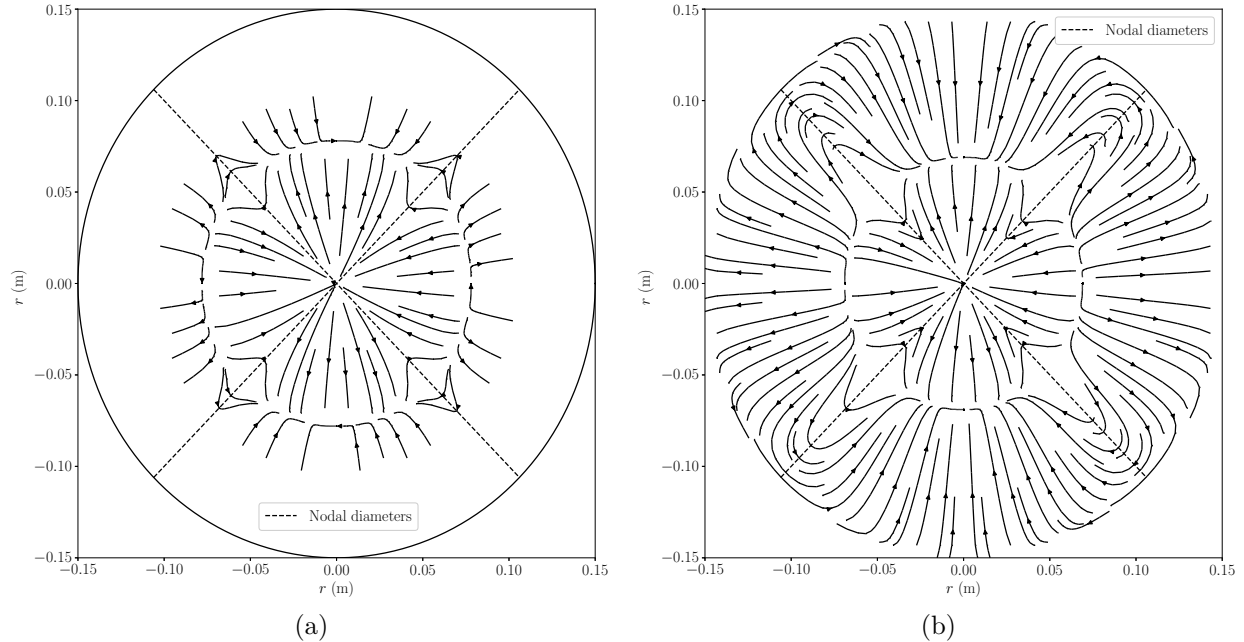


Figure 6.12 Effect of the disks separate deformation on the fluid flow in plane (r, θ) for the mode $(2, 0)$: (a) $z = 1$ mm and rotor deformation; (b) $z = 14$ and stator deformation

manually the associated streamlines. We observe the same flow as for the confined rotor. Indeed, on a circle of $r \approx 0.07$ m, there is either an influx or reflux of the fluid depending on the antinode. If it is upward, the fluid is pushed to the center of the disk and to the adjacent antinodes, as well as in the radial gap. For a downward antinode, it is the opposite: the fluid is dragged from the radial gap, the center of the disk and the adjacent antinodes. In this system, as the radial gap is 50 mm, the fluid flows close to the edge of the disk but not farther. It has no impact on the fluid placed further in the radial gap, which is globally at rest.

In Figure 6.12b, the deformation of the lone stator affects differently the fluid. We observe the apparition of the same circle where the fluid either inflows or refluxes, but it has a smaller radius of $r \approx 0.06$ m, compared to the case of the rotor. Moreover, the fluid is dragged or pushed all the way towards the edge of the confinement. Both differences may be due to the stator being a different disk. Indeed, while it has a radius of 125 mm (compared to 100 mm for the rotor), it is clamped on the outside, which results in no deformation at its edge and tighter modeshapes. The second consequence may relate to the circle of reflux or influx being smaller in radius, while the first may explain the flow reaching the lateral wall of the casing. For instance, when the rotor deforms, its edge being free, the fluid will flow around it, whereas it cannot do that at the edge of the stator and will travel along the upper wall

of the confinement. We also observe that for a corresponding antinode, the reflux and influx are shifted compared to the case for the rotor. Indeed, in the axial gap, the stator is placed above the fluid, while the rotor is below, thus, for the same antinode, they have the opposite influence on the fluid.

Once the deformation of each structure has been analyzed, we explore the influence of the rotor-stator coupling on the fluid flow. As for Figure 6.12, Figure 6.13 depicts the fluid flow in the plane (r, θ) near the rotor ($z = 1$ mm) and close to the stator ($z = 14$ mm) for the in-phase mode $(2, 0)$ of the coupled rotor-stator. In Figure 6.13a, we observe similar phenomena as for the sole deformation of the rotor from Figure 6.12a: the flow is negligible and erratic in the majority of the radial gap, while the fluid refluxes and inflows on a circle with a radius of $r \approx 0.05$ m. The circle thus has a smaller radius for the rotor-stator coupling, probably induced by the tighter stator modeshapes that are now present. Moreover, there seems to be a gap in the flow at the edge of the rotor, where the fluid was most active for the sole deformation of the rotor. In fact, as both disks are in-phase, the stator accompanies the flow created by the rotor, cancelling the one observed when it is rigid. Indeed, when it is the case, the fluid can only flow from or to the adjacent antinodes, the center and the radial gap. In this case, when the antinode is upward for example, the fluid that is supposed to travel through the radial gap is dragged to the stator and the observed flow is less considerable. For a downward antinode, the fluid that is supposed to come up through the radial gap is pushed back by the associated antinode of the stator, which reduces the flow in that location. We also notice that the reflux and influx happening on the circle near the rotor are shifted compared to the case for the sole rotor deformation. Indeed, they now match those observed on the stator, which means that the fluid flow is imposed principally by the stator deformation. It corroborates with the natural frequencies obtained for the in-phase mode, as they are similar to those for the sole deformation of the stator. Therefore, this suggests that the in-phase modes in the rotor-stator coupling are close to stator-only modes (as if the rotor is nearly rigid). The fact that the stator deformation accompanies the flow created by the rotor, instead of opposing it when it is rigid, is consistent with the observed natural frequencies. Indeed, the fluid is less accelerated this way, its added mass is reduced and the eigenfrequencies are higher for in-phase modes when the stator is flexible.

In Figure 6.13b, some slight differences are observed with the sole stator deformation case from Figure 6.12b. The circle of reflux and influx has a smaller radius of $r \approx 0.05$ m, which is consistent with the addition of the rotor. Indeed, its in-phase modeshapes centers the fluid motion, as being below the axial gap makes it accompany the flow created by the stator deformation. The flow in the radial gap is also affected by the rotor deformation with a subtle increase of the exchanges between the adjacent antinodes.

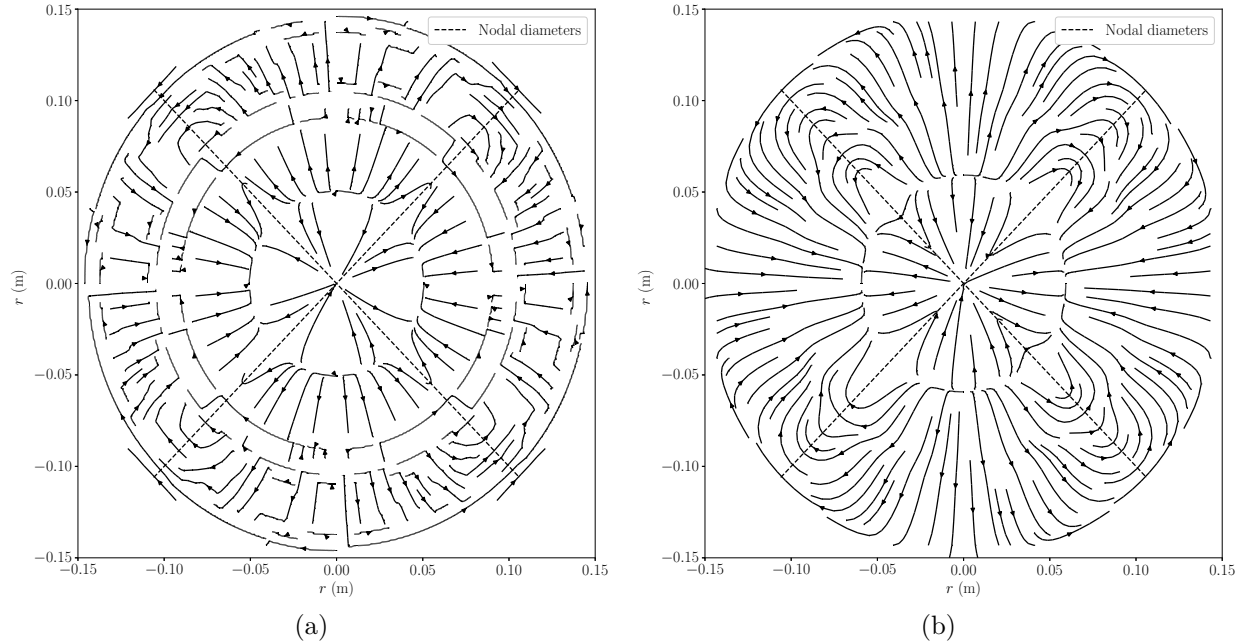


Figure 6.13 Effect of the rotor-stator coupling on the fluid flow in plane (r, θ) for the in-phase mode $(2, 0)$: (a) $z = 1$ mm; (b) $z = 14$ mm

With Figure 6.14, we analyze the influence of the rotor-stator coupling on the flow in the plane (r, θ) at the middle of the axial gap ($z = 7$ mm) for the in-phase mode $(2, 0)$. We also changed the plane of observation to $(r, 0, z)$ to observe the effect of the rotor-stator coupling on the fluid axial velocity. In Figure 6.14a, as we get closer to the stator, the fluid flow gradually changes to become what we observed near it in Figure 6.12b. The circle of reflux and influx is slightly wider, while there is still a gap in the flow around the edge of the rotor. Moreover, the flow in the radial gap becomes less erratic to be more imposed by the deformation of the stator. This suggests once more the prominence of the stator deformation on the fluid flow in the radial gap.

In Figure 6.14b, streamlines in the plane (r, z) provide additional insight on the phenomenon observed before in the other plane. At $\theta = 0$, the antinodes of the rotor and stator are upward, so the fluid below the rotor is dragged to it from the center and the edge of the cavity, while the fluid in the axial gap is pushed upward by the rotor and dragged to the stator. If the stator is rigid, the fluid in the axial gap should be pushed to the center and in the radial gap around the edge of the rotor as observed in Figure 6.2b. As the stator deforms in this case, it pulls up the fluid, shifting its flow in the axial gap as well as involving the one in the radial gap. It is also why we observe a gap in the flow at the edge of the rotor as the fluid is simultaneously dragged to it and by the stator. This once more confirms that

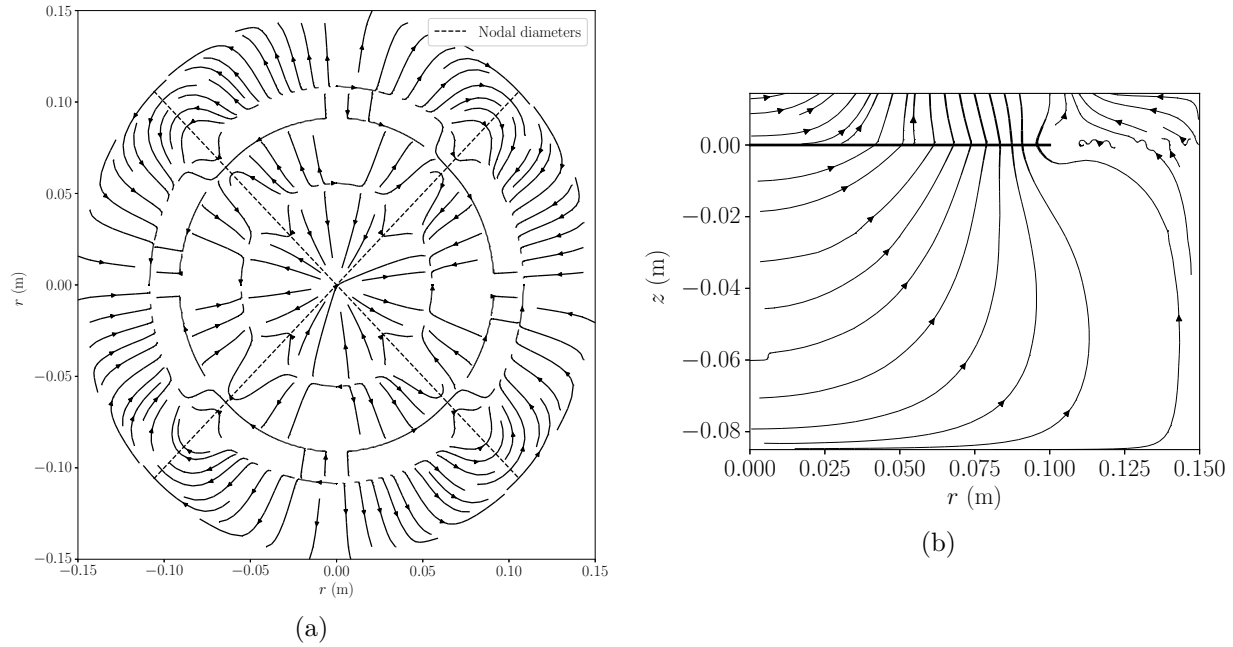


Figure 6.14 Effect of the rotor-stator coupling on the fluid flow for the in-phase mode $(2, 0)$: (a) plane $(r, \theta, 0.007)$; and (b) plane $(r, 0, z)$

the added mass of the fluid in the axial gap is reduced, bringing the eigenfrequencies of the in-phase modes closer to the higher natural frequencies of the lone stator.

Fluid flow without rotation - Out-of-phase modes

Up until now, we considered the in-phase mode $(2, 0)$, and were able to observe that they are close to stator-dominant modes. Therefore, we now take a look at the out-of-phase mode for the same number of nodal diameters. To analyze the fluid flow induced by the varicose mode, we introduce a phase shift of π/n inside the calculation of the fluid displacement potentials associated with the stator deformation from Eq. (4.37). In this way, for an upward antinode of the rotor, the stator has a corresponding downward antinode. Figure 6.15 depicts the influence of the rotor-stator coupling on the fluid flow in the plane (r, θ) at $z = 1$ mm and $z = 14$ mm for the out-of-phase mode $n = 2$. Near the rotor, in Figure 6.15a, we observe a wider circle of $r = 0.07$ m of reflux and influx no longer shifted compared to the in-phase case, as well as a flow in the radial gap similar to the one observed near the stator in Figure 6.13b. Close to the stator, in Figure 6.15b, apart from the wider circle, only the reflux and influx have shifted. All these differences are due to the flows created by each deformation being opposed. Indeed, what was observed for sole deformations is now reproduced, each disk acts as a rigid wall for one another. The fluid flow hereby confirms two aspects of the comparison

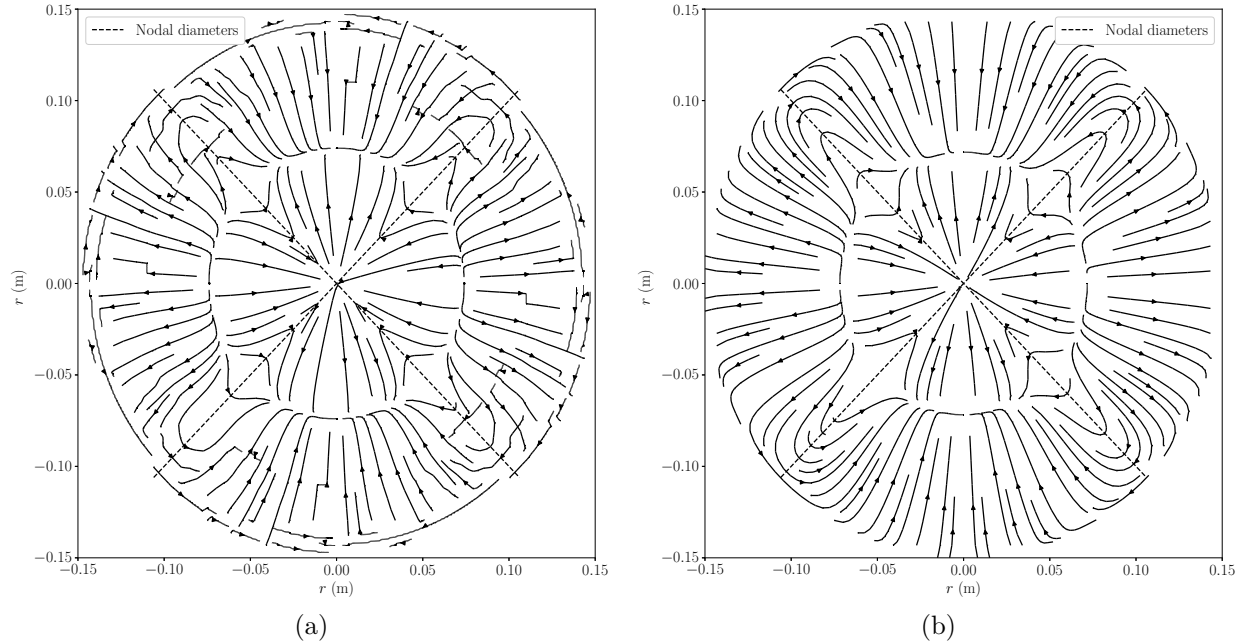


Figure 6.15 Effect of the rotor-stator coupling on the fluid flow for the out-of-phase mode $(2,0)$: (a) $z = 1$ mm; and (b) $z = 14$ mm

of the natural frequencies for each deformation, in-phase modes and out-of-phase modes. The varicose modes have lower eigenfrequencies than sinuous modes, as the flows for each deformation are opposed, the added mass of the fluid increases, reducing in turn the natural frequencies. The eigenfrequencies of the out-of-phase and the rotor-only modes are really close, which is consistent with the stator acting as a rigid wall on the flow created by the rotor deformation. This suggests that the rotor deformation is prominent for varicose modes, and that, while in-phase modes are stator-dominant modes, out-of-phase modes behave like rotor-only modes.

To corroborate the observations made for the out-of-phase modes in Figure 6.15, we look at the axial velocity of the fluid flow in the confinement. Figure 6.16 describes the effect of the rotor-stator coupling on the fluid motion in the plane $(r, 0, z)$ for the varicose mode $(2,0)$. At this location, the rotor and stator antinodes are upward and downward respectively. Compared to the in-phase modes, the flows created by both deformations are indeed opposed. In the axial gap, the fluid is pushed towards the radial gap and the center of the cavity, while it is affected similarly by the stator. It looks as if there is a rigid wall in the middle of the axial gap as each flow repulses one another. We also observe that the circle where reflux and influx appear has a wider radius of $r \approx 0.075$ m, as the fluid now travels around the edge of the rotor. It once more suggests that the added mass effect is more considerable in the

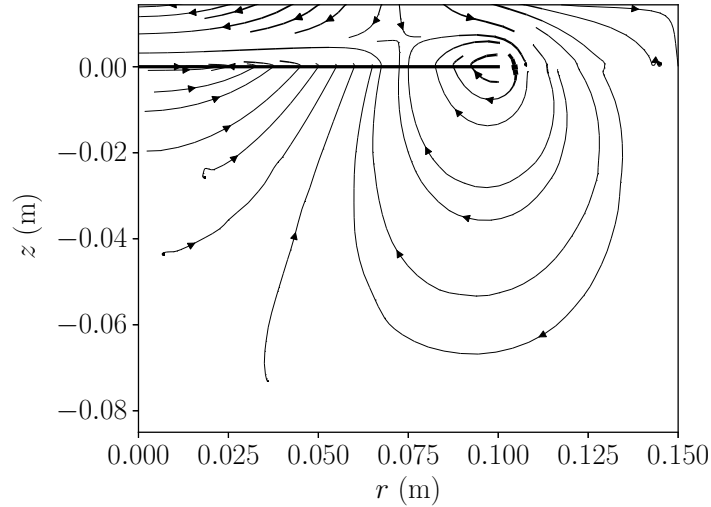


Figure 6.16 Effect of the rotor-stator coupling on the fluid flow in plane $(r, 0, z)$ for the out-of-phase mode $(2, 0)$

axial gap for out-of-phase modes and that the stator acts as a nearby-rigid wall for the rotor, making varicose modes close to rotor-only modes.

While those observations may be valid for a higher number of nodal diameters, it may not be the case for a different configuration depending on the amplitude of each disk and who is therefore dominant. The influence of characteristics of the fluid and the structure on the behavior of the rotor-stator coupling thus has to be analyzed.

Influence of rotation

To analyze the influence of the rotation on the rotor-stator coupling, we describe its associated dynamic behavior using characteristics such as the natural frequencies and the amplitude ratio (this is done for all the following parametric studies). The latter is obtained through the evaluation of the eigenmodes, once the eigenvalues (or eigenfrequencies) of the associated problem formed by the equations of motion (4.50) are determined. It is the ratio between the unknown amplitudes of the rotor A_{nm}^R and stator A_{nm}^S , such that it equals A_{nm}^R/A_{nm}^S . Therefore, when it is superior to 1, the associated mode is said to be with rotor dominant vibration, whereas an amplitude ratio inferior to 1 indicates a stator dominant vibration.

Figure 6.17a and Figure 6.17b depict the influence of the rotation on the natural frequencies of the in-phase and out-of-phase modes $(2, 0)$, $(3, 0)$ and $(4, 0)$ of the coupled rotor-stator. The eigenfrequencies are normalized with those of the rotor in vacuum f_V^R to better appreciate the mode split magnitude of the three modes. As for the confined rotor, the co and counter-

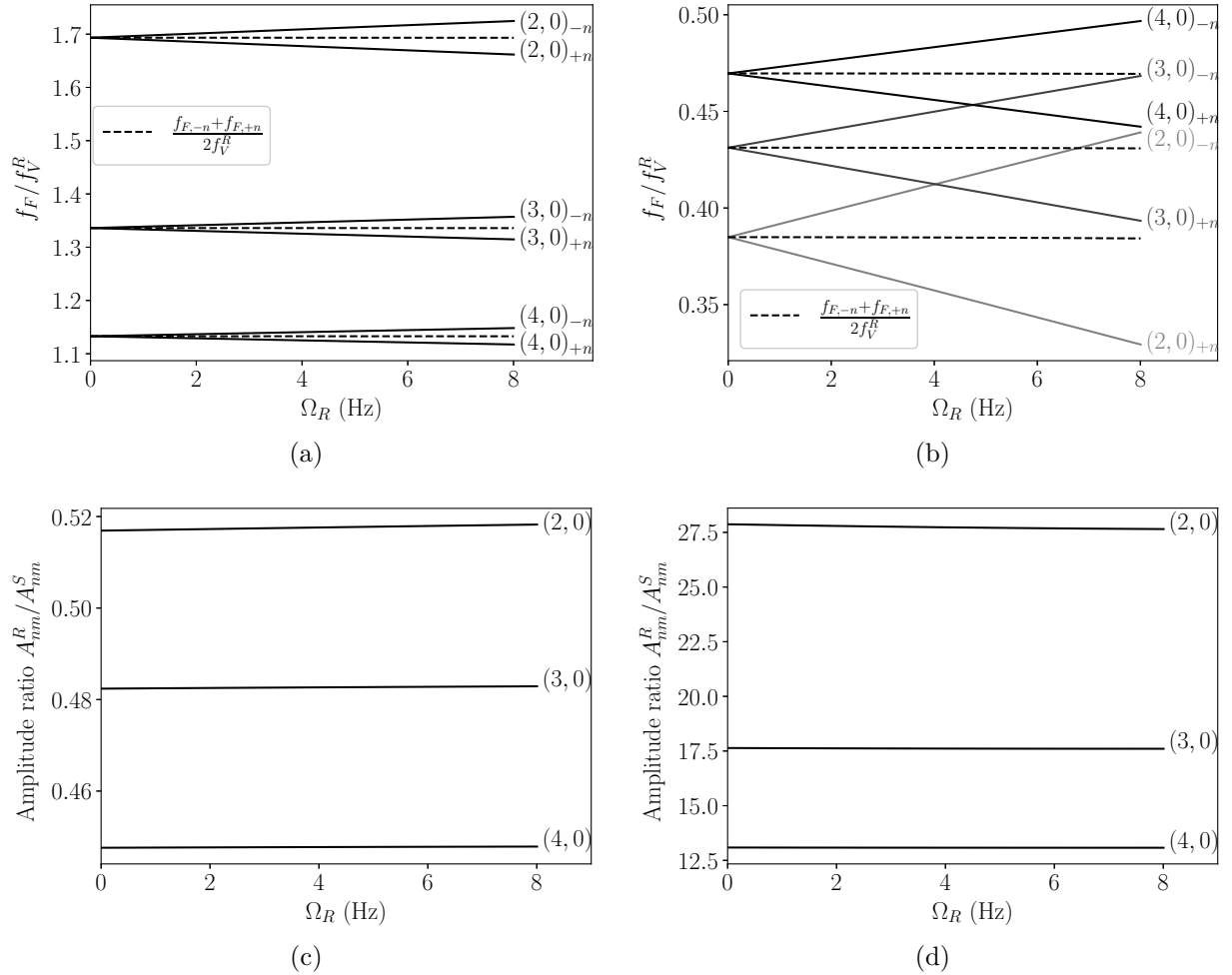


Figure 6.17 Effect of rotation on the coupled rotor-stator configuration, considering modes $(2,0)$, $(3,0)$ and $(4,0)$: (a) eigenfrequencies of $(n,0)^{\dagger\dagger}$; (b) eigenfrequencies of $(n,0)^{\dagger\ddagger}$; (c) amplitude ratios of $(n,0)^{\dagger\dagger}$; and (d) amplitude ratios of $(n,0)^{\dagger\ddagger}$

rotating waves separate to see their frequency split with increasing angular velocity. The central value of the pairs of eigenfrequencies for each mode are traced in dash line, and we can see that it slightly decreases with rotation, proving the existence of the frequency drift for the rotor-stator coupling. Apart from the effect of the rotation, we also notice that the natural frequencies of the coupled rotor-stator are higher than those of the rotor in vacuo for the in-phase modes as the ratios are superior to 1. This corroborates the fact that sinuous modes are stator-dominant, as the natural frequencies in fluid are close to those of the stator in water. In addition, the normalized eigenfrequencies of in-phase modes decrease with the number of nodal diameters, as the natural frequencies in vacuo of the rotor increase faster than those of the stator in water (the sinuous modes being stator-dominant, their eigenfrequencies follow the same trend). We observe the opposite behavior for the out-of-phase modes, as the

natural frequencies in vacuo of the rotor increase slower than those of the rotor in water (the varicose modes being rotor-dominant).

Figure 6.17c and Figure 6.17c describe the effect of the rotation on the amplitude ratios of the in-phase and out-of-phase modes $(2, 0)$, $(3, 0)$ and $(4, 0)$ of the coupled rotor-stator. The first observation is that for a higher number of nodal diameters, the amplitude ratio is lower for sinuous and varicose modes. This is explained with the amplitude of the rotor decreasing faster than the one of the stator when the azimuthal number increases. Indeed, the influence of n on the amplitude of the stator is less considerable than for the rotor, as the first is a fixed-fixed circular disk and the second a fixed-free annular disk. The amplitude ratios remain nearly constant with the rotation, suggesting that the bias motion does not have a considerable impact on the amplitude ratio, as observed by Weder (2018). However, we can still notice that it increases slightly for the sinuous modes, while it decreases for the varicose modes. This may be explained with the in-phase modes being stator-dominated, while the out-of-phase modes are rotor-dominated (amplitude ratios are lower and higher than 1 respectively). While this confirms the hypothesis advanced in the precedent section, it also suggests that either the amplitude of the rotor increases or the one of the stator decreases to reach a ratio of 1, as the disk imposes the rotation and the stator undergoes it. We also observe that the values of the amplitude ratios for out-of-phase modes are considerable. Indeed, varicose modes are rotor-dominant and the amplitude of the stator is small. It is also the case for following studies, and the range of values is higher than the one of Weder (2018). One explanation could be that the fluid being inviscid allows more considerable amplitude.

Influence of the radial gap

As the influence of the axial gap on the rotor-stator coupling has been analyzed by Weder (2018) and discussed in the comparison with his model, we study here the effect of the radial gap $c - a$. For this configuration, we defined the lateral wall of the confinement to be at $c = 125$ mm, on the edge of the stator. We then varied at first the outer radius a of the rotor from 100 to 125 mm, for an increment of 1 mm. However, our results displayed numerical instability, and we found out that decreasing the radial gap has the same effect on the convergence as for the confined rotor. The smaller it is, the higher N_s has to be for the natural frequencies of the out-of-phase modes to converge (see Figure 6.18a). This mainly concerns these modes as they are rotor-dominant and the reduction of the radial gap affects principally the confined rotor compared to the confined stator. In addition, the instability observed for the coupled static disks also has to be considered, as the equations of the FSI model are similar for the confined stator. Indeed, in Figure 6.18b, we can see that past a

threshold value of $N_s = 80$, the natural frequencies of the in-phase modes increase abruptly to become those of the stator in vacuo. The rank of the pseudo-inverse matrix decreases with N_s , and in particular here, there are three unknowns in the radial component of the fluid displacement potentials from Eq. 4.37 compared to the coupled static disks. Consequently, we cannot analyze the natural frequencies of the sinuous and varicose modes with the same approach as for the confined rotor, and we have to select a minimum radial gap so the convergence is reached for both types of modes. We also noticed that $N_s = 80$ is the limit of convergence for the in-phase modes, such that we observe numerical instability for part of the results. We decided to lower N_s to 70, and this induced that the minimum radial gap chosen for this configuration is $c - a = 6$ mm. Thus, the rotor outer radius a is varied from 100 mm to 119 mm, with an increment of 1 mm.

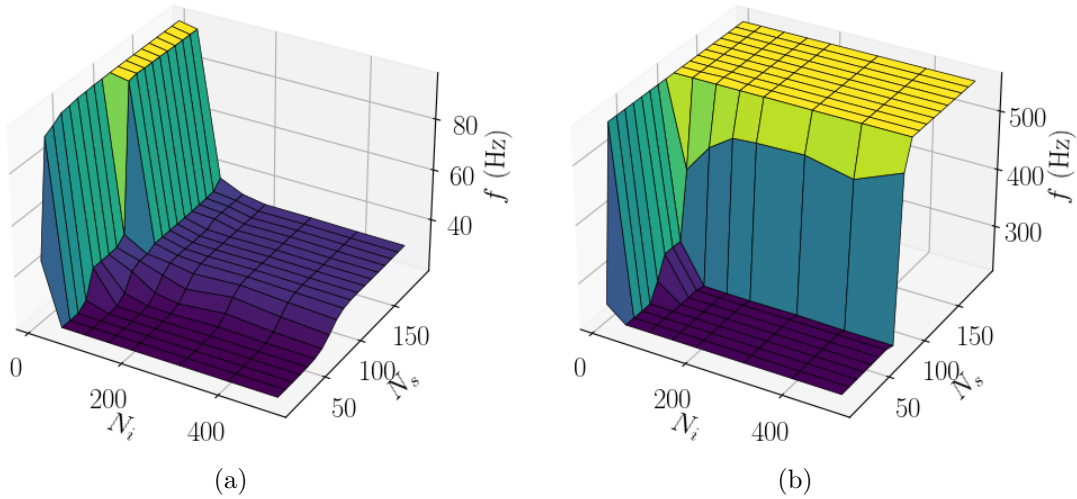


Figure 6.18 Influence of N_s and N_i on the eigenfrequencies for $c - a = 3$ mm: (a) $(2, 0)^{\downarrow}$ and (b) $(2, 0)^{\uparrow}$

Figure 6.19a and Figure 6.19b depict the impact of the radial gap on the eigenfrequencies of the in-phase and out-of-phase modes $(2, 0)$, $(3, 0)$ and $(4, 0)$ of the coupled rotor-stator. As observed for the axial gap in the coupled rotor-stator configuration and the radial gap for the confined rotor, reducing the radial gap decreases the natural frequencies, as the added mass of the fluid is increased. At first glance, reducing the radial gap, even for considerable values, decreases the eigenfrequencies of the coupled rotor-stator, where for the widest radial gaps and the confined rotor, it was demonstrated by Valentín et al. (2014) that it should not have any influence on its dynamic behavior. Therefore, this could corroborate the appreciations made when we studied the fluid flow, as the deformation of the stator involves the fluid in the radial gap. However, to decrease $c - a$, we increase the rotor outer radius and it was

observed for the confined rotor that the frequency parameter k_{nm} is greatly reduced when a is increased. Therefore, the reduction of natural frequencies for considerable values of the radial gap is probably mostly due to the increase of a and not $c - a$. In Figure 6.19b, we also observe that the reduction of the radial gap has a greater impact on the natural frequencies of the varicose modes. Indeed, the radial gap is assumed to influence the dynamic behavior of the structure through its interaction with the rotor, and we showed that the out-of-phase modes have rotor-dominant vibrations for this configuration. As a is increased to reduce the radial gap, and is an inherent characteristic of the rotor, we can appreciate that its effect on the rotor dynamic behavior is mostly visible for varicose modes as they are rotor-dominant.

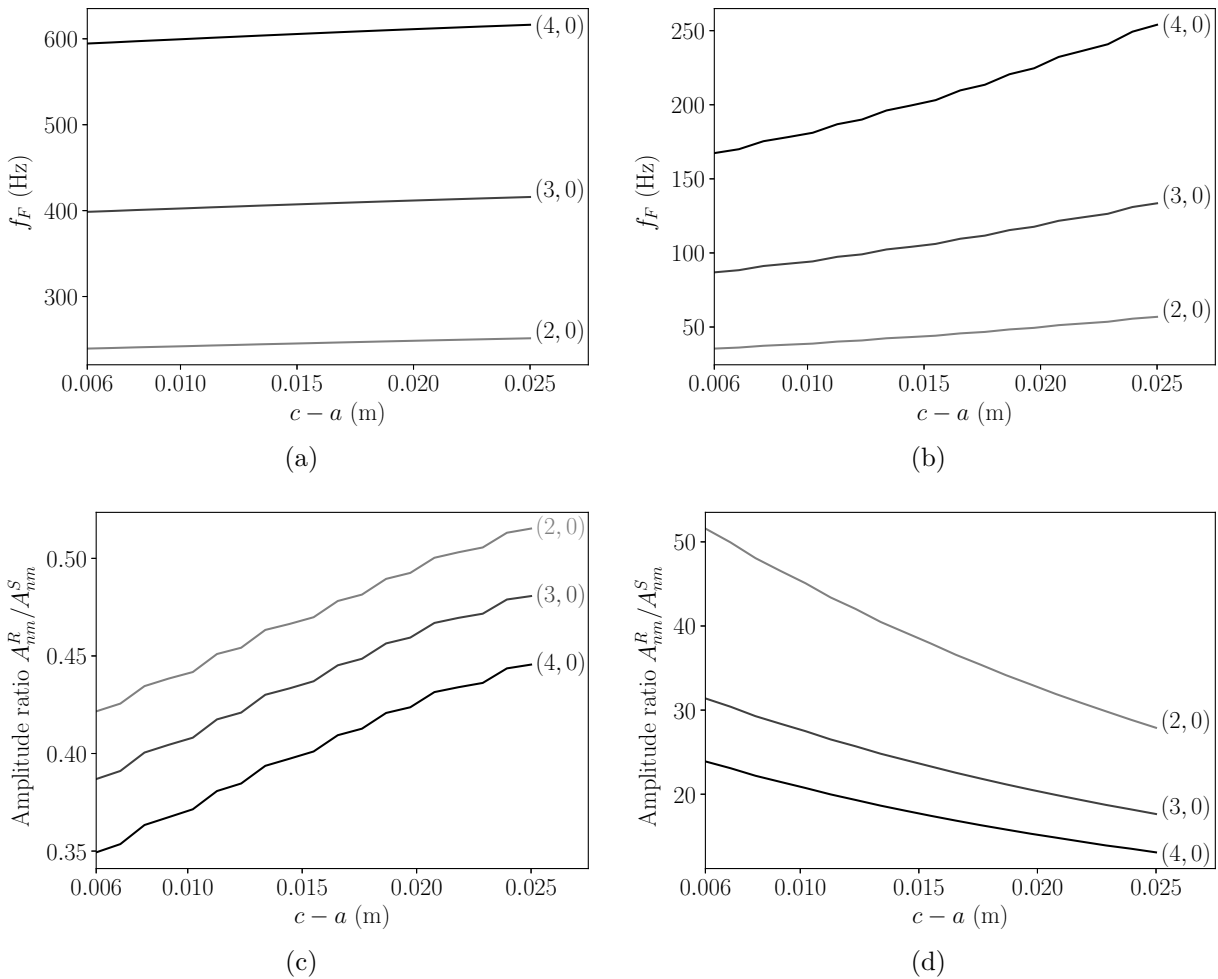


Figure 6.19 Influence of the radial gap on the coupled rotor-stator configuration, considering modes (2,0), (3,0) and (4,0): (a) natural frequencies of $(n,0)^\uparrow$; (b) natural frequencies of $(n,0)^\downarrow$; (c) amplitude ratios of $(n,0)^\uparrow$; and (d) amplitude ratios of $(n,0)^\downarrow$

Figure 6.19c and Figure 6.19d describe the influence of the radial gap on the amplitude ratios of the in-phase and out-of-phase modes (2,0), (3,0) and (4,0) of the coupled rotor-stator. In

Figure 6.19c, the amplitude ratio of sinuous modes decreases with the radial gap. In-phase modes are stator-dominant for this configuration, where the rotor is nearly rigid. Therefore, as the rotor expands, the added mass of the fluid contained in the axial gap increases. It in turn raises the amplitude of the stator, as an addition of mass to a structure reduces its natural frequencies and increases its amplitude. In Figure 6.19d, for varicose modes, reducing the radial gap increases greatly the amplitude ratio, as it is a rotor-dominant mode and the radial gap has the most influence on the rotor. Part of the curves are still jagged, showing numerical instability. It demonstrates once more the limitations of the point collocation method to discretize the deformable fluid-fluid and fluid-structure interfaces.

Influence of the rotor thickness

To analyze the influence of the thicknesses of the rotor and stator on the rotor-stator coupling, we divide the study in two, measuring the effect of each thickness separately. If we define the thickness ratio as the quotient of the rotor thickness over the stator one, Weder (2018) only studied its increase for values above 1. Our second study focuses on the decrease of the thickness ratio for values below 1. As before, we consider a wide axial gap of 14.4 mm, as the analytical model is validated for this parameter, even when the thicknesses are equal.

We first analyze the influence of increasing the rotor thickness, or the thickness ratio, on the dynamic behavior of the rotor-stator coupling. Figure 6.20a and Figure 6.20b describe the effect of the rotor thickness on the natural frequencies of the in-phase and out-of-phase modes $(2, 0)$, $(3, 0)$ and $(4, 0)$ of the coupled rotor-stator. For both types of modes, the eigenfrequencies increase with the thickness ratio: while it is linear for $h_R \geq 3$ mm for the sinuous modes, it quickly reaches an asymptote for the varicose modes. This may be explained with the in-phase modes becoming rotor-dominant as the thickness ratio rises, whereas the out-of-phase modes are already this way, and a thickness is reached where it does not affect the natural frequencies anymore (as the rotor is too rigid).

Figure 6.20c and Figure 6.20d depict the influence of the rotor thickness on the amplitude ratios of the in-phase and out-of-phase modes $(2, 0)$, $(3, 0)$ and $(4, 0)$ of the coupled rotor-stator. We appreciate an opposite behavior of the amplitude ratio for both types of modes: it increases for the sinuous modes whereas it decreases for the varicose modes (to reach nearly 0) with the increase of the rotor thickness. The same explanation as above holds: the amplitude ratio of in-phase modes rises as they become rotor-dominant (for $h_R \geq 3$ mm, they are no longer stator-dominant), while as the out-of-phase modes are already rotor-dominant, the increasing rigidity of the rotor decreases its amplitude until it is null. The trend observed for the sinuous modes suggests the importance of considering the rotor-stator coupling: the

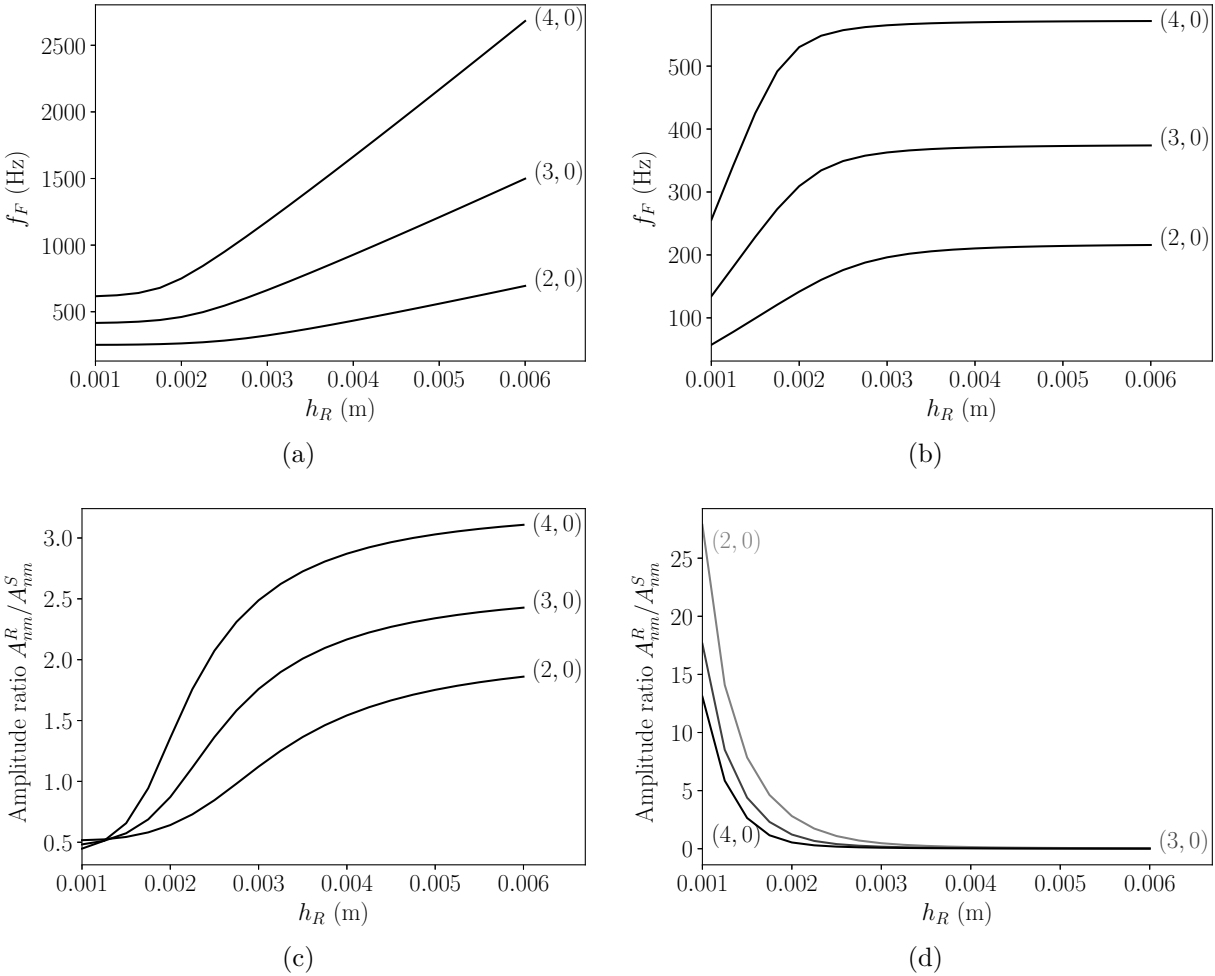


Figure 6.20 Effect of rotor thickness on the coupled rotor-stator configuration, considering modes (2,0), (3,0) and (4,0): (a) natural frequencies of $(n,0)^{\uparrow\uparrow}$; (b) natural frequencies of $(n,0)^{\uparrow\downarrow}$; (c) amplitude ratios of $(n,0)^{\uparrow\uparrow}$; and (d) amplitude ratios of $(n,0)^{\uparrow\downarrow}$

increasing rigidity of the rotor should induce a negligible amplitude ratio (as for the varicose modes), but the switch in structure-dominance first influences the amplitude ratio. Indeed, increasing the rotor thickness brings its natural frequencies in vacuo closer to those of the stator, such that there is a better coupling between both and the shift in dominance is possible. In addition, the amplitude ratio increases with the number of nodal diameters for the in-phase modes, as they are becoming rotor-dominant and the stator amplitude starts to decrease faster than the rotor one.

Influence of the stator thickness

Here we analyze the influence of increasing the stator thickness, or decreasing the thickness ratio, on the dynamic behavior of the rotor-stator coupling. The results are to be treated with caution, as this part of the analytical model has not been validated and is purely predictive.

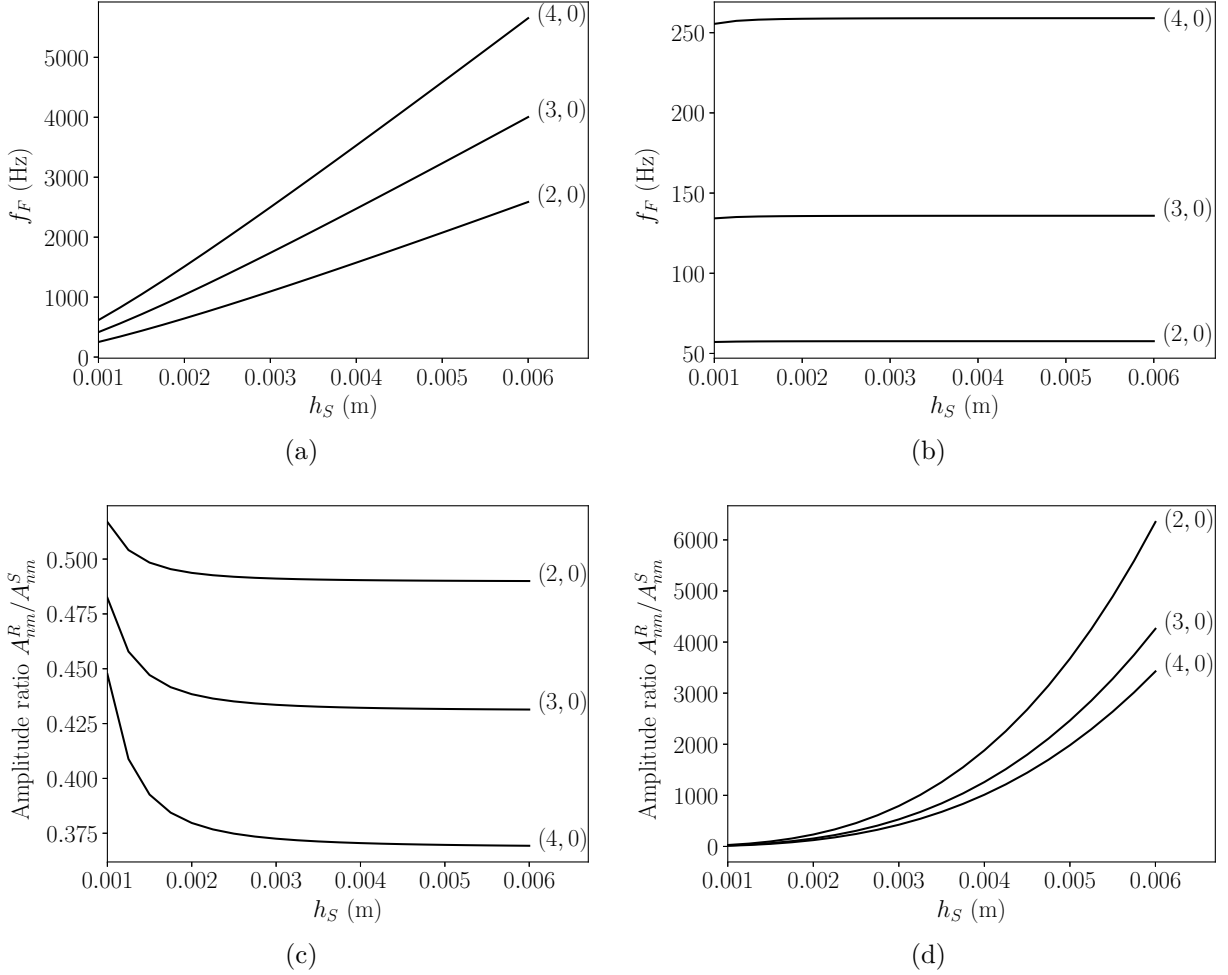


Figure 6.21 Effect of stator thickness on the coupled rotor-stator configuration, considering modes (2,0), (3,0) and (4,0): (a) natural frequencies of $(n,0)^{\uparrow\uparrow}$; (b) natural frequencies of $(n,0)^{\uparrow\downarrow}$; (c) amplitude ratios of $(n,0)^{\uparrow\uparrow}$; and (d) amplitude ratios of $(n,0)^{\uparrow\downarrow}$

Figure 6.21a and Figure 6.21b describe the effect of the stator thickness on the natural frequencies of the in-phase and out-of-phase modes (2,0), (3,0) and (4,0) of the coupled rotor-stator. For both types of modes, the eigenfrequencies rise with the decrease of the thickness ratio. However, it is linear and considerable for sinuous modes, whereas it is only a slight increase for the varicose modes. In the first case, the modes are stator-dominant, thus an increase in thickness and in turn of rigidity affects the entire rotor-stator coupling,

resulting in higher natural frequencies. The out-of-phase modes are rotor-dominant, hence an increase of rigidity for the stator that is already nearly rigid only has slight effects.

Figure 6.21c and Figure 6.21d depict the effect of the stator thickness on the amplitude ratios of in-phase and out-of-phase modes $(2, 0)$, $(3, 0)$ and $(4, 0)$ of the coupled rotor-stator. In Figure 6.21c, when increasing the stator thickness, the amplitude ratio decreases, which indicates that the sinuous modes become more stator-dominant. It quickly reaches an asymptote, as the stator is a clamped disk and increasing its thickness does not have an impact after a certain value (3 mm in this case). In Figure 6.21d, for the varicose modes, we observe the opposite behavior: as they are rotor-dominant, increasing the thickness of the stator and thus its rigidity raises the amplitude ratio. The values are considerably high, which may be due to the stator observing negligible amplitudes and as we considered inviscid fluid. We do not observe a shift in dominance as raising the stator thickness only increases the difference between the natural frequencies in vacuo of the stator and those of the rotor, such that the coupling is not enhanced.

CHAPTER 7 CONCLUSION

The analytical model is an extension of the approach developed by Louyot (2019) as it gives information on the effect of the FSI on the dynamic behavior of runners represented by annular disks submerged in dense fluid with a radial gap. To integrate the latter, we used the assumed-mode approach to impose single modeshapes of the disks on the potential flow, while representing the fluid-structure interface with the point collocation method, as done by Askari et al. (2013). The analytical method is able to predict the natural frequencies of the disk in a few seconds for different configurations (dependent of the characteristics of the fluid and the structure), and with disk rotation. Placed in the fluid reference frame, we evaluate the fluid rotation using an empirical value of the entrainment coefficient given by Poncet et al. (2005). Through the calculation of the frequencies of the co and counter-rotating waves, the frequency split and drift is well captured. The analytical model is verified using acoustic-structural modal analysis under Ansys from Blais (2021) to reproduce configurations with the same parameters and boundary conditions, lacking in available literature.

As Askari et al. (2013) who coupled the free surface of a confined fluid and the deformation of the submerged disk, we implement the rotor-stator coupling through the decomposition of each deformation and their coupling by applying the principle of superposition on the equations of motion. The analytical model is able to determine the natural frequencies of the in-phase and out-of-phase modes, as well as the associated amplitude ratio. It also offers the possibility to analyze the influence of different parameters such as the rotor and stator thicknesses, the disk rotation or the geometry of the casing. It can thus be used as a tool to assess the characteristics of the coupling through fluid of the runner with its head cover in high-head hydraulic turbines. The analytical approach is validated with experimental data from Weder (2018) for large axial gaps and/or a thickness ratio higher than 1. An acoustic-structural modal analysis of the rotor-stator coupling was implemented under Ansys in collaboration with Blais (2021) to verify its theoretical counterpart and provide a fast numerical tool.

The different parametric studies for the confined rotor configuration provide information on the influence of the characteristics of the system:

- With rotation, the natural frequencies of the confined rotor split and drift. While the first phenomenon is considerable for velocities in the range of the industry, it is not the case for the second.

- Reducing the axial and radial gaps increases the added mass of the fluid, thus decreasing the eigenfrequencies. The influence of the first one is more considerable than the second.
- Increasing the rotor thickness raises its rigidity and the associated eigenfrequencies.
- While increasing the inner radius of the annular disk raises the rigidity and the associated natural frequencies, increasing the outer radius raises its flexibility and reduces the associated natural eigenfrequencies.

For the coupled rotor-stator configuration, the parametric studies give some insights on the implied physics:

- The rotation affects the rotor-stator coupling in a similar fashion as for the confined rotor as the natural frequencies split and drift with the angular velocity. The drift is also negligible for velocities in the range of the industry. In addition, the amplitude ratio is nearly not affected.
- As for the confined rotor, decreasing the radial gap reduces the natural frequencies of the in-phase and out-of-phase modes, while it decreases and increases the amplitude ratio for the sinuous and varicose modes, respectively, without shifting the dominance of the rotor or stator.
- As the axial gap has the same influence as the radial gap according to Weder (2018), among the parameters analyzed, only the thicknesses of the rotor and stator can change their dominance in their coupling. For thickness ratios lower or equal to 1, the in-phase modes are stator-dominant, while the out-of-phase modes are rotor-dominant. This behavior shifts only when the thickness ratio is higher than 1, resulting from increasing (or decreasing) the rotor (or stator) thickness. Indeed, the natural frequencies in vacuo of the rotor become closer to those of the stator and the coupling between both is enhanced.

Limitations

As expected, the analytical and FEM models are principally limited by their assumptions, made in order to develop them. While the fluid can be assumed compressible in the numerical simulation, it is considered inviscid for both methods, as well as irrotational (and incompressible theoretically). Therefore, they both lose accuracy when there are small gaps between the flexible structures and the rigid walls, or between themselves, as viscous forces are even more considerable in these configurations. Moreover, to apply linear perturbation

theory, we consider small amplitude deformations for the disks. Hence, the models cannot take into account non-linear effects either from the fluid or the structure.

The analytical results depend on the choice of N_s and N_i to converge, and even if the selection works in most cases, we encountered some configurations where they have to be changed (such as the one from Jeong (2003) or for small radial gaps). Even when a pair of these parameters is functional, changing it can still induce small uncertainties, thus they have to be selected carefully in future extensions. However, it may not be realistic to test the convergence if a lot of configurations are created, hence we advise to check the values of these parameters if the results diverge or observe an uncommon behavior. Extra caution is recommended when reducing the radial gap between the rotor or stator and the casing, as it seems to be the geometrical characteristic with the most influence on the convergence.

Finally, due to issues with the compatibility between licences and the latest version of Ansys needed to be able to integrate the disk rotation in the modal analysis, the FEM model for the rotor-stator coupling cannot implement the rotation yet.

Outlook

First, the FEM model of the rotor-stator coupling could be extended to integrate rotation, to provide a fast numerical tool to study the mode split in disk-disk configurations.

During this project, we simulated the coupling between two annular disks and this model could be used to represent the interaction between the runner band and the discharge ring, after a validation with experimental data.

The analysis of the influence of the radial gap on the dynamic behavior of the confined rotor and coupled rotor-stator showed the limit of the point collocation method to discretize deformable fluid-fluid and fluid-structure interfaces. This approach could be replaced with a similar methodology such as Galerkin's method.

When compressible, the fluid has its own acoustic modes and natural frequencies, that are usually considered higher than those of the disk so that they do not affect each other. However, depending on the characteristics of the fluid cavity, they may be in each other's range. For instance, several analytical and numerical models were developed in the past to simulate submerged and rotating disks interacting with the acoustic modes of the surrounding fluid (Jeong, 2006; Kang and Raman, 2004, 2006a,b; Bossio et al., 2017). Therefore, it would be interesting to integrate the compressibility of the fluid in the analytical approach using those methods. A first starting point could be the work of Jeong (2006), where he develops a theoretical model for the coupling through compressible fluid of fixed-fixed annular disks.

REFERENCES

- Amabili, M. “Effect of finite fluid depth on the hydroelastic vibrations of circular and annular plates”. en. In: *Journal of Sound and Vibration* 193.4 (June 1996), pp. 909–925. ISSN: 0022460X. DOI: 10.1006/jsvi.1996.0322. URL: <https://linkinghub.elsevier.com/retrieve/pii/S0022460X96903223> (visited on 05/16/2020).
- Amabili, M., G. Frosali, and M.K. Kwak. “Free vibrations of annular plates coupled with fluids”. en. In: *Journal of Sound and Vibration* 191.5 (Apr. 1996), pp. 825–846. ISSN: 0022460X. DOI: 10.1006/jsvi.1996.0158. URL: <https://linkinghub.elsevier.com/retrieve/pii/S0022460X96901583> (visited on 05/16/2020).
- Amabili, M. and M. K. Kwak. “Free vibrations of circular plates coupled with liquids: revising the Lamb problem”. en. In: *Journal of Fluids and Structures* 10.7 (Oct. 1996), pp. 743–761. ISSN: 08899746. DOI: 10.1006/jfls.1996.0051. URL: <https://linkinghub.elsevier.com/retrieve/pii/S0889974696900511> (visited on 05/16/2020).
- Askari, E., K.-H. Jeong, and M. Amabili. “Hydroelastic vibration of circular plates immersed in a liquid-filled container with free surface”. en. In: *Journal of Sound and Vibration* 332.12 (June 2013), pp. 3064–3085. ISSN: 0022460X. DOI: 10.1016/j.jsv.2013.01.007. URL: <https://linkinghub.elsevier.com/retrieve/pii/S0022460X13000096> (visited on 02/07/2020).
- Biner, D. “Hydrodynamic damping and added stiffness prediction on a rotor-stator disk assembly in water using a modal approach”. en. MA thesis. 2017, p. 82.
- Blais, P. *Predicting the frequency split of submerged rotating disks with finite-element acoustic-structural modal analysis*. M. Eng. internship report. Polytechnique Montréal, 2021.
- Bossio, M., D. Valentín, A. Presas, D. R. Martin, E. Egusquiza, C. Valero, and M. Egusquiza. “Numerical study on the influence of acoustic natural frequencies on the dynamic behaviour of submerged and confined disk-like structures”. en. In: *Journal of Fluids and Structures* 73 (Aug. 2017), pp. 53–69. ISSN: 08899746. DOI: 10.1016/j.jfluidstructs.2017.05.008. URL: <https://linkinghub.elsevier.com/retrieve/pii/S0889974617300981> (visited on 02/07/2020).
- Coutu, A., D. Proulx, S. Coulson, and A. Demers. “Dynamic Assessment of Hydraulic Turbines”. In: 2004, pp. 16–20.
- Coutu, A., M. D. Roy, C. Monette, and B. Nennemann. “Experience with Rotor-Stator Interactions in High Head Francis Runner”. In: Foz do Iguassu, Brazil, Oct. 2008, p. 10.
- Dompierre, F. and M. Sabourin. “Determination of turbine runner dynamic behaviour under operating condition by a two-way staggered fluid-structure interaction method”. en. In:

- IOP Conference Series: Earth and Environmental Science* 12.1 (2010), p. 012085. ISSN: 1755-1315. DOI: 10.1088/1755-1315/12/1/012085. URL: <http://stacks.iop.org/1755-1315/12/i=1/a=012085> (visited on 06/13/2018).
- Egusquiza E. and Valero, C., A. Presas, X. Huang, A. Guardo, and U. Seidel. “Analysis of the dynamic response of pump-turbine impellers. Influence of the rotor”. en. In: *Mechanical Systems and Signal Processing* 68-69 (Feb. 2016), pp. 330–341. ISSN: 08883270. DOI: 10.1016/j.ymsp.2015.05.034. URL: <http://linkinghub.elsevier.com/retrieve/pii/S0888327015002988> (visited on 01/23/2017).
- Hengstler, J. A. N. “Influence of the Fluid-Structure Interaction on the Vibrations of Structures”. en. PhD thesis. ETH Zurich, 2013. DOI: 10.3929/ethz-a-010039229. URL: <http://hdl.handle.net/20.500.11850/76519> (visited on 06/14/2018).
- Hübner, B., W. Weber, and U. Seidel. “The role of fluid-structure interaction for safety and life time prediction in hydraulic machinery”. In: *IOP Conference Series: Earth and Environmental Science*. Vol. 49. IOP Publishing, 2016, p. 072007. URL: <http://iopscience.iop.org/article/10.1088/1755-1315/49/7/072007/meta> (visited on 01/23/2017).
- Jeong, K.-H. “Free vibration of two identical circular plates coupled with bounded fluid”. en. In: *Journal of Sound and Vibration* 260.4 (Feb. 2003), pp. 653–670. ISSN: 0022460X. DOI: 10.1016/S0022-460X(02)01012-X. URL: <https://linkinghub.elsevier.com/retrieve/pii/S0022460X0201012X> (visited on 02/07/2020).
- “Hydroelastic vibration of two annular plates coupled with a bounded compressible fluid”. en. In: *Journal of Fluids and Structures* 22.8 (Nov. 2006), pp. 1079–1096. ISSN: 08899746. DOI: 10.1016/j.jfluidstructs.2006.07.001. URL: <https://linkinghub.elsevier.com/retrieve/pii/S0889974606000764> (visited on 02/21/2020).
- Kang, N. and A. Raman. “Aeroelastic Flutter Mechanisms of a Flexible Disk Rotating in an Enclosed Compressible Fluid”. In: *Journal of Applied Mechanics* 71.1 (Mar. 2004), pp. 120–130. ISSN: 0021-8936. DOI: 10.1115/1.1631034. URL: <http://dx.doi.org/10.1115/1.1631034>.
- “Vibrations and stability of a flexible disk rotating in a gas-filled enclosure—Part 1: Theoretical study”. In: *Journal of Sound and Vibration* 296.4 (Oct. 2006), pp. 651–675. ISSN: 0022-460X. DOI: 10.1016/j.jsv.2005.09.001. URL: <http://www.sciencedirect.com/science/article/pii/S0022460X05006395> (visited on 01/10/2018).
- “Vibrations and stability of a flexible disk rotating in a gas-filled enclosure—Part 2: Experimental study”. In: *Journal of Sound and Vibration* 296.4 (Oct. 2006), pp. 676–689. ISSN: 0022-460X. DOI: 10.1016/j.jsv.2005.09.023. URL: <http://www.sciencedirect.com/science/article/pii/S0022460X05006401> (visited on 01/10/2018).

- Kerboua, Y., A.A. Lakis, M. Thomas, and L. Marcouiller. “Vibration analysis of rectangular plates coupled with fluid”. en. In: *Applied Mathematical Modelling* 32.12 (Dec. 2008), pp. 2570–2586. ISSN: 0307904X. DOI: 10.1016/j.apm.2007.09.004. URL: <https://linkinghub.elsevier.com/retrieve/pii/S0307904X07002260> (visited on 11/07/2021).
- Kubota, Y. and H. Ohashi. “A study on the natural frequencies of hydraulic pumps”. In: 1991, pp. 4–7.
- Kwak, M. K. and K. C. Kim. “Axisymmetric vibration of circular plates in contact with fluid”. In: *Journal of Sound and Vibration* 146.3 (May 1991), pp. 381–389. ISSN: 0022-460X. DOI: 10.1016/0022-460X(91)90696-H. URL: <http://www.sciencedirect.com/science/article/pii/0022460X9190696H> (visited on 06/11/2018).
- Lamb, H. “On the vibrations of an elastic plate in contact with water”. In: *Proceedings of the Royal Society of London. Series A, Containing Papers of a Mathematical and Physical Character* 98.690 (Nov. 1920). Publisher: Royal Society, pp. 205–216. DOI: 10.1098/rspa.1920.0064. URL: <https://royalsocietypublishing.org/doi/10.1098/rspa.1920.0064> (visited on 07/07/2021).
- Lee, H.W., S.H. Jeon, J.R. Cho, M.W. Seo, and W.B. Jeon. “Analytical and experimental study on natural sloshing frequencies in annular cylindrical tank with a bottom gap”. en. In: *Structural Engineering and Mechanics* 57.5 (Mar. 2016), pp. 877–895. DOI: 10.12989/SEM.2016.57.5.877. URL: <https://doi.org/10.12989/SEM.2016.57.5.877> (visited on 04/23/2020).
- Leissa, A. W. *Vibration of Plates*, en. Tech. rep. Ohio State University, Columbus, 1969. URL: <http://www.dtic.mil/docs/citations/ADA307623> (visited on 03/29/2018).
- Louyot, M. “Modal analysis of a spinning disk in a dense fluid as a model for high head hydraulic turbines”. fr. MA thesis. 2019, p. 65.
- Louyot, M., B. Nennemann, C. Monette, and F. P. Gosselin. “Modal analysis of a spinning disk in a dense fluid as a model for high head hydraulic turbines”. en. In: *Journal of Fluids and Structures* 94 (Apr. 2020), p. 102965. ISSN: 08899746. DOI: 10.1016/j.jfluidstructs.2020.102965. URL: <https://linkinghub.elsevier.com/retrieve/pii/S088997461930814X> (visited on 10/13/2020).
- Monette, C., B. Nennemann, C. Seeley, A. Coutu, and H. Marmont. “Hydro-dynamic damping theory in flowing water”. en. In: *IOP Conference Series: Earth and Environmental Science* 22.3 (Mar. 2014), p. 032044. ISSN: 1755-1307, 1755-1315. DOI: 10.1088/1755-1315/22/3/032044. URL: <http://stacks.iop.org/1755-1315/22/i=3/a=032044?key=crossref.8b89ccc48dc4c2071c17f4ac445234cb> (visited on 02/07/2020).

- Nennemann, B., C. Monette, and J. Chamberland-Lauzon. “Hydrodynamic damping and stiffness prediction in Francis turbine runners using CFD”. en. In: *IOP Conference Series: Earth and Environmental Science* 49.7 (2016), p. 072006. ISSN: 1755-1315. DOI: 10.1088/1755-1315/49/7/072006. URL: <http://stacks.iop.org/1755-1315/49/i=7/a=072006> (visited on 05/23/2018).
- Paidoussis, M. P. “Chapter 2 - Concepts, Definitions and Methods in Fluid-Structure Interactions”. In: *Fluid-Structure Interactions (Second Edition)*. Ed. by M. P. Paidoussis. Second Edition. Oxford: Academic Press, 2014, pp. 7–62. ISBN: 978-0-12-397312-2. DOI: 10.1016/B978-0-12-397312-2.00002-8. URL: <http://www.sciencedirect.com/science/article/pii/B9780123973122000028>.
- Piessens, R. “The hankel transform”. In: *The transforms and applications handbook* 2.9 (2000).
- Poncet, S., M.-P. Chauve, and R. Schiestel. “Batchelor versus Stewartson flow structures in a rotor-stator cavity with throughflow”. In: *Physics of Fluids* 17.7 (July 2005), p. 075110. ISSN: 1070-6631. DOI: 10.1063/1.1964791. URL: <https://aip.scitation.org/doi/abs/10.1063/1.1964791> (visited on 06/25/2019).
- Poncet, S., E. Serre, E. Séverac, M.-P. Chauve, R. Schiestel, A. Randriamampianina, and P. L. Gal. “Sur les écoulements de disque tournant”. fr. In: (2007), p. 14.
- Presas, A., E. Egusquiza, C. Valero, D. Valentin, and U. Seidel. “Feasibility of Using PZT Actuators to Study the Dynamic Behavior of a Rotating Disk due to Rotor-Stator Interaction”. en. In: *Sensors* 14.7 (July 2014), pp. 11919–11942. ISSN: 1424-8220. DOI: 10.3390/s140711919. URL: <http://www.mdpi.com/1424-8220/14/7/11919> (visited on 08/16/2021).
- Presas, A., D. Valentin, E. Egusquiza, C. Valero, and U. Seidel. “Influence of the rotation on the natural frequencies of a submerged-confined disk in water”. en. In: *Journal of Sound and Vibration* 337 (Feb. 2015), pp. 161–180. ISSN: 0022460X. DOI: 10.1016/j.jsv.2014.10.032. URL: <https://linkinghub.elsevier.com/retrieve/pii/S0022460X14008475> (visited on 08/16/2021).
- “On the detection of natural frequencies and mode shapes of submerged rotating disk-like structures from the casing”. en. In: *Mechanical Systems and Signal Processing* 60-61 (Aug. 2015), pp. 547–570. ISSN: 08883270. DOI: 10.1016/j.ymsp.2015.01.013. URL: <https://linkinghub.elsevier.com/retrieve/pii/S0888327015000151> (visited on 08/16/2021).
- “Dynamic response of a rotating disk submerged and confined. Influence of the axial gap”. en. In: *Journal of Fluids and Structures* 62 (Apr. 2016), pp. 332–349. ISSN: 08899746. DOI:

- 10.1016/j.jfluidstructs.2016.02.003. URL: <https://linkinghub.elsevier.com/retrieve/pii/S0889974616000311> (visited on 02/07/2020).
- Presas, A., D. Valentín, E. Egusquiza, C. Valero, and U. Seidel. “Experimental analysis of the dynamic behavior of a rotating disk submerged in water”. en. In: *IOP Conference Series: Earth and Environmental Science* 22.3 (Mar. 2014), p. 032043. ISSN: 1755-1307, 1755-1315. DOI: 10.1088/1755-1315/22/3/032043. URL: <http://stacks.iop.org/1755-1315/22/i=3/a=032043?key=crossref.ec8615ead88804e51211d7e923463a99> (visited on 02/07/2020).
- “On the excitation of a submerged disk-like structure with RSI patterns”. en. In: (2015), p. 5.
- Rayleigh, J. W. S. B. *The theory of sound*. Vol. 1. 1877.
- Renshaw, A.A., C. D’Angelo, and C.D. Mote. “Aerodynamically Excited Vibration Of A Rotating Disk”. en. In: *Journal of Sound and Vibration* 177.5 (Nov. 1994), pp. 577–590. ISSN: 0022460X. DOI: 10.1006/jsvi.1994.1454. URL: <https://linkinghub.elsevier.com/retrieve/pii/S0022460X84714544> (visited on 09/29/2021).
- Rodriguez, C.G., P. Flores, F.G. Pierart, L.R. Contzen, and E. Egusquiza. “Capability of structural–acoustical FSI numerical model to predict natural frequencies of submerged structures with nearby rigid surfaces”. In: *Computers & Fluids* 64 (2012), pp. 117–126.
- Seidel, U., B. Hübner, J. Löfflad, and P. Faigle. “Evaluation of RSI-induced stresses in Francis runners”. In: *IOP Conference Series: Earth and Environmental Science* 15.5 (Nov. 2012), p. 052010. ISSN: 1755-1307, 1755-1315. DOI: 10.1088/1755-1315/15/5/052010. URL: <http://stacks.iop.org/1755-1315/15/i=5/a=052010?key=crossref.040f9ece0402c8fddd06ba564ca161e4> (visited on 02/08/2016).
- Southwell, R. V. “On the free transverse vibrations of a uniform circular disc clamped at its centre; and on the effects of rotation”. en. In: *Proceedings of the Royal Society of London. Series A, Containing Papers of a Mathematical and Physical Character* 101.709 (May 1922), pp. 133–153. ISSN: 0950-1207, 2053-9150. DOI: 10.1098/rspa.1922.0032. URL: <https://royalsocietypublishing.org/doi/10.1098/rspa.1922.0032> (visited on 02/07/2020).
- Specker, M. “Simulation of the Structure-structure Coupling by Liquids using COMSOL”. PhD thesis. ETH Zürich, Oct. 2016.
- Trivedi, C., B. Gandhi, and C. J. Michel. “Effect of transients on Francis turbine runner life: a review”. In: *Journal of Hydraulic Research* 51.2 (Apr. 2013), pp. 121–132. ISSN: 0022-1686. DOI: 10.1080/00221686.2012.732971. URL: <http://dx.doi.org/10.1080/00221686.2012.732971>.

- Valentín, D., A. Presas, E. Egusquiza, and C. Valero. “Experimental study on the added mass and damping of a disk submerged in a partially fluid-filled tank with small radial confinement”. en. In: *Journal of Fluids and Structures* 50 (Oct. 2014), pp. 1–17. ISSN: 08899746. DOI: 10.1016/j.jfluidstructs.2014.06.006. URL: <https://linkinghub.elsevier.com/retrieve/pii/S0889974614001248> (visited on 02/07/2020).
- “On the Capability of Structural–Acoustical Fluid–Structure Interaction Simulations to Predict Natural Frequencies of Rotating Disklike Structures Submerged in a Heavy Fluid”. en. In: *Journal of Vibration and Acoustics* 138.3 (June 2016), p. 034502. ISSN: 1048-9002, 1528-8927. DOI: 10.1115/1.4032726. URL: <https://asmedigitalcollection.asme.org/vibrationacoustics/article/doi/10.1115/1.4032726/472580/On-the-Capability-of-StructuralAcoustical> (visited on 02/07/2020).
- Valentín, D., A. Presas, E. Egusquiza, C. Valero, and M. Egusquiza. “Experimental Study of a Vibrating Disk Submerged in a Fluid-Filled Tank and Confined With a Nonrigid Cover”. en. In: *Journal of Vibration and Acoustics* 139.2 (Apr. 2017), p. 021005. ISSN: 1048-9002, 1528-8927. DOI: 10.1115/1.4035105. URL: <https://asmedigitalcollection.asme.org/vibrationacoustics/article/doi/10.1115/1.4035105/472751/Experimental-Study-of-a-Vibrating-Disk-Submerged> (visited on 04/23/2020).
- Vogel, S. M. and D. W. Skinner. “Natural Frequencies of Transversely Vibrating Uniform Annular Plates”. en. In: *Journal of Applied Mechanics* 32.4 (Dec. 1965), pp. 926–931. ISSN: 0021-8936, 1528-9036. DOI: 10.1115/1.3627337. URL: <https://asmedigitalcollection.asme.org/appliedmechanics/article/32/4/926/425259/Natural-Frequencies-of-Transversely-Vibrating> (visited on 02/07/2020).
- Weber, W. and U. Seidel. “Analysis of natural frequencies of disc-like structures in water environment by coupled fluid-structure-interaction simulation”. en. In: (2015), p. 8.
- Weder, M. “Vibration of Rotor–Stator Systems Coupled by Viscous Liquids: Theory, Experiment and Simulation”. en. PhD thesis. 2018, p. 240.
- Weder, M., B. Horisberger, C. Monette, M. Sick, and J. Dual. “Experimental modal analysis of disk-like rotor–stator system coupled by viscous liquid”. en. In: *Journal of Fluids and Structures* 88 (July 2019), pp. 198–215. ISSN: 08899746. DOI: 10.1016/j.jfluidstructs.2019.05.003. URL: <https://linkinghub.elsevier.com/retrieve/pii/S0889974618303748> (visited on 02/07/2020).
- Zhu, F. “Rayleigh Quotients for Coupled Free Vibrations”. en. In: *Journal of Sound and Vibration* 171.5 (Apr. 1994), pp. 641–649. ISSN: 0022460X. DOI: 10.1006/jsvi.1994.1146. URL: <https://linkinghub.elsevier.com/retrieve/pii/S0022460X84711461> (visited on 02/07/2020).

APPENDIX A SEPARATION OF VARIABLES FOR THE 3D LAPLACE EQUATION IN CYLINDRICAL COORDINATES

We apply the separation of variables $\phi(r, \theta, z) = R(r)P(\theta)Z(z)$ to Laplace's equation (4.20):

$$\frac{1}{R} \frac{d^2 R}{dr^2} + \frac{1}{rR} \frac{dR}{dr} + \frac{1}{r^2 P} \frac{d^2 P}{d\theta^2} + \frac{1}{Z} \frac{d^2 Z}{dz^2} = 0 \leftrightarrow \frac{1}{R} \frac{d^2 R}{dr^2} + \frac{1}{rR} \frac{dR}{dr} + \frac{1}{r^2 P} \frac{d^2 P}{d\theta^2} = -\frac{1}{Z} \frac{d^2 Z}{dz^2}. \quad (\text{A.1})$$

As the terms from Eq. (A.1) are all independent, this equality is possible only if each side is equal to a constant. We write $-\frac{1}{Z} \frac{d^2 Z}{dz^2} = -\beta_{nm}^2$, which gives:

$$\frac{d^2 Z}{dz^2} - \beta_{nm}^2 Z = 0, \quad (\text{A.2})$$

whose solution is $Z(z) = C_1 \cosh \beta_{nm} z + C_2 \sinh \beta_{nm} z$. We choose a negative sign such that there is a solution when we apply the boundary condition of the lateral wall of Eq. (4.22) to the fluid displacement potentials. We now have:

$$\frac{1}{R} \frac{d^2 R}{dr^2} + \frac{1}{rR} \frac{dR}{dr} + \frac{1}{r^2 P} \frac{d^2 P}{d\theta^2} = -\beta_{nm}^2 \leftrightarrow \frac{r^2}{R} \frac{d^2 R}{dr^2} + \frac{r}{R} \frac{dR}{dr} + \beta_{nm}^2 r = -\frac{1}{P} \frac{d^2 P}{d\theta^2}. \quad (\text{A.3})$$

In the same way, we choose the constant n^2 , whose sign allows to write the equality between the vertical displacement of the disk w from Eq. (4.2) and the fluid velocity potentials ϕ_1 and ϕ_2 from Eq. (4.24) at their interface. As the tangential component of w is $\cos n\theta$, then $P(\theta) = \cos n\theta$. We finally obtain the modified Bessel equation:

$$\frac{d^2 R}{dr^2} + \frac{1}{r} \frac{dR}{dr} + \left(\beta_{nm}^2 - \frac{n^2}{r^2} \right) R = 0, \quad (\text{A.4})$$

whose solution is $R(r) = \sum_{s=1}^{\infty} (A_{nms} J_n(\beta_{nms} r) + B_{nms} Y_n(\beta_{nms} r))$. Each Bessel function of the first and second kind is solution to the modified Bessel equation, which gives an infinite number of solutions. Therefore, according to the superposition principle, we have to sum them all.

**APPENDIX B CONFINED ROTOR - SHAFT IN THE LOWER FLUID
DOMAIN AND SHAFT THROUGHOUT BOTH FLUID DOMAINS**

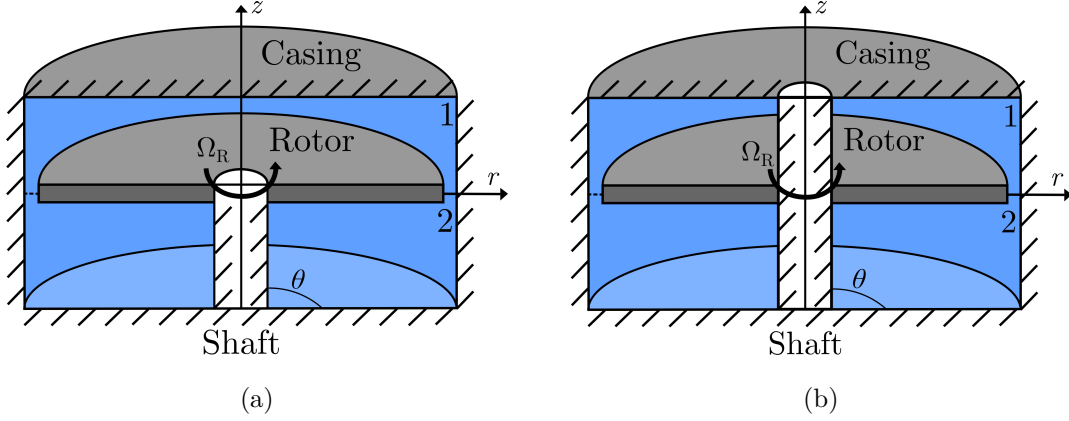


Figure B.1 System with (a) a shaft in the lower fluid domain; and (b) a shaft throughout both fluid domains

Model with a shaft in the lower fluid domain

In this model, the lower fluid displacement potential has not to be finished at $r = 0$ as a shaft is present. Therefore, we also have the Bessel function of the second kind in the radial component Eq. (4.21), and the fluid displacement potentials of each subdomain are:

$$\left\{ \begin{array}{l} \phi_1(r, \theta, z) = \cos n\theta \sum_{s=1}^{\infty} A_{nms} J_n(\beta_{nms,1}r) [C_1 \cosh \beta_{nms,1}z + C_2 \sinh \beta_{nms,1}z] \\ \phi_2(r, \theta, z) = \cos n\theta \sum_{s=1}^{\infty} (C_{nms} J_n(\beta_{nms,2}r) + D_{nms} Y_n(\beta_{nms,2}r)) [C_3 \cosh \beta_{nms,2}z + C_4 \sinh \beta_{nms,2}z] \end{array} \right. \quad \cdot \quad (\text{B.1})$$

We choose a different term β_{nms} for each potential from Eq. (B.1). Indeed, when we apply the conditions for the lateral wall and the centre of the confinement of Eq. (4.22), β_{nms} is solution to two different systems of equations, because of the different radial form of the fluid displacement potentials of Eq. (B.1).

As for the model without a shaft in both fluid domains, when we apply the conditions for the upper and lower rigid walls from Eq. (4.23) to the fluid displacement potentials from Eq.

(B.1), we get:

$$\left\{ \begin{array}{l} \phi_1(r, \theta, z) = \cos n\theta \sum_{s=1}^{\infty} A_{nms} J_n(\beta_{nms,1} r) [\cosh \beta_{nms,1} z - \tanh \beta_{nms,1} H_1 \sinh \beta_{nms,1} z] \\ \phi_2(r, \theta, z) = \cos n\theta \sum_{s=1}^{\infty} (C_{nms} J_n(\beta_{nms,2} r) + D_{nms} Y_n(\beta_{nms,2} r)) \\ \qquad \qquad \qquad [\cosh \beta_{nms,2} z + \tanh \beta_{nms,2} H_2 \sinh \beta_{nms,2} z] \end{array} \right. \quad (B.2)$$

The boundary conditions for the lateral wall and the center of the confinement give:

$$\left\{ \begin{array}{l} \frac{\partial \phi_1}{\partial r} \Big|_{r=c} = 0 \text{ and } \phi \Big|_{r=0} = 0 \\ \frac{\partial \phi_2}{\partial r} \Big|_{r=c} = 0 \text{ and } \frac{\partial \phi_2}{\partial r} \Big|_{r=b} = 0 \end{array} \right. \quad (B.3)$$

Namely, by substituting the potentials from Eq. (B.1) in Eq. (B.3):

$$J'_n(\beta_{nms,1} c) = 0 \text{ and } \left\{ \begin{array}{l} C_{nms} J'_n(\beta_{nms,2} b) + D_{nms} Y'_n(\beta_{nms,2} b) = 0 \\ C_{nms} J'_n(\beta_{nms,2} c) + D_{nms} Y'_n(\beta_{nms,2} c) = 0 \end{array} \right. \quad (B.4)$$

To solve the system of equations from Eq. (B.4), we put it in a matrix form:

$$\left[\begin{array}{cc} J'_n(\beta_{nms,2} b) & Y'_n(\beta_{nms,2} b) \\ J'_n(\beta_{nms,2} c) & Y'_n(\beta_{nms,2} c) \end{array} \right] \cdot \left[\begin{array}{c} C_{nms} \\ D_{nms} \end{array} \right] = \left\{ \begin{array}{c} 0 \\ 0 \end{array} \right\} \leftrightarrow \det \left[\begin{array}{cc} J'_n(\beta_{nms,2} b) & Y'_n(\beta_{nms,2} b) \\ J'_n(\beta_{nms,2} c) & Y'_n(\beta_{nms,2} c) \end{array} \right] = 0. \quad (B.5)$$

Consequently, the coefficient $\beta_{nms,1}$ is solution of $J'_n(\beta_{nms} c) = 0$, while $\beta_{nms,2}$ is such that the determinant from Eq (B.5) is null. We evaluate those two coefficients numerically.

Using the same boundary conditions from Eq. (B.3), we simplify the expression of ϕ_2 from Eq. (B.1). With one of both expressions from system (B.4), we express one of the factors C_{nms} or D_{nms} as a function of the other, which allows us to keep only one and reduce the number of unknowns. With the first expression from system (B.4), we write D_{nms} as a function of C_{nms} , and the expression of ϕ_2 thus becomes:

$$\phi_2(r, \theta, z) = \cos n\theta \sum_{s=1}^{\infty} R(r) [\cosh \beta_{nms,2} z + \tanh \beta_{nms,2} H_2 \sinh \beta_{nms,2} z] , \quad (B.6)$$

with

$$R(r) = C_{nms} \left[J_n(\beta_{nms,2} r) - \frac{J'_n(\beta_{nms,2} b)}{Y'_n(\beta_{nms,2} b)} Y_n(\beta_{nms,2} r) \right]. \quad (B.7)$$

This factorization, by reducing the number of unknowns, induces the convergence of this model (and the one with a shaft throughout both fluid domains), to finally get close results between the three models.

The boundary conditions for the fluid-shaft (considered rigid), fluid-rotor and fluid-fluid interfaces Γ_{shaft} , Γ_{rotor} and Γ_{gap} in $z = 0$ (see Figure 4.1b) lead to:

$$\frac{\partial \phi_{1/2}}{\partial z} \Big|_{z=0} = \left(1 + \frac{n\Omega_{D/F}}{\omega_F} \right) \psi_n(r) \cos n\theta \text{ for } b < r \leq a \text{ and } \begin{cases} \frac{\partial \phi_{1/2}}{\partial z} \Big|_{z=0} = 0 & 0 \leq r \leq b \\ \frac{\partial \phi_{1/2}}{\partial z} \Big|_{z=0} = \frac{\partial \phi_2}{\partial z} \Big|_{z=0} & a < r \leq c \\ \phi_2 \Big|_{z=0} = \phi_1 \Big|_{z=0} & a < r \leq c \end{cases} . \quad (\text{B.8})$$

The rest of the approach is the same as for the model without shaft in both fluid domains.

Model with a shaft throughout both fluid domains

The shaft is throughout both fluid domains: the boundary conditions at the center and the lateral wall of the confinement from Eq. (B.3) are the same for the upper and lower fluid domains, such that they both have expressions similar to the second one from Eq. (B.3). Hence, both fluid displacement potentials are analogous to the one for the lower fluid domain from Eq. (B.1). It is thus necessary to use the factorization with the boundary conditions at the lateral wall and the center from Eq. (B.3) for both. We obtain:

$$\begin{cases} \phi_1(r, \theta, z) = \cos n\theta \sum_{s=1}^{\infty} A_{nms} R(r) [\cosh \beta_{nms,2} z - \tanh \beta_{nms,2} H_1 \sinh \beta_{nms,2} z] \\ \phi_2(r, \theta, z) = \cos n\theta \sum_{s=1}^{\infty} C_{nms} R(r) [\cosh \beta_{nms,2} z + \tanh \beta_{nms,2} H_2 \sinh \beta_{nms,2} z] \end{cases} , \quad (\text{B.9})$$

with $R(r) = \left[J_n(\beta_{nms,2} r) - \frac{J'_n(\beta_{nms,2} b)}{Y'_n(\beta_{nms,2} b)} Y_n(\beta_{nms,2} r) \right]$. Moreover, only $\beta_{nms,2}$ intervenes in this case.

APPENDIX C EIGENFREQUENCIES CALCULATION - AVMI FACTOR AND RAYLEIGH'S COEFFICIENT

Method with the AVMI factor

The eigenfrequencies in water are written as a function of those in vacuo with the AVMI factor:

$$\frac{\omega_F^2}{\omega_V^2} = \frac{1}{1 + \beta}, \quad (\text{C.1})$$

with

$$\beta = \frac{E_F^1 + E_F^2}{E_R + E_S}. \quad (\text{C.2})$$

For reminder, we have:

$$\begin{cases} E_F^i = \rho_F \iint_{\Omega_i} \phi_i|_{z=0} \frac{\partial \phi_i}{\partial z}|_{z=0} r dr d\theta \\ E_{R/S} = \frac{1}{2} \rho_{R/S} h_{R/S} \iint_{\Omega_m} (w^{R/S})^2 r dr d\theta \end{cases}. \quad (\text{C.3})$$

By writing $A = (A_{nm}^R \ A_{nm}^S)^T$ the vector of the unknown amplitudes, we get:

$$A^T M A = 0, \text{ namely } M A = \vec{0}, \quad (\text{C.4})$$

with

$$M = \begin{bmatrix} \omega_F^2 \left(a_7 + \left(1 + \frac{n\Omega_{R/F}}{\omega_F} \right)^2 a_{1,5} \right) - a_7 \omega_V^{R^2} & \omega_F^2 \left(1 + \frac{n\Omega_{R/F}}{\omega_F} \right) \left(1 + \frac{n\Omega_{S/F}}{\omega_F} \right) a_3 \\ \omega_F^2 \left(1 + \frac{n\Omega_{R/F}}{\omega_F} \right) \left(1 + \frac{n\Omega_{S/F}}{\omega_F} \right) (a_2 + a_6) & \omega_F^2 \left(a_8 + \left(1 + \frac{n\Omega_{S/F}}{\omega_F} \right)^2 a_4 \right) - a_8 \omega_V^{S^2} \end{bmatrix}, \quad (\text{C.5})$$

where:

$$\begin{cases} a_{1,5} = \frac{1}{2} \rho_F \psi_\theta \sum_{s=0}^{\infty} (-A_{nms}^R + B_{nms}^R) \int_b^a J_n(\beta_{nms,1} r) \psi_{nm}^R dr \\ a_2 = -\frac{1}{2} \rho_F \psi_\theta \sum_{s=0}^{\infty} A_{nms}^S \int_b^a J_n(\beta_{nms,1} r) \psi_{nm}^R dr \\ a_3 = \frac{1}{2} \rho_F \psi_\theta \sum_{s=0}^{\infty} A_{nms}^R (\cosh \beta_{nms,1} H_1 - \tanh \beta_{nms,1} H_1 \sinh \beta_{nms,1} H_1) \int_0^d J_n(\beta_{nms,1} r) \psi_{nm}^S dr \\ a_4 = \frac{1}{2} \rho_F \psi_\theta \sum_{s=0}^{\infty} (A_{nms}^S \cosh \beta_{nms,1} H_1 + B_{nms}^S \sinh \beta_{nms,1} H_1) \int_0^d J_n(\beta_{nms,1} r) \psi_{nm}^S dr \end{cases} \quad (\text{C.6})$$

and

$$\begin{cases} a_7 = \frac{1}{2}\rho_r\psi_\theta \int_b^a \psi_{nm}^R{}^2 dr \\ a_8 = \frac{1}{2}\rho_r\psi_\theta \int_0^d \psi_{nm}^S{}^2 dr \\ a_6 = \frac{1}{2}\rho_F\psi_\theta \sum_{s=0}^{\infty} C_{nms}^S \int_b^a J_n(\beta_{nms,1}r)\psi_{nm}^R dr \end{cases} \quad (\text{C.7})$$

are linked to the different reference kinetic energies of the fluid, rotor and stator. As before, to determine the natural frequencies, we have to solve the eigenvalue problem of Eq. (C.4), which is equivalent to calculating the determinant of the matrix M from Eq. (C.5), where ω_F is the unknown. In M , each term in the diagonal refer to each deformation of the rotor and stator, while in the other diagonal are displayed the coupling terms. It is possible mathematically to place all coupling terms in only one term of the diagonal, and the determinant is then easier to evaluate. However, the coupling terms do not intervene anymore, such that we obtain the frequencies associated to the uncoupled deformations. Moreover, for the terms in the diagonal displaying the natural frequencies in vacuo, we have to consider for each one the eigenfrequencies linked to the associated structure deformation. Indeed, if the rotor-stator coupling is not considered anymore, we have to obtain the frequencies associated to the uncoupled deformations. This is possible only if the diagonal terms have the same expressions as when we calculate the AVMI factor for each deformation.

Method with Rayleigh's coefficient

We write the Rayleigh coefficient:

$$\omega_F^2 = \frac{V_R + V_S}{E_R + E_S + E_F^1 + E_F^2}, \quad (\text{C.8})$$

where $V_{R/S} = D_{R/S} \int_0^{2\pi} \int_{b/0}^{a/d} k_{nm}^4 (w^{R/S})^2 r dr d\theta$ is the maximum potential energy of the rotor and stator.

In the same way as for the other methods, it is possible to isolate the amplitude terms then to determine the eigenfrequencies. We noticed that the final matrices obtained through the three approaches are the same. In fact, this is what allowed us to succeed with the model by comparing the methods between them.

APPENDIX D COUPLING OF A ROTATING FIXED-FREE ANNULAR DISK WITH A FIXED-FIXED ANNULAR DISK

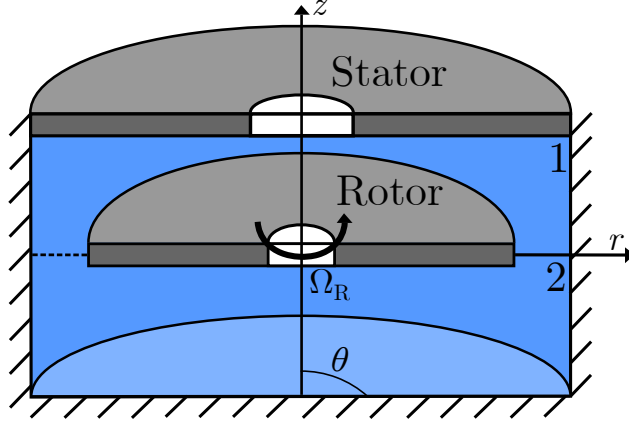


Figure D.1 Rotating fixed-free annular disk coupled with a fixed-fixed annular disk

In this model where we replace the free-fixed circular disk by a fixed-fixed annular disk, the first modification of the global approach is in the structural model of the stator. Indeed, its boundary conditions have changed and become:

$$W_{nm}(r, \theta)|_{r=e} = 0, \quad \frac{\partial W_{nm}(r, \theta)}{\partial r} \Big|_{r=e} = 0, \quad (\text{D.1})$$

$$W_{nm}(r, \theta)|_{r=c} = 0, \quad \frac{\partial W_{nm}(r, \theta)}{\partial r} \Big|_{r=c} = 0, \quad (\text{D.2})$$

where e is the inner radius of the stator and the modeshapes W_{nm} have the same form as those of the rotor.

The second change is in the FSI model of the stator, where its vertical displacement is applied on the fluid not from 0 to d , but from e to c , such that:

$$\begin{cases} \frac{\partial \phi_1^S}{\partial z} \Big|_{z=H_1} = 0 & 0 \leq r \leq e \\ \frac{\partial \phi_1^S}{\partial z} \Big|_{z=H_1} = \left(1 + \frac{n\Omega_{S/F}}{\omega_F}\right) \psi_{nm}^S(r) \cos n\theta & e < r \leq c \end{cases}. \quad (\text{D.3})$$

Considering a disk with different boundary conditions also modifies the expression of the pressures applied on the stator for both deformations, such that the integration is done on the interval $e \leq r \leq c$.